1-1-2014

Regulating Gene Expression With Light-Activated Oligonucleotides

Julianne C. Griepenburg
University of Pennsylvania, jewel1231@gmail.com

Regulating Gene Expression With Light-Activated Oligonucleotides

Abstract
The work in this thesis identifies new photochemical approaches to gain high spatiotemporal control over molecular structure and function, for broad applications in materials and biological science. "Caged" compounds provide a method for temporarily blocking function until acted upon by an external trigger, typically near-UV light. To enable multiplexing studies, three new biomolecular caging strategies were developed that can be activated with various wavelengths of near-UV or visible light. The first method, an oligonucleotide hairpin structure incorporating one or two nitrobenzyl photolinkers, was applied to a miRNA antagomir and used to "turn off" let-7 miRNA in zebrafish embryos with 365 nm light. To achieve bidirectional control over miRNA, a circular construct was designed for the ability to "turn on" the release of exogenous miRNA into zebrafish embryos with 365 nm light. A second oligonucleotide caging method, using a ruthenium-based photolinker (RuBEP), was designed to extend photoactivation to the visible spectrum, with additional potential for two-photon activation. RuBEP was used to cage antisense morpholinos through circularization via a Cu(I)-mediated [3+2] Huisgen cycloaddition reaction. RuBEP-caged morpholinos were photoactivated to "turn on" antisense activity and successfully knocked down zebrafish chd and ntl genes with 450 nm light, with limited background activity prior to irradiation. A third method of caging was based on encapsulation within photoresponsive nano-polymersomes. Self-assembly of nano-polymersomes was optimized to generate visible-light-responsive vesicles that incorporate a porphyrin dimer in the hydrophobic membrane. These nanovesicles were shown to encapsulate a variety of cargo, including 25mer oligonucleotides, a small molecule fluorescent dye, and two biologically relevant metal ions, Zn2+ and Ca2+. The photoresponsiveness of the system was modulated with light wavelength, irradiation time, and the presence of dextran in the aqueous core.

Degree Type
Dissertation

Degree Name
Doctor of Philosophy (PhD)

Graduate Group
Chemistry

First Advisor
Ivan J. Dmochowski

Keywords
Light-activated, Oligonucleotides, Photo-activated, Polymersomes, Ruthenium, Zebrafish

Subject Categories
Biochemistry | Chemistry

REGULATING GENE EXPRESSION WITH LIGHT-ACTIVATED OLIGONUCLEOTIDES

Julianne C. Griepenburg

A DISSERTATION

in

Chemistry

Presented to the Faculties of the University of Pennsylvania

in

Partial Fulfillment of the Requirements for the

Degree of Doctor of Philosophy

2014

Supervisor of Dissertation

_____

Dr. Ivan J. Dmochowski

Associate Professor of Chemistry

Graduate Group Chairperson

_____

Dr. Gary A. Molander
Hirschmann-Makineni Professor of Chemistry

Dissertation Committee

Dr. David W. Christianson, Roy and Diana Vagelos Professor of Chemistry and Chemical Biology

Dr. Barry S. Cooperman, Professor of Chemistry

Dr. Tobias Baumgart, Associate Professor of Chemistry

ACKNOWLEDGMENT

I would first like to thank my advisor, Dr. Ivan Dmochowski, for his continued guidance throughout my graduate career. I truly appreciate the advice and support he has provided. The opportunities I have had in the Dmochowski Lab have helped me grow both scientifically and professionally. I would also like to thank my committee members, Dr. David Christianson, Dr. Barry Cooperman, and Dr. Tobias Baumgart. I have truly appreciated their insight, knowledge, and constructive criticism which has helped to guide me in my research.

I'd like to extend a very special thank you to the people I have spent every day of the past several years with - the Dmochowski Lab members, both past and present. Graduate school would have been a lot more difficult without such wonderful coworkers and friends. Thank you all for sharing the ups and downs of graduate school life. I'd like to give a special thank you the members of "Team Oligo" who worked on this project with me, especially Dr. Xinjing Tang, Sean Yeldell, and Teresa Rapp. Dr. Xinjing Tang was a wonderful post-doc and mentor, and helped me get acclimated with the project and the lab when I first started. I am very grateful to him for his patience as I was learning a completely new area of research. I am also very happy to have Sean and Teresa to leave this project to and I am very confident in their continuation of this work! In addition to leaving my project in good hands, I know I am turning over the role of lab baker to two of the best - Teresa and Katie Pulsipher! Finally, I must give a personal thank you to Brittany Riggle, as both a coworker and friend. Brittany has been so supportive throughout every aspect of graduate school and I am so grateful to her for always being there for me. I have always been able to count on Brittany for sound advice in science and life in general. Brittany is one of the most talented and helpful people I know and I will truly miss working with her.

I would also like to thank all of the friends that I have made over the years, starting with the great group of friends from my first year of graduate school, Ariane Perez-Gavilan, Genette "G" McGrew, Josh Stecher, and Najat Khan. I wouldn't have survived the early years of graduate school without them. We spent so many days and nights studying, but also had a ton of fun, exploring Philadelphia together and cooking our weekly dinners. I know we will continue to stay in touch as we all move forward with our careers. Another wonderful friend that I was so lucky to meet in graduate school is Anne Wagner. Anne was my go-to for stress relief, whether it was going to lunch, or taking a quick coffee break and talking about dogs! Anne has a very special talent of making everyone around her smile! I'd also like to thank Nimil Sood as both a collaborator and friend. Nimil and I worked so well together on a very difficult project and have become great friends in the process. I will miss our happy hours after long days of experiments! Finally, I'd like to give much credit to my best friend since middle school, Ellen McColl, for always being there for me either for support, advice, or a good laugh!

My family has been my greatest support system throughout graduate school. I am very fortunate to have such caring, loving, and supportive parents who have always been there for me throughout every aspect of my life. I also feel very lucky to have my brother, Todd, and sister, Suzanne, who I know I can always turn to for advice or just a good chat. My husband, Chris, has been supportive of me throughout this entire process. It was always nice to be able to get home from work and have someone to talk about the day with that understands what graduate school life is about. We have been there for each other through many stressful years of school, and I am beyond excited that we are both finally done! Of course, I have to thank all of the non-humans in my life - my dogs, bunnies, and other critters. My pets have always given me something to smile about, and a great excuse to take a break!

ABSTRACT

REGULATING GENE EXPRESSION WITH LIGHT-ACTIVATED OLIGONUCLEOTIDES

Julianne C. Griepenburg

Ivan J. Dmochowski

The work in this thesis identifies new photochemical approaches to gain high spatiotemporal control over molecular structure and function, for broad applications in materials and biological science. "Caged" compounds provide a method for temporarily blocking function until acted upon by an external trigger, typically near-UV light. To enable multiplexing studies, three new biomolecular caging strategies were developed that can be activated with various wavelengths of near-UV or visible light. The first method, an oligonucleotide hairpin structure incorporating one or two nitrobenzyl photolinkers, was applied to a miRNA antagomir and used to “turn off” *let-7* miRNA in zebrafish embryos with 365 nm light. To achieve bidirectional control over miRNA, a circular construct was designed for the ability to “turn on” the release of exogenous miRNA into zebrafish embryos with 365 nm light. A second oligonucleotide caging method, using a ruthenium-based photolinker (RuBEP), was designed to extend photoactivation to the visible spectrum, with additional potential for two-photon activation. RuBEP was used to cage antisense morpholinos through circularization via a Cu(I)-mediated [3+2] Huisgen cycloaddition reaction. RuBEP-caged morpholinos were photoactivated to “turn on” antisense activity and successfully knocked down zebrafish

chd and *ntl* genes with 450 nm light, with limited background activity prior to irradiation. A third method of caging was based on encapsulation within photoresponsive nano-polymersomes. Self-assembly of nano-polymersomes was optimized to generate visible-light-responsive vesicles that incorporate a porphyrin dimer in the hydrophobic membrane. These nanovesicles were shown to encapsulate a variety of cargo, including 25mer oligonucleotides, a small molecule fluorescent dye, and two biologically relevant metal ions, Zn^{2+} and Ca^{2+}. The photoresponsiveness of the system was modulated with light wavelength, irradiation time, and the presence of dextran in the aqueous core.

TABLE OF CONTENTS

LIST OF TABLES

LIST OF ILLUSTRATIONS

Chapter 1

Introduction to light-activation

I. "Uncaging" with light

The understanding of complex biological systems is advanced by tools that can help manipulate structure, function, and or localization of molecules with high spatial and temporal resolution. One strategy is to put an active compound under the control of a conditional trigger. This concept of blocking a compound's biological activity until acted on by an internal or external stimulus was termed "caging" in 1978 by Kaplan et. al. with the photolytic release of adenosine 5'-triphosphate.[1] Light-activation dates back to 1943, however, with the example of azobenzene modified amino acids.[2] Although the term "caged" is now widely used in biochemistry, it is somewhat of a misnomer because most caging strategies involve the use of one or more small photoactive moieties rather than true molecular confinement.

Light in the UV to near IR (NIR) window is a commonly used external stimulus for the activation of caged molecules as it can be very easily manipulated both temporally and spatially. Spatial control depends on the irradiation source and activation wavelength, but generally, confocal laser scanning microscopy (CLSM) and two-photon microscopy provide excellent and well established spatial resolution with the ability to irradiate and image simultaneously. Two-photon microscopy achieves high spatial resolution, with the ability to control light in three dimensions down to the sub-cellular level and femtoliter volumes.[3,4] Although UV light has been commonly used for uncaging due to the broad availability of UV-active caging groups[5], uncaging with longer wavelengths of light has many potential benefits. Absorption and scattering decrease with increasing wavelength,

as scattering has a λ^{-4} dependence on wavelength. Visible light is far less damaging to cells than UV light[6], and has the potential to penetrate biological systems up to 1 cm.[7] This makes visible light activation feasible for small biological model systems and cells. However, when transitioning to larger biological systems, significantly higher depth penetration is necessary. The NIR window (700 - 900 nm) has a very low absorption coefficient in biological tissue, and combined with low levels of scattering, NIR light has the potential to penetrate tissue to depths of several centimeters.[7] Above 900 nm, this is hindered by strong water absorption.

It is important to expand the currently available caging toolkit to include a broader range of biologically active molecules that can be controlled light. Specifically, there is a need to be able to cage molecules ranging from small metal ions to large proteins and plasmids. Additionally, it is of equal importance to expand the wavelengths that can be used for uncaging. Several examples exist in the literature for caging moieties that can be activated with UV light, but fewer exist for longer wavelength light in the visible and near-IR region. Ideally, the future will hold a vast library of caged biomolecules that can be activated with high spatiotemporal resolution at different wavelengths of light spanning the UV, visible and near-IR spectrum.

This introduction will focus on literature precedent for three types of caging relevant to the work presented in this thesis: 1) The commonly used UV-active moieties and their applications in caging short oligonucleotides, 2) Visible and two-photon light activated ruthenium complexes, and 3) Light-responsive polymersomes as nanocarriers.

II. Common caging groups

Three photoresponsive caging groups that have been commonly used for biological applications are nitrobenzyl, coumarin, and azobenzene moieties, shown in Figures 1-1, 1-2, and 1-3. These caging groups and their derivatives have received attention for their ability to be incorporated site-specifically into biomolecules to control structure and function with UV light.

The most commonly used caging group[8], and the caging group used most frequently in our laboratory is the nitrobenzyl group, shown in Figure 1-1. The ortho-nitrobenzyl has been widely used as a synthetic protecting group since initial reports in 1970.[9,10] Ortho-nitrobenzyl is photoactive at 365 nm, but the wavelength can be tuned by adding substituents. Common derivatives of 2-nitrobenzyl are the 4,5-dimethoxy analog (DMNB), 1-(2-nitrophenyl)ethyl (NPE) and 4,5-dimethoxy analog (DMNPE) and α-carboxy analog (CNB) which range in activation wavelength from 260 nm to 365 nm.[11] These analogs provide benefits and drawbacks, for example, CNB has increased hydrophilicity due to the carboxy groups, but activates at shorter wavelengths (maximum at 260 nm).[12] DMNPE and DMNB activate at longer wavelengths (maximum at 355 nm), but photolysis rates and quantum yields are typically much lower than for CNB. Recently, styryl-2-nitrobenzyl (SNB) moieties were presented to extend conjugation and red-shift activation wavelengths to 370 nm, allowing tail-end activation up to 450 nm.[13] The nitrobenzyl moiety has become so widely used for photocontrol over oligonucleotides, that a phosphoramidite was made that can be directly incorporated into

solid-phase synthesis,[14,15] and is now commercially available through Glen Research (Sterling, VA).

Initial literature on coumarin protecting groups dates back to 1984 with the report on 7-methoxycoumarin-4-ylmethyl (MCM) esters by Givens et al.[16] Irradiation of coumarin results in the release of the protected carboxylic acid and formation of the corresponding hydroxymethyl coumarin. Typical MCM esters have activation wavelengths in the UV (340 - 360 nm) range, but the spectral range of irradiation can be altered with the addition of substituents, which can also change the hydrophilicity and quantum yield of photolysis. Brominated 7-hydroxycoumarin-4-ylmethyl esters (Bhc) is a coumarin derivative reported by Furuta et al. that has been modified to push the activation wavelength to 365 nm. Additionally, the extended conjugation and high extinction coefficient for π-π^* transitions makes Bhc two-photon active with a cross section of 1 GM.[17] This two-photon active coumarin has been applied to the design and synthesis of a caged glutamate and used to resolve three-dimensional maps of neuron glutamate sensitivity in intact mouse brain slices.[17] Structures of coumarin (MCM ester) and derivative Bhc are shown in Figure 1-2. Recently, coumarin derivatives have been synthesized for photoactivation with visible light. Variations of (coumarin-4-yl)methoxycarbonyl (CMOC) have been shown to light-activate in the visible region, and by adding carboxylate substituents, these chromophores can be made more water soluble,[18] which makes them candidates for biological applications.[19]

Azobenzene is another popular choice as a photoactive moiety that has a different light-activated mechanism than other caging groups. Azobenzene undergoes *trans-cis* isomerization upon irradiation with UV light, resulting in a structural change instead of photocleavage. Unlike the previously presented groups, nitrobenzyl and coumarin, azobenzene has the ability to "photoswitch" and reverse back to *trans*, initiated either thermally or upon irradiation with visible light. Many derivatives have been made to adjust the wavelength, quantum yield, and to prevent the thermally activated isomerization back to the *trans* configuration to have better control over the system with light.[20] Several examples in the literature have used azobenzene, from the reversible photocontrol of oligonucleotide duplex formation,[21-23] to the incorporation of azobenzene derivatives in diblock copolymers for materials science applications.[24-26] The reversible isomerization of azobenzene is shown in Figure 1-3.

III. Light-activated oligonucleotides

Caging a wide variety of small and large biologically active molecules has been a popular area of research and has had much success in recent years. Examples of caging can be found for molecules including metal ions,[27] peptides,[28] oligonucleotides,[29] proteins,[30] and plasmids.[31,32] This review will focus on literature pertaining to caging short oligonucleotides that control gene expression, primarily antisense oligonucleotides.

Over the past two decades, several methods for controlling oligonucleotide function with light have been developed.[29] Caging oligonucleotides is challenging due to

their complexity and large size, and thus, many different methods have been explored. Initial efforts towards light-activated oligonucleotides were made in 1995 by Ordoukhanian et. al., with the design of photoresponsive DNA "building blocks" which could be site-specifically incorporated into a short oligonucleotide synthesis, and destabilize hybridization upon photolysis with 355 nm light.[33] Another example of using photoresponsive nucleobases to induce DNA strand breaks was presented in 2002 by Dussy et. al.[34] More commonly, strategies have been developed that involve the use of caging groups on the nucleosides to disrupt Watson-Crick base pairing and destabilize duplex formation until irradiation.[35,36] This strategy has been used widely for a variety of applications including siRNA,[37-39] peptide nucleic acids,[40,41] caged fluorescent oligonucleotides,[42] antisense oligonucleotides,[43-45] and miRNA.[43,46] A cartoon representation of these designs is represented in Figure 1-4 A-B.

Although caged nucleobases have proven effective towards light-activating hybridization based functions of oligonucleotides, drawbacks of this approach include the need for unique nucleobase monomers, which makes it difficult to design a generalizable method for caging. Another drawback to this method is that typically multiple caging groups are necessary to effectively disrupt hybridization which increases the light dose necessary for uncaging. This can be especially problematic since many of these designs use UV-active moieties, and high doses of UV irradiation can be damaging in biological systems. For these reasons, our lab and others have moved towards caged hairpin and circular caged designs.

A. Caged hairpin oligonucleotides

Caged hairpins consist of a biologically active strand and a shorter complementary strand, covalently attached with one or more photocleavable linkers. Through hybridization of a shorter blocking strand, the biologically active strand is rendered inactive. Covalent attachment of the two complementary sequences achieves a higher effective concentration, resulting in a higher thermal stability for the duplex. While covalently held in the hairpin structure, the biologically active strand is unable to bind to its target. Upon irradiation with UV light, the photolinker is cleaved which destabilizes the duplex. This results in duplex dissociation, and more favorable hybridization to the full length target. A schematic representation of a caged hairpin is shown in Figure 1-6A.

Our lab has designed and synthesized various caged hairpins, for RNase H-mediated mRNA digestion, antisense oligonucleotides, and most recently, for harvesting mRNA from single cells.[47] Additional examples for caged hairpins have been presented by the Chen lab.[48-50] One of the first examples published by Tang and Dmochowski reported a caged antisense DNA hairpin.[51] This hairpin blocked function of a 20-mer DNA when covalently attached to a blocking strand via a nitrobenzyl-based heterobifunctional photocleavable linker. Upon photocleavage with 365 nm light, antisense DNA was revealed to bind to target mRNA and recruit RNase H for mRNA degradation. This design was applied to target *c-myb*, a hematopoietic transcription factor in human K562 (leukemia) cells.[52] A similar design was applied to caging an 18-mer

antisense negatively charged peptide nucleic acid.[53] This caged antisense hairpin was used to photomodulate gene expression in zebrafish embryos for two early developmental genes, *chordin* and *bozozok*.

Additional efforts have been made towards caging antisense morpholinos, which are currently the gold standard in achieving gene knockdown in many model developmental organisms, including sea urchin, ascidian, zebrafish, frog, chick, and mouse.[54] Morpholinos (Figure 1-5) have been demonstrated to have high nuclease resistance due to their highly modified backbone. Initial reports of caging morpholinos by Shestopalov et al. involved a hairpin structure, where the morpholino, inhibitor sequence and dimethoxynitrobenzyl moiety were linked through a Cu(I)-catalyzed Huisgen 1,3-dipolar cycloaddition.[48] Additional features of this design included 3′ fluorescein for construct visualization *in vivo*. Successful photomodulation of zebrafish *notail* was achieved with this design. Following up on this design, Shestopalov et al. reported an additional caged morpholino with a simplified synthesis.[49,50] A DMNB-based bifunctional linker was used to conjugate the antisense morpholino and its complementary inhibitor strand in three steps, starting with commercially available morpholinos. Generalizable methods pertaining to inhibitor placement and length optimization were also explored. Additionally, a bromohydroxyquinoline (BHQ)-based linker for two-photon uncaging was presented.

B. Circular caged oligonucleotides

More recently, caging of short oligonucleotides has been achieved through circularization.[55-59] By covalently attaching the 5′ and 3′ ends of the oligonucleotide with a photocleavable linker so that it forms a circular structure, the oligonucleotide is structurally restricted from hybridizing to a complementary target. A cartoon representation of this design is shown in Figure 1-6. This design has many benefits that arise from the lack of a blocking sequence. Primarily, the circularization scheme is sequence independent. Additionally, there is no risk of the blocking strand having biological activity and off-target effects after photolysis and dissociation. As there is only one photocleavable linker in most circular designs, this significantly lowers the light dose necessary for uncaging.

Initial reports of circular oligonucleotides were by Richards *et al.* where a photolabile circular DNAzyme was enzymatically synthesized using T4 ligase and photomodulation of RNA digestion was achieved.[58] Tang et al. presented the first example of photomodulating RNA digestion by RNase H through the synthesis of light-activated circular DNA antisense oligonucleotides.[57] The first example of a caged circular morpholino was reported by Yamazoe et al.,[55] shortly followed by Wang et al. who also caged a 25-mer morpholino by linking the two ends in a circular structure with a nitrobenzyl photocleavable moiety.[56] These caged cMOs were successfully used to photomodulate early developmental genes in zebrafish embryos with 365 nm light.

Yamazoe et al. compared background activity between circular and hairpin structures and found significantly less background activity in vivo with circular constructs.

C. Other designs of caged oligonucleotides

Another method for caging oligonucletides reported by the Dmochowski lab is an "RNA bandage" design that provides a method of blocking mRNA translation and restoring it upon irradiation with UV light.[60] These constructs perform opposite of the previously described caged hairpins and circular caged oligonucleotides, as they can regulate gene expression from "off to on" as opposed to "on to off". A schematic representation is shown in Figure 1-7A. Bandages were designed and synthesized using 2′-OMe RNA antisense oligonucleotides and linked by a nitrobenzyl-based photocleavable moiety that activates with 365 nm irradiation. These RNA bandages were demonstrated to be successful at photomodulating in vitro translation.

A similar design strategy was implemented by Tallafuss et al. to cage an antisense morpholino.[61] In this design, two shorter blocking sequences were linked with a nitrobenzyl photocleavable moiety and hybridized to a 25-mer target morpholino for turning genes from "off to on" with light (Figure 1-7A). Additionally, this design can be used for "on to off" gene photomodulation by linking two shorter MO sequences together with a nitrobenzyl moiety to form a full length active morpholino that is able to bind to an mRNA target (Figure 1-7B). Upon UV light exposure, the two shorter MO sequences

are liberated, resulting in dissociation from the mRNA. This technology is commercially available through Gene Tools (Philomath, Oregon).

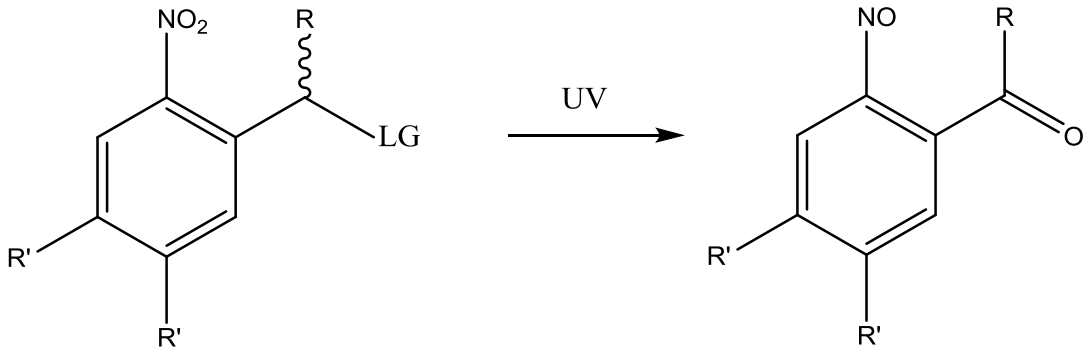

ONB: R = H
NPE: R = Me
CNB: R = COOH
Nv: R' = H
DMNB: R' = OMe

Figure 1-1. Structure of *o*-nitrobenzyl and derivatives

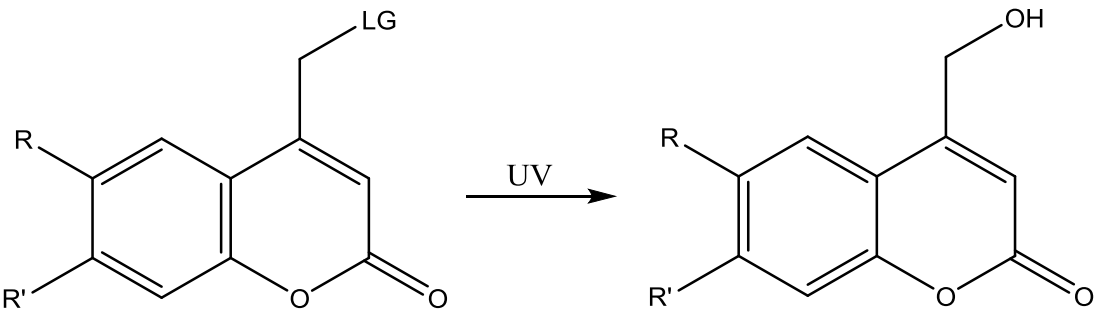

Coumarin: R = H, R' = OMe
Bhc: R = Br, R' = OH

Figure 1-2. Structure of MCM ester (coumarin) and derivative, brominated 7-hydroxycoumarin-4-ylmethyl ester (Bhc).

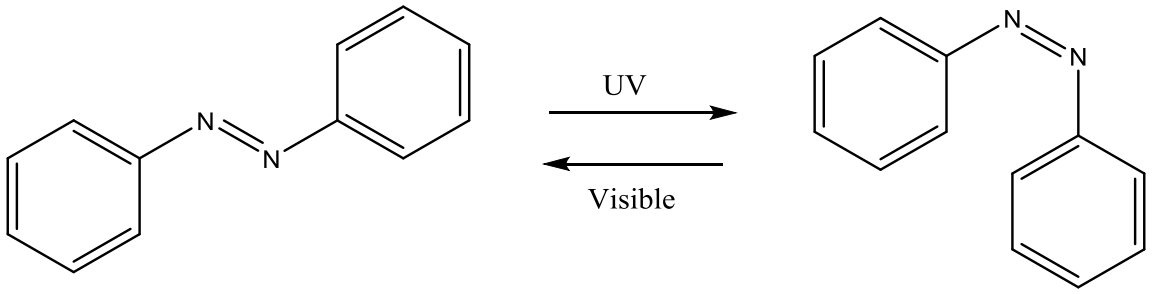

Figure 1-3. Azobenzene structure

Azobenzene changes from *trans*-*cis* configuration upon UV irradiation and *cis*-*trans* thermally, or upon visible irradiation.

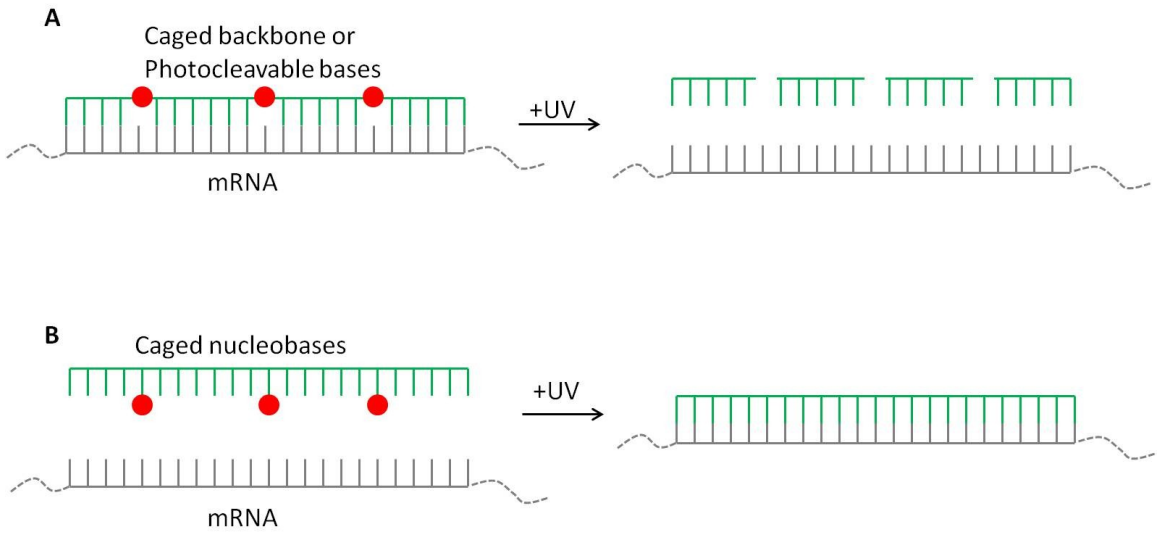

Figure 1-4. Cartoon representation of A) caged backbone, or photocleavable bases and B) caged nucleobases.

A) The oligonucleotide hybridizes to the target (depicted as mRNA) until irradiated with UV light. B) Caging groups on bases disrupt Watson-Crick base pairing until irradiation with UV light. Caging groups are shown in red, antisense oligonucleotide sequence is shown in green, and target (mRNA) is shown in gray.

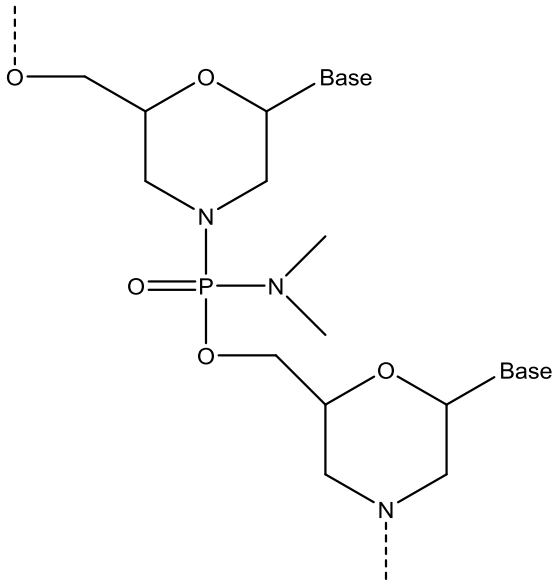

Figure 1-5. Structure of antisense morpholino

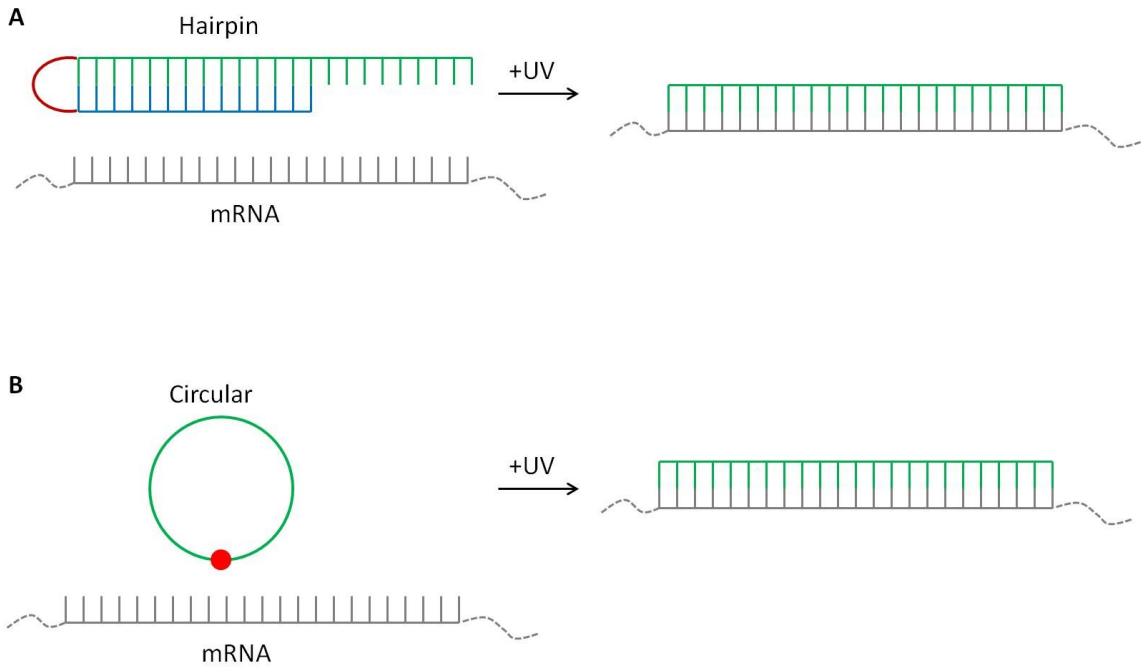

Figure 1-6. Cartoon representation of A) caged antisense hairpin and B) circular antisense oligonucleotide.

A) An antisense sequence is covalently attached to a blocking sequence by a photocleavable linker. This blocking sequence can vary in length and placement. B) An antisense sequence is covalently held in a circular structure to prevent target binding. Upon UV irradiation, the antisense oligonucleotide is liberated and able to hybridize to a complementary target. Caging groups are shown in red, antisense oligonucleotide sequence is shown in green, blocking sequence is shown in blue, and target (mRNA) is shown in gray.

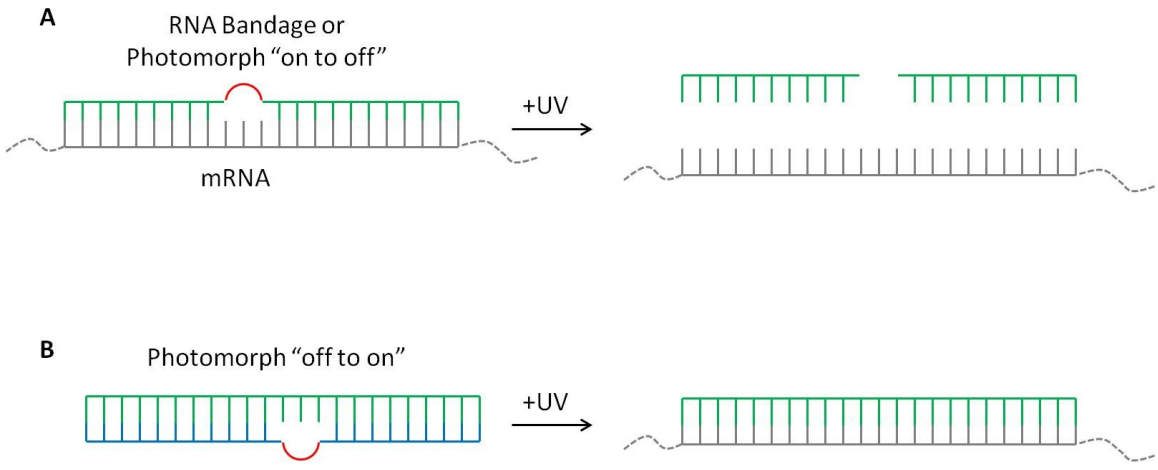

Figure 1-7. Cartoon representation of A) RNA bandage or Photomorph and B) Photomorph "off to on" antisense oligonucleotide.

A) Two shorter antisense sequences are joined by a photocleavable group to form a full length sequence that can hybridize to target mRNA. Upon irradiation, shorter sequences dissociate and liberate mRNA. B) Two shorter blocking sequences are joined by a photocleavable group to form a full length sequence that can hybridize block morpholino function. Upon irradiation, shorter sequences dissociate and activate the morpholino. Caging groups are shown in red, antisense oligonucleotide sequence is shown in green, blocking sequence is shown in blue, and target (mRNA) is shown in gray.

III. Moving away from ultraviolet light activation

A. One-photon vs. two-photon activation

The primary goal of caged compounds is the ability to control biological processes with light with high spatiotemporal resolution. Although much progress has been made towards this goal through the use of 1-photon active moieties such as the UV active *o*-nitrobenzyl group and derivatives, significant improvements can be achieved with the implementation of two-photon photolinkers. The use of 2-photon activation in caged compounds can provide even greater spatial resolution in three dimensions through the addition of depth control.[62]

Two-photon photolysis replaces the absorption of one photon with two longer-wavelength, lower-energy photons, typically in the NIR region, of equivalent total energy. The simultaneous absorption of these photons is governed by the light intensity and the two-photon absorption cross section, measured in GM (Göppert-Mayer). A GM is equal to 10^{-50}cm^4 s photon^{-1}, therefore, confining the uncaging event to a very small region of focus with negligible out of focus irradiation.[63] This allows for uncaging in very small regions of interest and volumes as small as 1 femtoliter.[4] Additional benefits of NIR light used for two-photon uncaging is significantly less scattering than shorter wavelength light, and less damage to biological systems compared to UV light.[64]

B. Two-photon photolinkers

Nitrobenzyl and coumarin derivatives have been shown to be two-photon active, however their two-photon absorption cross sections are very low, in the 0.01 - 0.1 GM range.[65] Although NIR light is significantly less damaging than UV light, high laser powers required to activate compounds with such low two-photon cross sections result in heating and toxicity due to water strongly absorbing 700-900 nm light.[66] For this reason, it is necessary to develop two-photon caging groups with significantly higher cross-sections (3-30 GM).[63]

There are few applications that have been demonstrated for two-photon caged biomolecules, likely due to the limited availability of two-photon caging groups. Some examples of two-photon caged compounds using coumarin derivatives are caged calcium, azid-1,[67] and caged glutamate.[68] Although successful two-photon uncaging has been achieved with these caged compounds,[69,70] cross-sections were measured to be below the 3 - 30 GM target level, therefore requiring high levels of laser power.[4]

C. $[Ru(bpy)_2XY]^{n+}$ ligand dissociation with visible and two-photon light

Octahedral Ru(II) polypyridyl complexes have been shown to be a promising method of caging molecules for release with visible and two-photon excitation. Specifically, complexes of the type $[Ru(bpy)_2XY]^{n+}$, a Ru(II) center with two bipyridines and two monodentate ligands (Figure 1-8), undergo photochemistry resulting in the photodissociation of one or both monodentate ligands.[71] Initial reports of these complexes

were published by Dwyer et al.,[72] with in-depth photochemical studies followed two decades later.[73] Photochemical reactions typically follow equation (1) and sometimes also equation (2), where X and Y are monodentate ligands, and S is solvent.

$$Ru(bpy)_2XY^{n+} + S \xrightarrow{h\nu} Ru(bpy)_2YS^{n+} + X \quad (1)$$

$$Ru(bpy)_2YS^{n+} + S \xrightarrow{h\nu} Ru(bpy)_2S_2^{n+} + Y \quad (2)$$

A general mechanism of photorelease is demonstrated through the Jablonski diagram in Figure 1-9. Upon irradiation, absorption into the MLCT (typically 400-500 nm) populates the single ^{1}MLCT band. Intersystem crossing (ISC) occurs, populating the triplet ^{3}MLCT state. This process occurs very rapidly, on the order of 40 fs measured for $Ru(bpy)_3^{2+}$.[74] Decay can occur through multiple pathways, non-radiative (nr), radiative (rad), and in the case of $[Ru(bpy)_2XY]^{n+}$, cross-over to the ligand field (^{3}LF) state where ligand dissociation occurs.[75] Population of the ligand field state is thermally activated, and directly correlates with the energy gap between ^{3}MLCT and ^{3}LF. At a given temperature, a higher energy ^{1}MLCT results in a higher energy ^{3}MLCT band and thus, a smaller gap between ^{3}MLCT and ^{3}LF. This results in a blue-shifted MLCT ground-state absorption band and therefore, a higher yield of photosubstitution (i.e., a higher quantum yield). In contrast, a larger gap between the ^{3}MLCT and ^{3}LF will result in lower quantum yields of photosubstitution.[75]

D. $[Ru(bpy)_2(X)_2]^{2+}$ as a photolinker

The tunable photophysical properties of $[Ru(bpy)_2XY]^{n+}$ make these complexes very attractive for caging applications. The MLCT in the visible region is beneficial for use in biological systems, as visible light is far less damaging to cells, and also penetrates tissue samples deeper due to the longer wavelength.[71] Additionally, as shown in Scheme 1-1, the mechanism of uncaging is through a ligand-exchange process instead of a photo-cleavage process which allows for very clean and efficient whole-molecule uncaging. Many examples of whole-molecule caging with these ruthenium complexes have been presented in the literature.

The first example of ruthenium caging of a biologically relevant molecule was presented by Zayat et. al. in 2003 with the caging of 4-aminopyridine.[76] In this example, 4-aminopyridine (4-AP), a neurocompound that blocks K^+ channels,[77] was cooordinated directly to $Ru(bpy)_2Cl_2$ through the amine. The resulting water-soluble compound, $[Ru(bpy)_2(4\text{-}AP)_2]Cl_2$ had a MLCT centered at 489 nm and underwent successful uncaging, as confirmed by a free 4-AP ligand seen by ^1H NMR spectroscopy. Experiments using $[Ru(bpy)_2(4\text{-}AP)_2]Cl_2$ showed successful uncaging and neuronal stimulation in a leech ganglion, with no toxicity observed. Additional compounds were designed by the Etchenique lab using similar strategies, including a cholinergic agonist nicotine, $[Ru(bpy)_2(Nic)_2]^{2+}$,[78] and a caged γ-aminobutyric acid (GABA).[79] These caged compounds all coordinated to the ruthenium through an amine.

The octahedral ruthenium center on $[Ru(bpy)_2XY]^{n+}$ provides flexibility in coordination chemistry. The choice of ligand depends primarily on the desired photophysical characteristics, such as wavelength and quantum yield, providing excellent potential for designing photolinkers. Selecting ligands that are much weaker σ-donors will result in an electronically depleted Ru(II) center, thus, shifting the activation to higher energy (shorter wavelengths). This blue-shifting results in a significantly higher quantum yield.[80] Another consideration is whether or not one or both monodentate ligands will dissociate. This also depends on the electronics of the ligands. For example, if X and Y are different ligands, substitution will occur at the ligand that is a weaker σ-donor. In cases where the monodentate ligands are identical, the substitution will proceed on one ligand to form the mono-aquo product, unless the ligand is a weaker σ-donor than the solvent, in which case both ligands will be exchanged.[71]

Another benefit of using $[Ru(bpy)_2XY]^{n+}$ compounds as photolinkers is their demonstrated two-photon activation. Salierno et al. presented a caged glutamate, $Ru(bpy)_2(PMe_3)(Glu)$, which could be efficiently uncaged with one-photon (450 nm) or two-photon (800 nm) light.[81] The two-photon cross section for this caged glutamate was determined to be 0.14 GM. Additional examples of two-photon activation of $[Ru(bpy)_2XY]^{n+}$ compounds include the two-photon uncaging of a caged dopamine, $[Ru(bpy)_2(PMe_3)(Dopa)](PF_6)_2$ which has an even higher two-photon cross-section of 0.24 GM.[82] These two-photon cross sections are significantly higher than what has been reported for two-photon activation of nitrobenzyl or coumarin derivatives, and there.is

potential for tuning the Ru ligands to achieve the desired 3-30 GM target. Compounds of the type $[Ru(bpy)_2XY]^{n+}$ are promising for developing a library of photoactive moieties, as they are widely tunable depending on the coordinated ligands.

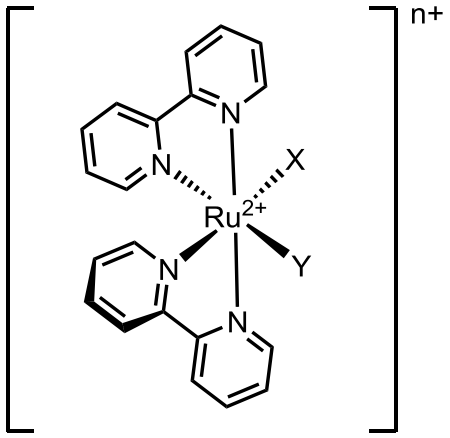

Figure 1-8. General structure of $[Ru(bpy)_2XY]^{n+}$ complexes

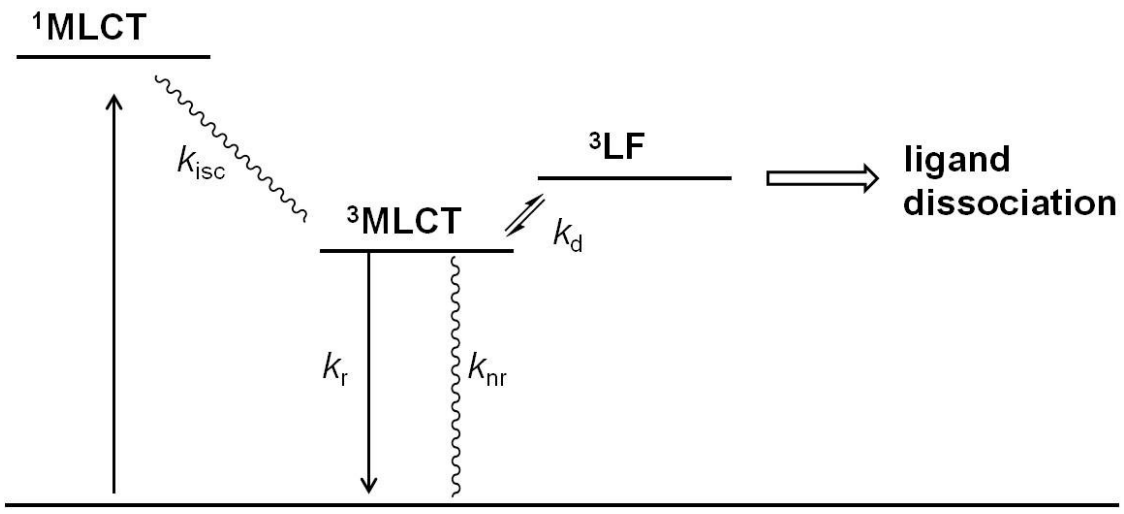

Figure 1-9. Jablonski diagram showing mechanism of photo-triggered ligand dissociation

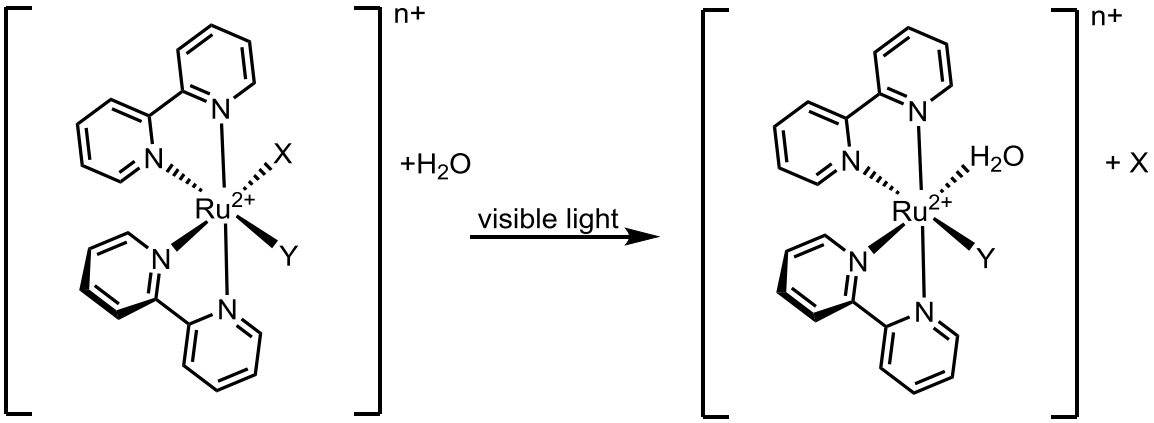

Scheme 1-1. General scheme for single ligand exchange of $[Ru(bpy)_2XY]^{n+}$ in H_2O

IV. Light-activated polymersomes

A. Introduction to polymersomes

Polymersomes are a class of synthetic vesicles that self-assemble from amphiphilic diblock copolymers.[83] Polymersomes have attracted much attention since their initial discovery by Hammer, Discher, and Eisenberg a little over a decade ago[84,85] due to their robustness, tunability, ability to mimic biological membranes and the ability to encapsulate a broad variety of molecules. Polymersomes are composed of two components, a large hollow aqueous core, and a thick hydrophobic membrane which separates the aqueous core from the outer medium. These two structural components provide versatility in encapsulation possibilities, from hydrophobic drugs (ie, paclitaxel, doxorubicin, quantum dots) encapsulated in the membrane, to small molecules and large biomolecules (i.e., siRNA, DNA, plasmids, proteins, enzymes) encapsulated in the aqueous core.

Polymersomes have many benefits over liposomes as carrier systems, namely, they are fully synthetic which provides the possibility to tune many characteristics such as membrane thickness, vesicle size, and vesicle composition. Since polymersomes are comprised of high molecular weight polymers as opposed to small phospholipids like liposomes, membrane thickness typically spans from 3-30 nm in comparison to 3-5 nm.[83] These high molecular weights also offer benefits such as decreased membrane permeability and enhanced mechanical strength. Additionally, polymersomes have been

shown to have significantly longer circulation times *in vivo* than unmodified liposomes.[86] Circulation time of liposomes is typically on the order of hours,[87] but can be increased by functionalizing the outer surface with poly(ethylene glycol) (PEG), known as "stealth liposomes".[88] In contrast, polymersomes have intrinsically long circulation times due to their composition.

Polymersomes can generally be prepared by two different methods, phase-inversion, and polymer rehydration. The phase-inversion technique involves dissolving the diblock copolymer in an organic solvent, followed by hydration with aqueous solvent. Typically, this process yields fairly uniform nanovesicles that can be tuned through polymer concentration and organic-to-water ratio.[83] This process results in self-assembly by increasing the interfacial tension between the hydrophobic polymer blocks and the hydration solution. The polymer rehydration method involves dissolving the diblock copolymer in organic solvent and forming a thin film by evaporation of the organic solvent. Self-assembly is promoted by hydration with water. With the polymer rehydration technique, vesicles are formed as the water permeates the polymer film through defects, causing the polymer to lift from the surface. Polymer rehydration typically yields larger vesicles that can be made smaller and more uniform through extrusion.[89]

B. Light-activated polymersomes

Much attention has been dedicated to designing "smart" polymersomes, or polymersomes that respond to a stimulus to release cargo. This stimulus can be an

internal or external trigger such as degradation by hydrolysis, temperature, pH, magnetic fields, or light.[90] This review will focus on examples of polymersomes that undergo membrane disruptions in response to light. Light-responsive polymersomes are an attractive method of controlled release because light can be easily externally manipulated for release of cargo with high spatial and temporal resolution.

One such system by Mabrouk et al. used an azobenzene group incorporated within the diblock copolymer to promote rapid membrane disruptions in response to UV light.[91] Asymmetric micron-sized polymersomes were assembled through two block copolymers, an inert copolymer, polyethyleneglycol-polybutadiene (PEG-b-PBD), and a liquid crystal based copolymer, PEG-b-PMAazo444 (PAzo). The liquid crystal block contained an azobenzene group which underwent a *trans*-to-*cis* configurational transition in response to UV light. The isomerization caused a conformational change in the block from a rod to a coil, which induced an area difference between the two polymer monolayers sufficient to trigger membrane rupture.

Another example of a light-responsive micron-sized polymersome system was presented by Robbins et al.[92] This system was the first example of a photoactive polymersome formed by incorporating a protein in the aqueous interior and a meso-to-meso ethyne-bridged bis[(porphinato)zinc] (PZn_2) chromophore in the membrane. Micron-size vesicles were self-assembled using a polyethylene oxide-polybutadiene (PEO_{30}-PBD_{46}, denoted OB29) diblock copolymer. Two different proteins, horse spleen ferritin (HSF) or iron-free apoferritin (HSAF), were encapsulated within the aqueous

core. Incorporation of the PZn_2 chromophore into the vesicle's hydrophobic membrane allowed for light absorption of near-UV to near-IR wavelengths. Irradiation with 488, 543, and 633 nm induced irreversible membrane deformities ranging from "budding" to complete rupture. It was hypothesized that the protein associated with the inner membrane, causing asymmetrical membrane deformation upon PZn_2 energy dissipation as heat, which ultimately resulted in membrane rupture. A small molecule, biocytin, was encapsulated within the core and 25-50% release was demonstrated upon light exposure.

The work by Robbins et al.[92] was further explored by Kamat et al.[93] and subsequently resulted in a general method for producing photoresponsive micron-sized vesicles with chromophore PZn_2 in the hydrophobic membrane. Following up on the work by Robbins et al., it was hypothesized that any luminal solute that associates with the inner leaflet of the membrane can induce polymersome rupture when combined with PZn_2 in the membrane. Dextran was investigated as a luminal encapsulant due to its biocompatibility and aqueous solubility. It was shown that inclusion of dextran could induce membrane instability upon irradiation. Studies were performed varying the size of the dextran and molecular weight of the polymer, and it was shown that photoresponsiveness increased with molecular weight and dextran concentration. Additional work by Kamat et al. explored this system for use as a membrane stress sensor.[94] cIt was demonstrated that PZn_n fluorophores underwent significant red emission shifts as a response to environmental crowding within a polymersome membrane.

To date, only one example exists of a photoresponsive nanoscale polymersome. It is important to develop light-responsive vesicles on the nano-scale for biological applications, as micron vesicles are not sized appropriately for *in vivo* experiments. Mammalian cells, such as HeLa cells, are typically 10-20 μM in diameter, therefore it is necessary to develop much smaller carrier systems for these applications. Additionally, passive uptake of polymer-based nanoparticles by red blood cells has been shown to occur for particles less than 200 nm.[95]

Cabane et al. presented a photocleavable amphiphilic diblock copolymer, poly(methyl caprolactone)-ONB-poly(acrylic acid) (PMCL-ONB-PAA) that self-assembled into micelles and 150 nm polymersomes.[96] qcThis block copolymer contained an *o*-nitrobenzyl moiety as a photocleavable linker between the hydrophilic and hydrophobic polymer chains. UV-irradiation induced a successful cleavage of the diblock copolymer chains, both in THF and aqueous solution, as well as in self-assembled vesicles. This work was further extended to probe the ability of this system to encapsulate and release two small molecules, as well as a large biomolecule, green fluorescent protein.[97] Irradiation with 365 nm light induced polymersome disintegration within minutes. Upon irradiation, cargo was released and polymersome morphology was shown by cryo-TEM to transition from vesicles to micelles. This nanoscale system provides a promising route to deliver cargo *in vivo* with UV light, and can be tuned for delivery needs by altering the number of photocleavable moieties in the polymer.

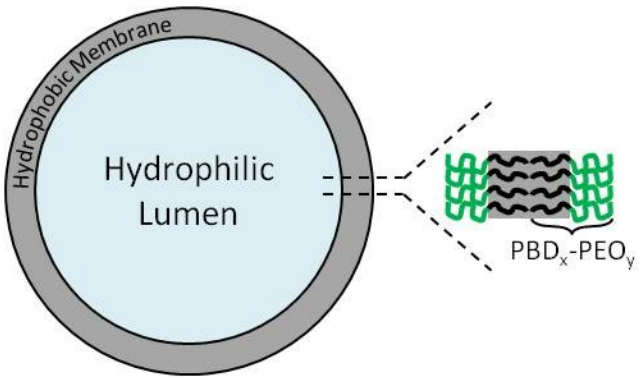

Figure 1-11. General schematic of a polymersome.

The hydrophobic membrane, shown in gray, is composed of a hydrophobic polymer (black) and hydrophilic polymer (green). A common diblock copolymer used for polymer self assembly is PBD_x-PEO_y. The hydrophilic lumen for encapsulating cargo is shown in blue.

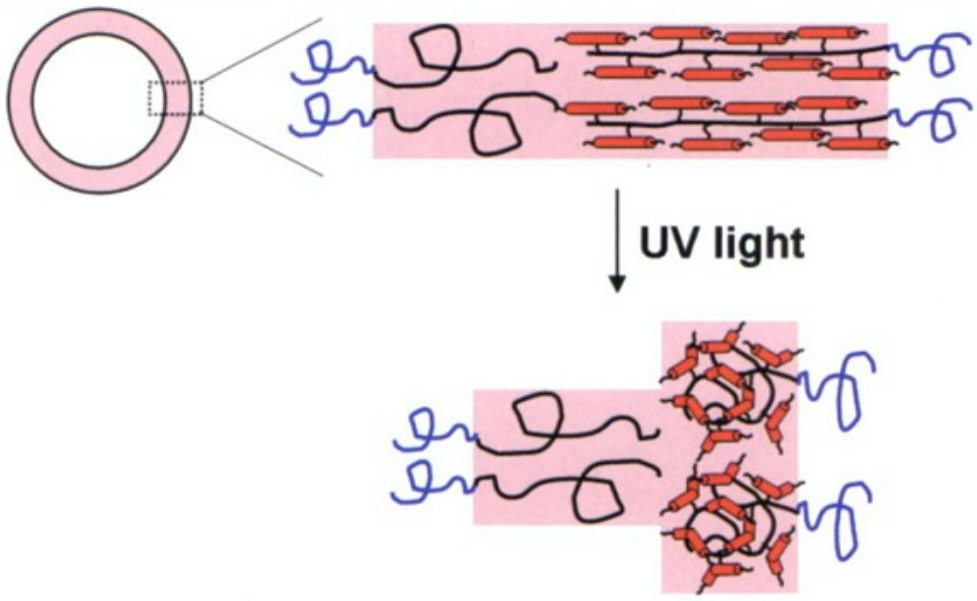

Figure 1-12. Cartoon of a PEG-b-PBD/PEG-b-PMAzo444 polymersome and response to UV light.

Under UV illumination, isomerization of the azobenzene induces a conformational change of the diblock copolymer, resulting in vesicle rupture.

Figure adapted from E. Mabrouk. et. al. P.N.A.S. 2009, 106, 7294-7298

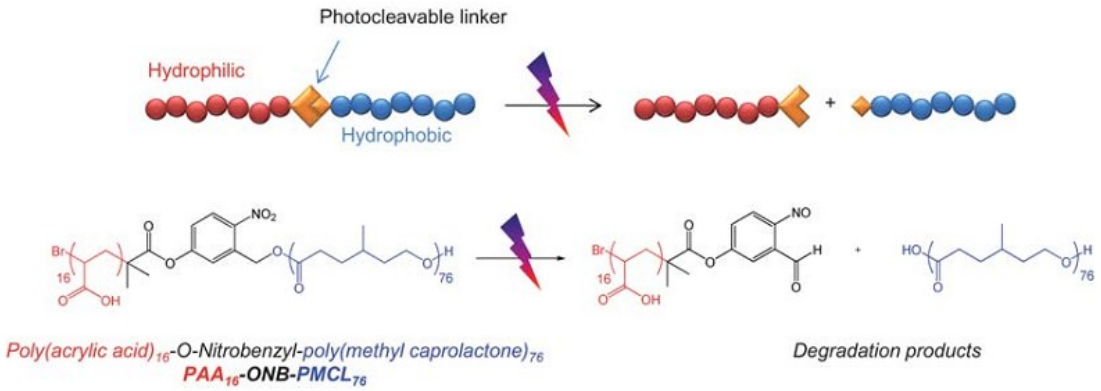

Figure 1-13. Nitrobenzyl-linked light-responsive polymersome.

Chemical structure of the poly(methyl caprolactone)-ONB-poly(acrylic acid) diblock copolymer and degradation products upon UV irradiation are shown.

Figure adapted from E. Cabane et. el. *Soft Matter*, 2011, 7, 9167–9176

V. Research Aims

Work presented in this thesis demonstrates three unique designs for biomolecular caging, all responsive to different wavelengths of light. The first two designs involve the site-specific incorporation of a caging moiety, and the third design involves encapsulation within a light-activated polymersome nanocarrier. Specifically, Chapter 2 presents a caged antagomir for the regulation of *let-7* miRNA, in zebrafish embryos. This caged antagomir provides the ability to block the activity of a miRNA *in vivo* upon photoactivation with 365 nm light. Additionally, Chapter 2 presents a caged miRNA, providing a method of introducing an exogenous miRNA into zebrafish embryos and activating it upon irradiation. Used together, these two constructs provide the ability for bidirectional control of a miRNA. Chapter 3 focuses on the design, synthesis, and application of a ruthenium-based visible-light photolinker, RuBEP. Two antisense morpholinos were circularized with RuBEP through click-chemistry, and activated in zebrafish embryos with 450-nm light. Chapter 3 demonstrates an encapsulation-based approach for caging through the use of photo-responsive nano-polymersomes. These nano-polymersomes were used to encapsulate oligonucleotides, small molecules (FITC), and metal ions (Zn^{2+} and Ca^{2+}) and cargo was released with 488 nm light.

VI. References

(1) Kaplan, J. H.; Forbush, B.; Hoffman, J. F. *Biochemistry* **1978**, *17*, 1929-1935.

(2) Karrer, P.; Keller, P.; Szönyi, G. *Helv. Chim. Acta* **1943**, *26*, 38-50.

(3) Denk, W.; Strickler, J. H.; Webb, W. W. *Science* **1990**, *248*, 73-76.

(4) Brown, E. B.; Shear, J. B.; Adams, S. R.; Tsien, R. Y.; Webb, W. W. *Biophys. J.* **1999**, *76*, 489-499.

(5) Mayer, G.; Heckel, A. *Angew. Chem., Int. Ed. Engl.* **2006**, *45*, 4900-4921.

(6) Sinha, R. P.; Hader, D.-P. *Photochem. Photobiol. Sci.* **2002**, *1*, 225-236.

(7) Weissleder, R. *Nat. Biotech.* **2001**, *19*, 316-317.

(8) Shao, Q.; Xing, B. *Chem. Soc. Rev.* **2010**, *39*, 2835-2846.

(9) Barltrop, J. A.; Plant, P. J.; Schofield, P. *Chem. Commun. (London)* **1966**, 822-823.

(10) Patchornik, A.; Amit, B.; Woodward, R. B. *J. Am. Chem. Soc.* **1970**, *92*, 6333-6335.

(11) Corrie, J. E. T.; Furuta, T.; Givens, R.; Yousef, A. L.; Goeldner, M. In *Dynamic Studies in Biology*; Wiley-VCH Verlag GmbH & Co. KGaA: 2005, p 1-94.

(12) Schaper, K.; Madani Mobarekeh, S. A.; Doro, P.; Maydt, D. *Photochem. Photobiol.* **2010**, *86*, 1247-1254.

(13) Bao, C.; Jin, M.; Li, B.; Xu, Y.; Jin, J.; Zhu, L. *Org. Biomolec. Chem.* **2012**, *10*, 5238-5244.

(14) Olejnik, J.; Krzymanska-Olejnik, E.; Rothschild, K. J. *Nucleic Acids Res.* **1996**, *24*, 361-366.

(15) Olejnik, J.; Krzymanska-Olejnik, E.; Rothschild, K. J. *Nucleic Acids Res.* **1998**, *26*, 3572-3576.

(16) Givens, R. S.; Matuszewski, B.; Athey, P. S.; Stoner, M. R. *J. Am. Chem. Soc.* **1990**, *112*, 6016-6021.

(17) Furuta, T.; Wang, S. S.-H.; Dantzker, J. L.; Dore, T. M.; Bybee, W. J.; Callaway, E. M.; Denk, W.; Tsien, R. Y. *Proc. Natl. Acad. Sci. U. S. A.* **1999**, *96*, 1193-1200.

(18) Kotzur, N.; Briand, B.; Beyermann, M.; Hagen, V. *J. Am. Chem. Soc.* **2009**, *131*, 16927-16931.

(19) Yamazoe, S.; Liu, Q.; McQuade, L. E.; Deiters, A.; Chen, J. K. *Angew. Chem., Int. Ed. Engl.* **2014**, n/a-n/a.

(20) Bandara, H. M. D.; Burdette, S. C. *Chem. Soc. Rev.* **2012**, *41*, 1809-1825.

(21) Asanuma, H.; Liang, X.; Yoshida, T.; Komiyama, M. *ChemBioChem* **2001**, *2*, 39-44.

(22) Asanuma, H.; Matsunaga, D.; Liu, M.; Liang, X.; Jhao, J.; Komiyama, M. *Nucleic Acids Res.* **2003**, 117-118.

(23) Liang, X.; Yoshida, T.; Asanuma, H.; Komiyama, M. *Nucleic Acids Symp. Ser.* **2000**, 277-278.

(24) del Barrio, J.; Oriol, L.; Sanchez, C.; Serrano, J. L.; Di Cicco, A.; Keller, P.; Li, M. H. *J. Am. Chem. Soc.* **2010**, *132*, 3762-3769.

(25) Mabrouk, E.; Cuvelier, D.; Brochard-Wyart, F.; Nassoy, P.; Li, M.-H. *Proc. Natl. Acad. Sci. U. S. A.* **2009**, *106*, 7294-7298.

(26) Li, M.-H.; Auroy, P.; Keller, P. *Liq. Cryst.* **2000**, *27*, 1497-1502.

(27) Ellis-Davies, G. C. R. *Chem. Rev.* **2008**, *108*, 1603-1613.

(28) Shigeri, Y.; Tatsu, Y.; Yumoto, N. *Pharmacol. Ther.* **2001**, *91*, 85-92.

(29) Tang, X.; Dmochowski, I. J. *Molecular BioSyst.* **2007**, *3*, 100-110.

(30) Riggsbee, C. W.; Deiters, A. *Trends Biotechnol.*, *28*, 468-475.

(31) Monroe, W. T.; McQuain, M. M.; Chang, M. S.; Alexander, J. S.; Haselton, F. R. *J. Biol. Chem.* **1999**, *274*, 20895-20900.

(32) Ando, H.; Furuta, T.; Tsien, R. Y.; Okamoto, H. *Nat. Genet.* **2001**, *28*, 317-325.

(33) Ordoukhanian, P.; Taylor, J.-S. *J. Am. Chem. Soc.* **1995**, *117*, 9570-9571.

(34) Dussy, A.; Meyer, C.; Quennet, E.; Bickle, T. A.; Giese, B.; Marx, A. *ChemBioChem* **2002**, *3*, 54-60.

(35) Heckel, A. In *Curr. Protoc. Nucleic Acid Chem.*; John Wiley & Sons, Inc.: 2001.

(36) Buff, M.; Mack, T.; Heckel, A. *CHIMIA* **2009**, *63*, 261-264.

(37) Mikat, V.; Heckel, A. *RNA* **2007**, *13*, 2341-2347.

(38) Govan, J. M.; Young, D. D.; Lusic, H.; Liu, Q.; Lively, M. O.; Deiters, A. *Nucleic Acids Res.* **2013**, *41*, 10518-10528.

(39) Wu, L.; Pei, F.; Zhang, J.; Wu, J.; Feng, M.; Wang, Y.; Jin, H.; Zhang, L.; Tang, X. *Chemistry* **2014**.

(40) Guha, S.; Graf, J.; Goricke, B.; Diederichsen, U. *J. Pept. Sci.* **2013**, *19*, 415-422.

(41) Watanabe, T.; Hoshida, T.; Sakyo, J.; Kishi, M.; Tanabe, S.; Matsuura, J.; Akiyama, S.; Nakata, M.; Tanabe, Y.; Suzuki, A. Z.; Watanabe, S.; Furuta, T. *Org. Biomol. Chem.* **2014**, *12*, 5089-5093.

(42) Tang, X.; Dmochowski, I. J. *Org. Lett.* **2005**, *7*, 279-282.

(43) Connelly, C. M.; Uprety, R.; Hemphill, J.; Deiters, A. *Molecular BioSyst.* **2012**, *8*, 2987-2993.

(44) Deiters, A.; Garner, R. A.; Lusic, H.; Govan, J. M.; Dush, M.; Nascone-Yoder, N. M.; Yoder, J. A. *J. Am. Chem. Soc.* **2010**, *132*, 15644-15650.

(45) Young, D. D.; Lusic, H.; Lively, M. O.; Yoder, J. A.; Deiters, A. *ChemBioChem* **2008**, *9*, 2937-2940.

(46) Connelly, C.; Deiters, A. In *Cancer Cell Signaling*; Robles-Flores, M., Ed.; Springer New York: 2014; Vol. 1165, p 99-114.

(47) Lovatt, D.; Ruble, B. K.; Lee, J.; Dueck, H.; Kim, T. K.; Fisher, S.; Francis, C.; Spaethling, J. M.; Wolf, J. A.; Grady, M. S.; Ulyanova, A. V.; Yeldell, S. B.; Griepenburg, J. C.; Buckley, P. T.; Kim, J.; Sul, J.-Y.; Dmochowski, I. J.; Eberwine, J. *Nat. Methods* **2014**, *11*, 190-196.

(48) Shestopalov, I. A.; Sinha, S.; Chen, J. K. *Nat. Chem. Biol.* **2007**, *3*, 650-651.

(49) Ouyang, X.; Shestopalov, I. A.; Sinha, S.; Zheng, G.; Pitt, C. L.; Li, W. H.; Olson, A. J.; Chen, J. K. *J. Am. Chem. Soc.* **2009**, *131*, 13255-13269.

(50) Shestopalov, I. A.; Chen, J. K. *Methods Cell Biol.* **2011**, *104*, 151-172.

(51) Tang, X.; Dmochowski, I. J. *Angew. Chem., Int. Ed. Engl.* **2006**, *45*, 3523-3526.

(52) Tang, X.; Swaminathan, J.; Gewirtz, A. M.; Dmochowski, I. J. *Nucleic Acids Res.* **2008**, *36*, 559-569.

(53) Tang, X.; Maegawa, S.; Weinberg, E. S.; Dmochowski, I. J. *J. Am. Chem. Soc.* **2007**, *129*, 11000-11001.

(54) Heasman, J. *Dev. Biol.* **2002**, *243*, 209-214.

(55) Yamazoe, S.; Shestopalov, I. A.; Provost, E.; Leach, S. D.; Chen, J. K. *Angew. Chem., Int. Ed. Engl.* **2012**, *51*, 6908-6911.

(56) Wang, Y.; Wu, L.; Wang, P.; Lv, C.; Yang, Z.; Tang, X. *Nucleic Acids Res.* **2012**, *40*, 11155-11162.

(57) Tang, X.; Su, M.; Yu, L.; Lv, C.; Wang, J.; Li, Z. *Nucleic Acids Res.* **2010**, *38*, 3848-3855.

(58) Richards, J. L.; Seward, G. K.; Wang, Y. H.; Dmochowski, I. J. *ChemBioChem* **2010**, *11*, 320-324.

(59) Griepenburg, J. C.; Ruble, B. K.; Dmochowski, I. J. *Bioorg. Med. Chem.* **2013**, *21*, 6198-6204.

(60) Richards, J. L.; Tang, X.; Turetsky, A.; Dmochowski, I. J. *Bioorg. Med. Chem. Lett.* **2008**, *18*, 6255-6258.

(61) Tallafuss, A.; Gibson, D.; Morcos, P.; Li, Y.; Seredick, S.; Eisen, J.; Washbourne, P. *Development* **2012**, *139*, 1691-1699.

(62) Denk, W.; Strickler, J.; Webb, W. *Science* **1990**, *248*, 73-76.

(63) Pelliccioli, A. P.; Wirz, J. *Photochem. Photobiol. Sci.* **2002**, *1*, 441-458.

(64) Fomina, N.; McFearin, C. L.; Sermsakdi, M.; Morachis, J. M.; Almutairi, A. *Macromolecules* **2011**, *44*, 8590-8597.

(65) Aujard, I.; Benbrahim, C.; Gouget, M.; Ruel, O.; Baudin, J. B.; Neveu, P.; Jullien, L. *Chemistry* **2006**, *12*, 6865-6879.

(66) Tsai, C.-L.; Chen, J.-C.; Wang, W.-J. *Med. Biol. Eng.* **2001**, *21*, 7-14.

(67) Adams, S. R.; Lev-Ram, V.; Tsien, R. Y. *Chem. Biol.* **1997**, *4*, 867-878.

(68) Pettit, D. L.; Wang, S. S.; Gee, K. R.; Augustine, G. J. *Neuron* **1997**, *19*, 465-471.

(69) Matsuzaki, M.; Ellis-Davies, G. C.; Kasai, H. *J. Neurophysiol.* **2008**, *99*, 1535-1544.

(70) Konishi, M.; Yamashita, T.; Nakayama, S.; Kokubun, S. *Jpn. J. Physiol.* **2001**, *51*, 127-132.

(71) Zayat, L.; Filevich, O.; Baraldo, L. M.; Etchenique, R. *Philos. Trans. A Math Phys. Eng. Sci.* **2013**, *371*, 20120330.

(72) Dwyer, F.; Goodwin, H.; Gyarfas, E. *Aust. J. Chem.* **1963**, *16*, 544-548.

(73) Pinnick, D. V.; Durham, B. *Inorg. Chem.* **1984**, *23*, 1440-1445.

(74) McCusker, J. K. *Acc. Chem. Res.* **2003**, *36*, 876-887.

(75) Garner, R. N.; Joyce, L. E.; Turro, C. *Inorg. Chem.* **2011**, *50*, 4384-4391.

(76) Zayat, L.; Calero, C.; Alborés, P.; Baraldo, L.; Etchenique, R. *J. Am. Chem. Soc.* **2003**, *125*, 882-883.

(77) Muller, M.; Dierkes, P. W.; Schlue, W. R. *Brain Res.* **1999**, *826*, 63-73.

(78) Filevich, O.; Salierno, M.; Etchenique, R. *J. Inorg. Biochem.* **2010**, *104*, 1248-1251.

(79) Filevich, O.; Etchenique, R. *Photochem. Photobiol. Sci.* **2013**, *12*, 1565-1570.

(80) Campagna, S.; Puntoriero, F.; Nastasi, F.; Bergamini, G.; Balzani, V. In *Photochemistry and Photophysics of Coordination Compounds I*; Balzani, V., Campagna, S., Eds.; Springer Berlin Heidelberg: 2007; Vol. 280, p 117-214.

(81) Salierno, M.; Marceca, E.; Peterka, D. S.; Yuste, R.; Etchenique, R. *J. Inorg. Biochem.* **2010**, *104*, 418-422.

(82) Araya, R.; Andino-Pavlovsky, V.; Yuste, R.; Etchenique, R. *ACS Chem. Neurosci.* **2013**, *4*, 1163-1167.

(83) Meng, F.; Zhong, Z. *J. Phys. Chem. Lett.* **2011**, *2*, 1533-1539.

(84) Discher, B. M.; Won, Y.-Y.; Ege, D. S.; Lee, J. C.-M.; Bates, F. S.; Discher, D. E.; Hammer, D. A. *Science* **1999**, *284*, 1143-1146.

(85) Discher, D. E.; Eisenberg, A. *Science* **2002**, *297*, 967-973.

(86) Photos, P. J.; Bacakova, L.; Discher, B.; Bates, F. S.; Discher, D. E. *J. Controlled Release* **2003**, *90*, 323-334.

(87) Christian, D. A.; Cai, S.; Bowen, D. M.; Kim, Y.; Pajerowski, J. D.; Discher, D. E. *Eur. J. Pharm. Biopharm.* **2009**, *71*, 463-474.

(88) Immordino, M. L.; Dosio, F.; Cattel, L. *Int. J. Nanomed.* **2006**, *1*, 297-315.

(89) Lee, J. S.; Feijen, J. *J. Controlled Release* **2012**, *161*, 473-483.

(90) De Oliveira, H.; Thevenot, J.; Lecommandoux, S. *Wiley Interdiscip. Rev.: Nanomed. Nanobiotechnol.* **2012**, *4*, 525-546.

(91) Tong, X.; Wang, G.; Soldera, A.; Zhao, Y. *J. Phys. Chem. B* **2005**, *109*, 20281-20287.

(92) Robbins, G. P.; Jimbo, M.; Swift, J.; Therien, M. J.; Hammer, D. A.; Dmochowski, I. J. *J. Am. Chem. Soc.* **2009**, *131*, 3872-3874.

(93) Kamat, N. P.; Robbins, G. P.; Rawson, J.; Therien, M. J.; Dmochowski, I. J.; Hammer, D. A. *Adv. Funct. Mater.* **2010**, *20*, 2588-2596.

(94) Kamat, N. P.; Liao, Z.; Moses, L. E.; Rawson, J.; Therien, M. J.; Dmochowski, I. J.; Hammer, D. A. *Proc. Natl. Acad. Sci. U. S. A.* **2011**.

(95) Shang, L.; Nienhaus, K.; Nienhaus, G. *J Nanobiotechnology* **2014**, *12*, 5.

(96) Cabane, E.; Malinova, V.; Meier, W. *Macromol. Chem. Phys.* **2010**, *211*, 1847-1856.

(97) Cabane, E.; Malinova, V.; Menon, S.; Palivan, C. G.; Meier, W. *Soft Matter* **2011**, *7*, 9167-9176.

Chapter 2

Caged oligonucleotides for bidirectional photomodulation of *let-7* in zebrafish embryos

This chapter was adapted from J.C. Griepenburg et. al. *Bioorg. Med. Chem.* 2013, 21, 6198-6204.

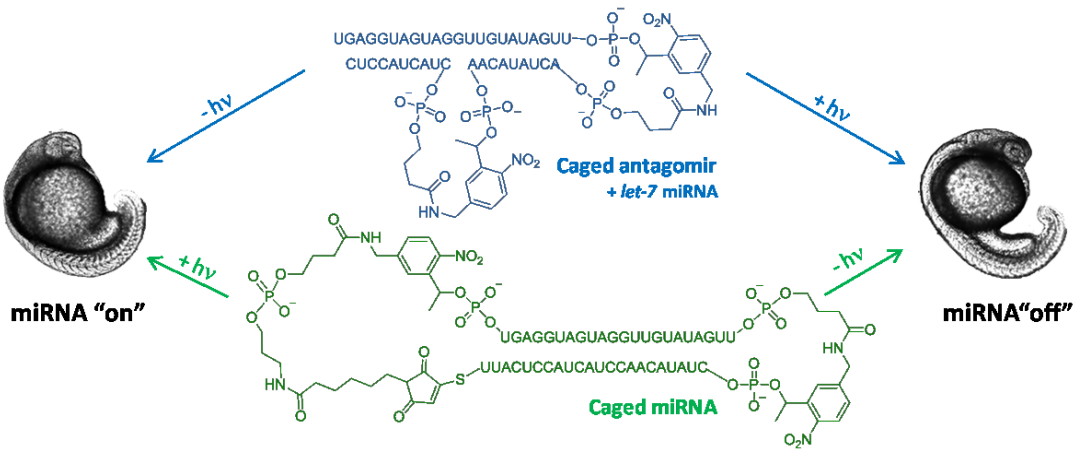

I. Introduction

MicroRNA (miRNA) is a large class of non-coding RNA that interferes with post-transcriptional gene expression through binding to the 3′ UTR of mRNA. Since the discovery of the first miRNA in 1993, *lin-4*, it has been found that miRNAs are abundant short RNAs that have important roles in normal developmental and cellular processes, as well as in human disease.[1,2]

Unlike short interfering RNA (siRNA), a single miRNA can interfere with multiple gene targets, as binding does not require perfect complementarity except in the 5′ seed region.[3,4] This makes elucidation of miRNA function particularly challenging as a single miRNA can have multiple roles that vary with cellular location and timing.[5] Loss-of-function miRNA studies are useful in determining miRNA pathways,[6] but fall short in identifying multiple miRNA functions with spatial and temporal resolution.

Loss-of-function studies of miRNA are most commonly performed using anti-miRNA oligonucleotides, also known as antagomirs.[7] These oligonucleotides are perfectly complementary to the biologically active sequence of the miRNA and sterically block function by outcompeting the target mRNA. Various oligonucleotide backbone and ribose modifications have been previously studied to improve the efficacy of antagomirs, such as phosphorothioation, 2′-F RNA, 2′-OMe RNA, locked nucleic acid (LNA), as well as morpholinos which are commonly used in antisense applications.[4] Reverse complementary 2′-OMe RNA can block miRNA function in *C. elegans*, based on

nuclease resistance and increased binding affinity as shown by melting temperature (T_m) studies.[6,8]

The complexity of gene expression patterns established in metazoan early development has motivated the creation of biochemical tools for controlling genes with higher spatial and temporal resolution.[9-12] Light-activated approaches show considerable promise as near-UV/Vis/near-IR light of desired wavelength can be applied dose-dependently and in a spatially and temporally controlled manner. In recent years, there have been advances in caging siRNA, allowing for spatial and temporal control of the RNA interference (RNAi) pathway. In 2005 the Friedman lab first reported caged siRNA by labeling the phosphate backbone of a siRNA duplex with 1-(4,5-dimethoxy-2-nitrophenyl)ethyl moieties, which blocked the siRNA-RISC interaction before photolysis.[13] Additional work by the Friedman lab blocked siRNA activity with a larger photocleavable cyclo-dodecyl (dimethoxy-2-nitrophenyl)ethyl moiety.[14] The addition of steric bulk to the terminal phosphates prevents Dicer and nucleases that could remove the caging group, from interacting with the siRNA. Most recently, Kala et. al. presented a method of photoregulating siRNA with a tetra-DMNPE–modified duplex RNA, where the terminal phosphates are caged with regiospecific DMNPE.[15] The terminal DMNPE groups effectively cage native siRNA until irradiated with 365 nm light.

While these and other[16,17] advances have been made towards spatiotemporal control of the RNAi pathway, there has been much less reported for the biochemical modulation of miRNA. Recently, Zheng et al. reported a novel photoactivatable

antagomir for controlling miRNA in *C. elegans*.[18] In this work, a caged hairpin-like structure was created by attaching a complementary blocking strand to the antagomir via a coumarin moiety. After irradiation, dissociation of the antagomir became more favorable, allowing binding to a miRNA target.[18] Additionally, Connelly et al. reported a method of photomodulating miRNA in cells by attaching caging groups on specific bases of the *miR-122* and *miR-21* antagomirs.[19] Here, we expand upon the caged hairpin antagomir. Moreover, we provide the first example of a caged miRNA, which makes it possible to "turn on" exogenously supplied miRNA via photoactivation.

Let-7, the miRNA of interest in this study, was discovered in 2000 in *C. elegans* by Reinhart et al. and was shown to play an important role in developmental timing.[20] Interestingly, this particular miRNA is evolutionarily conserved across humans, flies, mice, and zebrafish.[21] *Let-7* miRNA was chosen for the current investigation due to the developmental arrest caused by overexpression in *Danio rerio* (zebrafish) embryos, resulting in a readily observable phenotype.[5] This phenotype is characterized by reduced head and eye formation, shortened tail, and limited yolk sack extension.[5] *Let-7* miRNA is not endogenously expressed in zebrafish embryos until 48 hours post fertilization (hpf), but an early *let-7* expression phenotype can be induced by injecting the *let-7* miRNA at the one-cell stage. This phenotype is clearly visible at 24 hpf.[5] Representative examples of zebrafish embryos showing the *let-7* early induction phenotype are shown in Figure 2-1. This provides a miRNA-vertebrate model system to photoregulate miRNA in both directions--from "off to on" and "on to off".

Novel oligonucleotide constructs were developed for regulating miRNA in zebrafish embryos: two caged hairpin antagomirs (CHANT1, CHANT2) for blocking miRNA function with 365 nm light, as well as a caged circular miRNA (CIRC*let7*) for introducing exogenous miRNA into a system with 365 nm light. The design of CHANT1 was guided by our lab's experience in developing caged hairpins with a single photocleavable linker for photoactivating antisense oligonucleotides in zebrafish embryos.[22] This is similar to the caged hairpin antagomir recently published by Zheng et al.[18] In CHANT2, we expand upon this design by incorporating a longer blocking sense strand and second photocleavable linker. Finally, the circular miRNA expands on our previous circular design involving the 10-23 DNAzyme,[23] and also draws inspiration from several notable circular caged oligonucleotide constructs that have recently been published.[24-26]

II. Experimental procedures

A. Synthesis, purification, and characterization of light-activated miRNA antagomirs: CHANT1 and CHANT2

CHANT1 and CHANT2 were synthesized on a 1 μmol scale using published methods for oligonucleotide synthesis on solid support using an ABI 394 DNA synthesizer.[27,28] CHANT1 and CHANT2 were cleaved from solid support using concentrated ammonium hydroxide for 16 h, and HPLC purified (Figure 2-2). A reverse-

phase C18 semi-preparatory column was used on an Agilent 1100 HPLC system. A gradient of 10% - 80% acetonitrile in 0.05 M triethylammonium acetate (TEAA) was used for purification of all oligonucleotides containing a dimethoxytrityl (DMT) protecting group (Table 2-1). The DMT protecting group was removed using 80% glacial acetic acid for 20 min at rt. A NAP-5 column was used for buffer exchange after purification and deprotection. After HPLC purification, approximately 100 nmol of pure material was isolated.

Table 2-1. Gradient for HPLC purification of CHANT1 or CHANT2 after cleavage from solid support.

A gradient of 0.05 M triethylammonium acetate in H2O was used with a Zorbax reverse-phase C18 column. The column was heated to 40 °C during purification.

Time (min)	% Acetonitrile	% 0.05 M TEAA
0.0	90	10
40.0	40	60
50.0	20	80

B. Synthesis and purification of CIRC*let7*

CIRC*let7* was synthesized on a 1 μmol scale using published methods for oligonucleotide synthesis on solid support using an ABI 394 DNA synthesizer.[29] A FMOC-protected amino solid support was used on the 3′ end and a disulfide

phosphoramidite was incorporated at the 5′ end. The construct was cleaved from solid support using concentrated ammonium hydroxide for 16 h, and HPLC purified (Figure 2-2A). A reverse-phase C18 column was used on an Agilent 1100 HPLC system. A gradient of 10% - 80% acetonitrile in 0.05 M triethylammonium acetate (TEAA) was used for purification of all oligonucleotides containing a dimethoxytrityl (DMT) protecting group (Table 2-2B). The DMT protecting group was removed using 80% glacial acetic acid for 20 min at rt. A NAP-5 column was used for buffer exchange and desalting after purification and deprotection. After HPLC purification, approximately 30 nmol of pure material was attained.

The 3′ amine was reacted with an excess of sulfo-EMCS linker. A 0.4 mg/mL linker solution was prepared in 0.1 M PBS buffer, pH 7.2. The reaction was allowed to proceed for 30 min at 37 °C and quenched by removing excess sulfo-EMCS with a NAP-5 column. The 5′ disulfide was then reduced with TCEP at 37 °C, and the circularization reaction with 5′ thiol was allowed to proceed for 24 h. Circularization was confirmed by visualizing bands by gel electrophoresis. Circularization yield was determined by band quantification using ImageQuant TL 7.0 Image Analysis Software with the rubber band background subtraction method. Circular product was purified from linear starting material using anion exchange HPLC (Figure 2-3B). A Dionex DNAPac PA100 anion exchange column was used with a gradient of $NaClO_4$ in the presence of Tris-Cl pH 8.0 to separate linear starting material from circularized product (Table 2-2B).

Table 2-2. Gradients for HPLC purification of CIRC*let7* A) after solid-phase synthesis and B) after circularization.

A) Zorbax C18 column heated to 40 °C during purification B) DNAPac PA100 column heated to 60 °C during purification.

A)

Time (min)	% Acetonitrile	% 0.05 M TEAA
0.0	90	10
40.0	40	60
50.0	20	80

B)

Time (min)	% H_2O	% 0.25 M Tris-Cl pH 8	% 0.375 M $NaClO_4$
0.0	88	10	2
0.1	58	10	32
26.1	32	10	58
26.5	0	0	100
34.5	0	0	100
35.0	88	10	2
50.0	88	10	2

C. Characterization

Melting temperature analysis was performed on a Beckman Coulter DU800 spectrophotometer with a Peltier temperature controller and T_m analysis software. A solution of 1 μM oligonucleotide in 50 mM NaCl in deionized H_2O was used for all

melting temperature experiments. Samples were irradiated using a Spectroline TR-365R transilluminator delivering 9 mW/cm^2 centered at 365 nm for 10 min. Melting temperatures were analyzed by varying the temperature between 15 °C and 90 °C at a rate of 1 °C per min, in both forward and reverse directions.

Gel electrophoresis was performed using a 20% polyacrylamide gel containing 7 M urea. Gels were run at 300 V for 45 min and stained with ethidium bromide. Gels were imaged with a GE Typhoon FLA 7000 imager. Masses were confirmed by the Wistar Proteomics Facility using an Applied Biosystems Voyager 6030 with 3-hydroxypicolinic acid (3-HPA) as matrix (Table 2-3, Figure 2-4).

Table 2-3. Masses determined for CHANT1 and CHANT2 by MALDI-TOF MS.

	Expected Mass (m/z)	**MALDI Mass (m/z)**
CHANT1	11,683	11,466
CHANT2	14,336	14,498

D. *In vivo* studies

Zebrafish embryos were obtained from CDB Zebrafish Core Facility at the University of Pennsylvania. Both Tu and TLF wildtype embryos were used for these studies. Zebrafish embryo injection solutions were prepared to contain a final concentration of 0.1 M KCl and 0.25% phenol red dye. All injections were performed at the one-cell stage and injected into the cell compartment only. A Harvard Apparatus PLI-

100 pico-injector was used to inject controlled volumes. Injection volume was calibrated to dispense 8 - 10 nL per embryo. Zebrafish embryos were incubated at 28 °C in E3 zebrafish medium.[30] All embryos were incubated in the dark, except for irradiated samples which were exposed to near-UV light for the stated time and returned to the dark incubator. Embryo micrographs were collected at 24 hpf with an Olympus FV1000 laser scanning confocal microscope using transmitted light imaging. A 10x air objective was used for single embryo imaging.

E. Materials

2′-OMe RNA phosphoramidites for solid-phase oligonucleotide synthesis and all modified phosphoramidites, including CPG solid supports, were purchased from Glen Research (Sterling, VA). Product numbers for photocleavable spacer phosphoramidite, amino modifier CPG, and thiol modifier phosphoramidite are 10-4913-90, 20-2957-01, 10-1926-90, respectively. N-Ɛ-Maleimidocaproyl-oxysulfosuccinimide ester (Sulfo-EMCS) linker was purchased from Thermo Scientific (Pierce Protein Biology Products). NAP-5/10 desalting columns were purchased from GE Healthcare. *Let-7* miRNA (5′-UGAGGUAGUAGGUUGUAUAGUU-3′) was ordered from Integrated DNA Technologies (IDT).

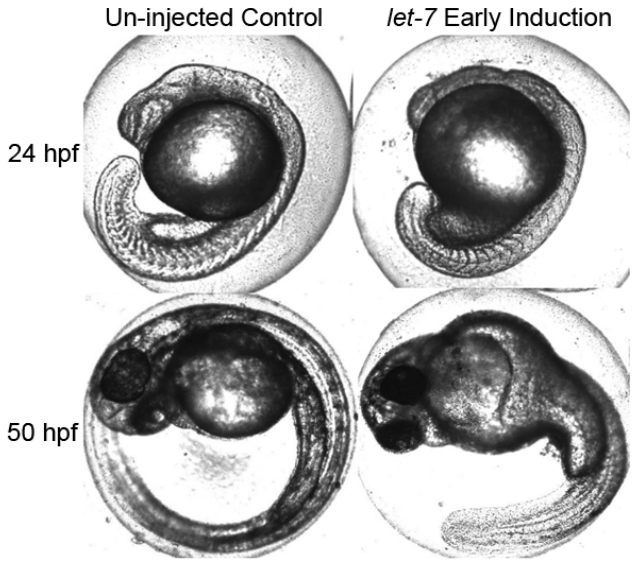

Figure 2-1. *let-7* early induction phenotype.

Zebrafish embryos injected at the 1-cell stage with 10 μM *let-7* miRNA show the *let-7* early induction phenotype when imaged at 24 and 50 hpf (right images), compared to un-injected wildtype (Tu x Tu) embryos (left images). The early induction *let-7* miRNA phenotype is characterized by decreased head formation, shortened tail, and yolk that fails to extend along the tail.

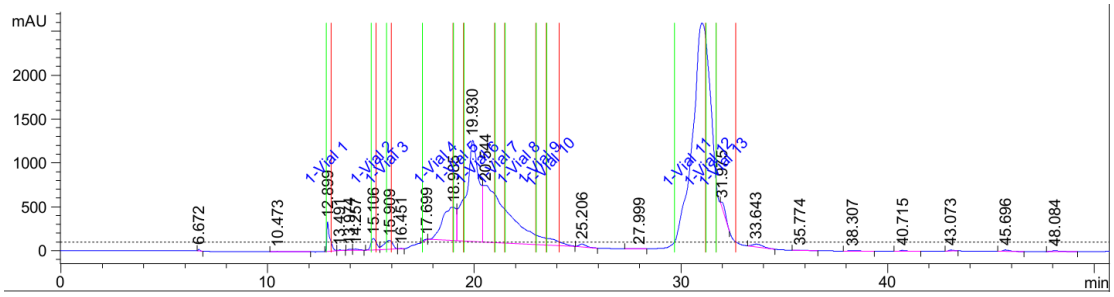

Figure 2-2. HPLC trace for CHANT1.

Purification of CHANT1 after cleavage from solid support was performed using a Zorbax C18 column with a gradient of 0.05 M triethylammonium acetate in H_2O. Column was heated to 40 °C during purification. Product eluted at 30 - 31 min with gradient in Table 2-1.

A

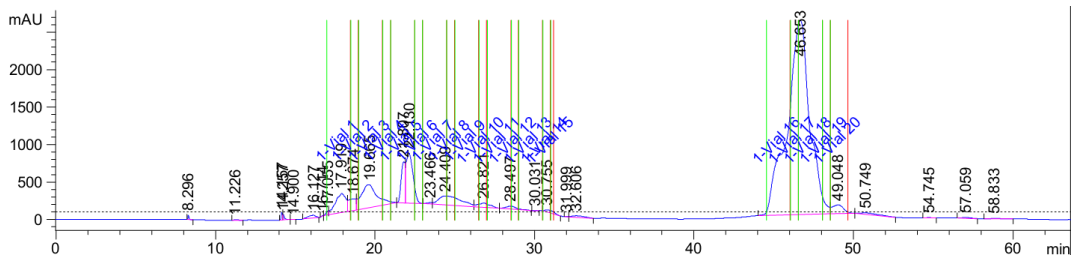

B

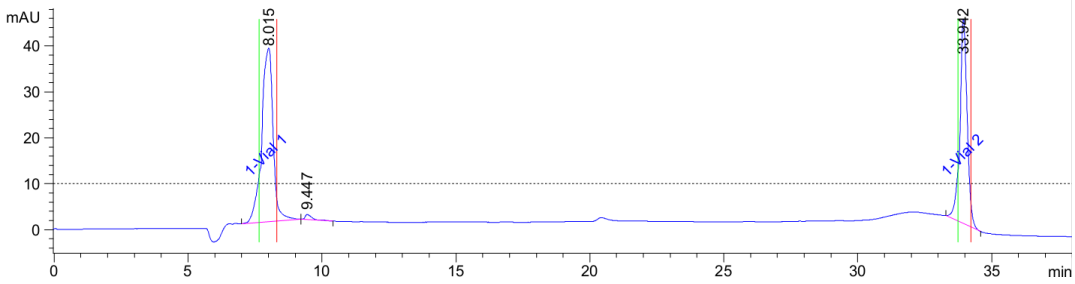

Figure 2-3. HPLC traces for purification of CIRC*let7*.

A) Purification of linear oligonucleotide after cleavage from solid support was performed using a Zorbax C18 column with a gradient of 0.05 M triethylammonium acetate in H_2O. Column was heated to 40 °C during purification. Retention time of product was 46 min. B) Purification of circular product after circularization procedure using a DNAPac PA100 column with a gradient of 0.25 M Tris-Cl pH 8 and 0.375 M $NaClO_4$ in H_2O (adapted from manufacturer protocol). Column was heated to 60 °C during purification. Retention time of CIRC*let7* was 34 min.

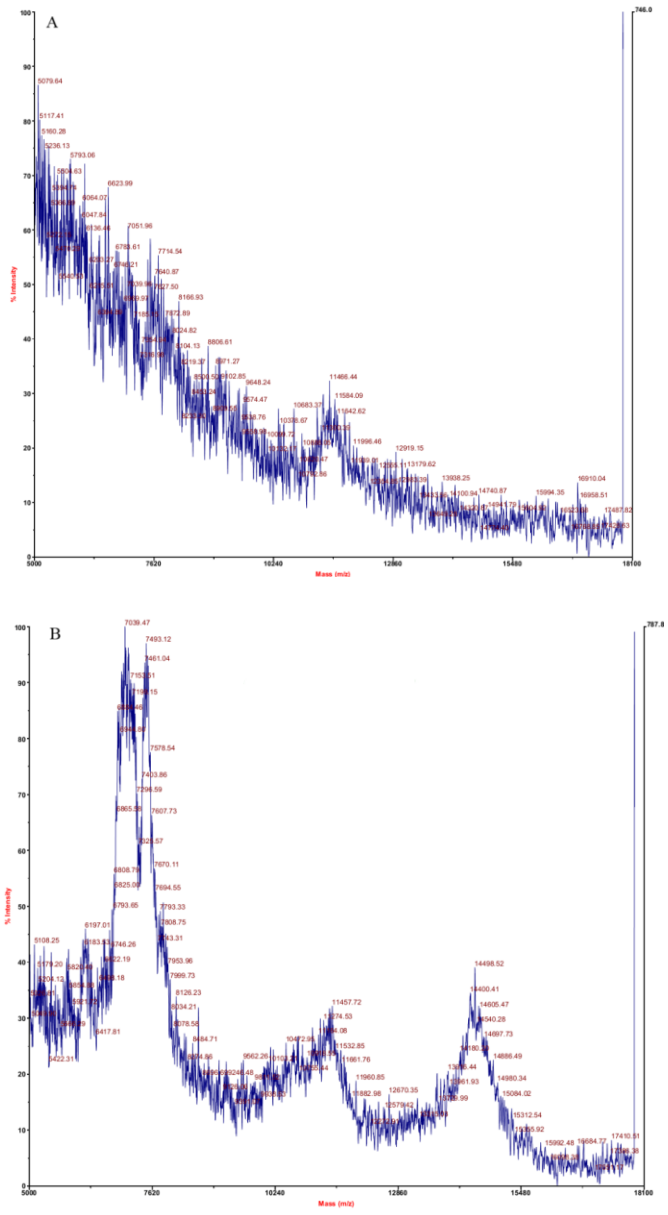

Figure 2-4. Masses determined for A) CHANT1 and B) CHANT2 by MALDI-TOF MS.

MALDI-MS was performed by the Wistar Proteomics Facility at the University of Pennsylvania. All masses were attained in linear negative mode, using 3-hydroxypicolinic acid (3-HPA) matrix.

III. Results and discussion

A. Photoactivatible miRNA antagomir: CHANT1

A caged hairpin antagomir (CHANT1) was designed and synthesized to "turn off" *let-7* miRNA with a low dose of 365 nm irradiation. This antagomir consisted of a 22-mer oligonucleotide synthesized with all 2′-OMe RNA bases (Figure 2-5). The function of this antagomir was inhibited by a shorter 12-mer 2′-OMe RNA blocking strand. The antagomir and blocking strand were covalently attached by a nitrobenzyl photocleavable linker, PL (shown in red). Prior to photolysis, PL stabilized the hairpin hybrid form, thereby blocking the function of the antagomir. Upon near-UV irradiation, PL was cleaved, resulting in a destabilized hybrid. The photoactivated 22-mer 2′-OMe RNA antagomir can readily hybridize to the complementary miRNA and sterically block its function.

In designing CHANT1, a balance was struck between antagomir blocking efficiency and restoration of antagomir function post-irradiation. In principle, all antagomir nucleotides can be sterically blocked with a 22-mer blocking sequence; however, this would disfavor dissociation post-irradiation. For this particular construct, a 12-mer blocking strand was chosen to block the antagomir at the 5' seed region, as this 6-8 nucleotide sequence has been shown to be important in miRNA-mRNA target recognition.[31,32] Additionally, terminating the blocking sequence with a guanine or cytosine base should result in a more stable hybrid due to the increase in hydrogen

bonding. For this reason, the placement and length of the blocking strand for this particular sequence was chosen to be a 12-mer as shown in Figure 2-5.

CHANT1 was synthesized by solid-phase synthesis, isolated by HPLC purification (Figure 2-2, Table 2-1)), and confirmed by MALDI-TOF MS to have the correct mass (Figure 2-4, Table 2-3). Melting temperature analysis has proved to be a useful tool to determine nearly the optimal length of the blocking strand. Melting temperature analysis showed a CHANT1 melting temperature of ≥ 85 °C, indicating favorable duplex stability. The T_m dropped to 64 °C post-photolysis, decreasing the melting temperature (ΔT_m) by at least 21 °C (Figure 2-6). This ΔT_m indicates significant photomodulation of duplex stability and is comparable to many caged hairpins synthesized in our laboratory.[33-35] However, the post-photolysis T_m of 64 °C suggests that a significant amount of antagomir remains bound to the blocking strand (and therefore inactive), even after uncaging.

To confirm the efficacy of the exogenous *let-7* miRNA *in vivo*, a 10 μM solution was injected into zebrafish embryos at the one-cell stage (n = 35). Injection resulted in the *let-7* miRNA early induction phenotype in 92% of embryos (Figure 2-1). *In vivo* studies with CHANT1 were subsequently performed by co-injecting a 10 μM solution of *let-7* miRNA, together with varying concentrations (40 - 100 μM) of CHANT1 into embryos at the one cell stage. CHANT1 at 50 μM exhibited high activity with minimal toxicity. Thus, a 10 μM solution of *let-7* miRNA and 50 μM CHANT1 was subsequently injected into all zebrafish embryos at the one-cell stage. Half of the injected embryos

were allowed to incubate at 28 °C in the dark, while the other half were irradiated at 1 hpf. A near-UV transilluminator was used to irradiate the embryos for 10 min in E3 zebrafish media. The embryos were incubated for 24 h at 28 °C, and then imaged to determine phenotypic response. Of the embryos that were irradiated with 365 nm light (n = 21), the majority (86%) developed normally, indicating that the caged antagomir was photoactivated and able to block *let-7* miRNA function (Figure 2-7). In the non-irradiated embryo group (n = 15), the majority (80%) developed with the *let-7* miRNA early induction phenotype, as expected. However, a significant minority (20%) of the embryos developed normally (Figure 2-10), indicating incomplete caging of CHANT1. Although this caged hairpin exhibited a very high T_m, only 12 of the 22 antagomir nucleotides were blocked from *let-7* miRNA binding.

B. Photoactivatible miRNA antagomir: CHANT2

A second caged hairpin antagomir, CHANT2 (Figure 2-5B), was developed with the goal of minimizing background miRNA binding pre-photolysis, while maximizing miRNA binding post-photolysis. To achieve these aims, we reasoned that the caged hairpin must form a longer, stable duplex structure prior to irradiation, and become less thermodynamically stable afterwards. In particular, the high melting temperature of CHANT1 post-photolysis indicated a route to further optimization.

To minimize caged antagomir background activity, the number of complementary bases in the blocking sequence was increased such that fewer antagomir bases were available to bind to the miRNA. By adding an additional photocleavable moiety in the

blocking strand, it was possible to incorporate more bases within the blocking strand, without sacrificing antagomir activity after irradiation. Prior to *in vivo* studies, one goal in design optimization was to increase ΔT_m, pre- vs. post-photolysis.

The same 22-mer antagomir complementary to *let-7* miRNA was covalently attached via a PL to a blocking strand comprised of a 9-mer and 10-mer linked by an additional PL (Figure 2-5B). This PL blocking strand design was guided by our previously published RNA "bandage" which used two shorter sequences linked by a PL to achieve mRNA blocking pre-photolysis and dissociation post-photolysis.[36] Consistent with successful RNA bandage designs,[36] a one nucleotide gap was introduced at the position of the PL. Finally, because terminating the blocking sequence with a guanine or cytosine base should result in a more stable duplex, the blocking strand was extended by one base on the 3′ end to a 10-mer to facilitate G/C base-pair termination.

CHANT2 was synthesized on solid support, purified by HPLC (Figure 2-2, Table 2-1) and the mass was confirmed by MALDI-TOF MS (Table 2-3, Figure 2-4). The ΔT_m for CHANT2 was measured to be -38 °C: $T_{m\ (-UV)}$ = 71 °C, $T_{m\ (+UV)}$ = 33 °C (Figure 2-8). Significantly, $T_{m\ (+UV)}$ was much closer to rt than observed for CHANT1, which should improve the miRNA-binding activity of the uncaged antagomir. Moreover, relative to CHANT1 with a single 12-mer blocking strand, CHANT2 exhibited a significantly greater difference in thermal stability pre- vs. post-photolysis, $\Delta\Delta T_m$ = 17 °C. Interestingly, $T_{m\ (-UV)}$ was significantly lower for CHANT2 than CHANT1, which indicates that the 9-mer-PL-10-mer blocking strand did not behave as a contiguous 19-

mer. This is likely due to the intervening PL, and also the one nucleotide gap included in the 9-mer-PL-10-mer design. This is further corroborated by the appearance of the broad T_m curve. Upon photolysis, two short oligonucleotides of different lengths will dissociate at different temperatures, causing the melting curve to broaden.

Based on T_m alone, it would appear as though CHANT1 would be more stable prior to photolysis due to a higher melting temperature. However, when the structure of CHANT2 is taken into account and analyzed together with *in vivo* data, it is clear that thermal stability alone is not a clear predictor of blocking efficiency. In cases where the T_m is significantly above incubation temperature, it is expected that the hairpin will remain annealed. A more important factor becomes the antagomir bases that are sterically blocked when the caged hairpin is fully annealed, and this is why the addition of the second PL becomes so critical for *in vivo* efficiency. Preliminary *in vivo* studies were performed by co-injecting a 10 μM solution of *let-7* miRNA with varying concentrations (30 – 100 μM) of CHANT2 into embryos at the 1-cell stage. CHANT2 at 50 μM exhibited high activity with minimal toxicity. Thus, a 10 μM solution of *let-7* miRNA and 50 μM CHANT2 was subsequently injected into all zebrafish embryos at the one-cell stage. Half of the injected embryos were incubated at 28 °C in the dark, while the other half were irradiated at 1 hpf for 10 min with the near-UV transilluminator. The embryos were incubated for 24 h in the dark at 28 °C and then imaged to determine phenotypic response (Figure 2-9). The embryos that were irradiated (n = 40) developed normally which clearly showed that the uncaged antagomir was active. Photoactivated CHANT2

rescued the normal wildtype phenotype for nearly 90% of zebrafish embryos, vs. 80% for CHANT1 embryos (Figure 2-10). A marked improvement was also seen in antagomir caging in the non-irradiated embryos (n = 45), with just 2% background activity for CHANT2 compared to 20% for CHANT1 (Figure 2-10). This 2% background can be attributed to injection error, which can range from 0 - 10% of embryos. This construct was also tested at lower concentrations (30 - 50 μM) and it was demonstrated that *in vivo* efficiency is dependent on concentration. This concentration dependence is expected, as the amount of free antagomir post-photolysis directly depends on the incubation temperature (28°C) which happens to be below the T_m. The concentration reported with maximum efficiency is far below 100 μM, the concentration where significant toxicity was observed.

The significant decrease in CHANT2 background activity as compared to CHANT1 highlights that the 9-mer-PL-10-mer blocking strand caged the antagomir more effectively than the original 12-mer, despite the lower thermal stability of CHANT2 (T_m = 72 °C) relative to CHANT1 ($T_m \geq 85$ °C) (Figure 2-6, 2-8). The melting temperature for CHANT1 is reported as ≥ 85 °C as the exact temperature cannot be determined since a full transition cannot be observed at such a high T_m. The data indicate that CHANT2 is nearly optimized for photomodulating the *let-7* antagomir in the current experimental paradigm, where miRNA is co-injected in zebrafish embryos.

With the creation of CHANT1 and CHANT2 and the two previously published caged antagomirs,[19,37] a new class of tools for downregulating miRNA with light is

emerging. Connelly et al. presented an elegant method of caging antagomirs miR-122 and miR-21 with minimal background activity and showed efficient antagomir restoration post-photolysis, however, this involved the use of custom caged bases. Zheng et al. presented the first example of *in vivo* miRNA photomodulation by using a caged hairpin antagomir. To achieve very efficient caging and uncaging, it was necessary to design and test a large number of caged antagomirs. Our CHANT2 design minimizes the need for optimization, as the second PL allows a much larger portion of the antagomir to be blocked without sacrificing uncaging efficiency. This will facilitate the targeting of multiple miRNAs without optimization necessary for each sequence. Additionally, the commercial availability of the 2′-OMe RNA phosphoramidites and PL used in CHANT2 make it readily accessible to biological researchers.

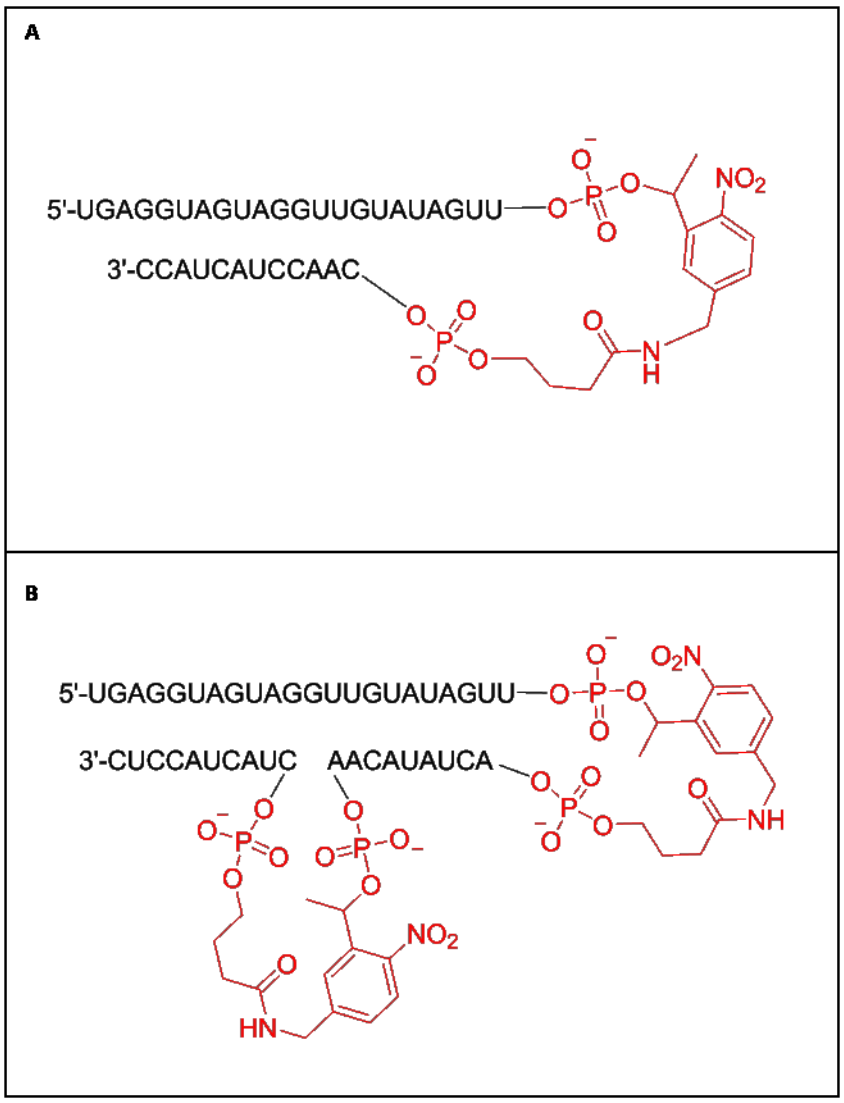

Figure 2-5. Structures of caged hairpin antagomirs CHANT1 and CHANT2.

A) CHANT1: A 22-mer miRNA antagomir targeting *let-7* miRNA was covalently attached to a complementary 12-mer blocking sequence via a nitrobenzyl photocleavable linker, PL (in red). Upon photolysis, the 12-mer more readily dissociated, restoring antagomir function. B) CHANT2: A 22-mer miRNA antagomir targeting *let-7* miRNA was covalently attached to a 5′-9-mer-PL-10-mer blocking sequence. Upon PL photolysis, antagomir function was restored. All sequences consisted of 2′-OMe RNA bases.

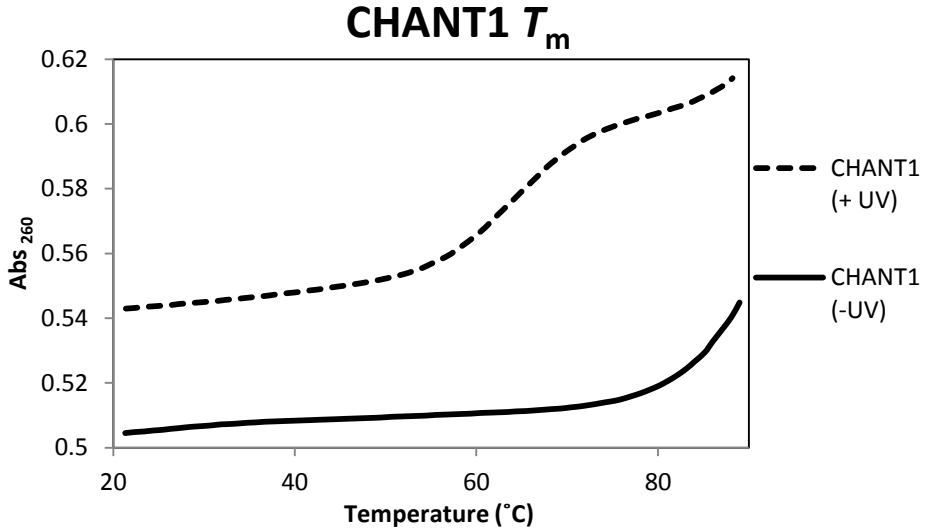

Figure 2-6. Melting temperature data for CHANT 1.

Melting temperature analysis of CHANT1 showing a T_m of $\geq$ 85 °C prior to photolysis, and 64 °C post-photolysis, decreasing the melting temperature (ΔT_m) by at least 21 °C

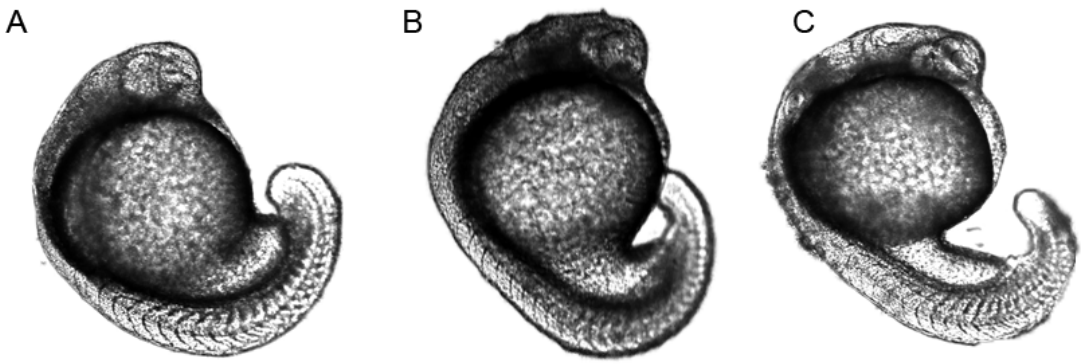

Figure 2-7. CHANT1 *in vivo* experiments.

A) Embryos injected at the 1-cell stage with 10 μM *let-7* miRNA showed *let-7* early induction phenotype. B) Embryos injected with 10 μM *let-7* miRNA + 50 μM CHANT1 showed similar *let-7* early induction phenotype prior to 365 nm irradiation. C) Embryos injected with 10 μM *let-7* miRNA + 50 μM CHANT1 developed normally after 365 nm irradiation for 10 min at 1 hpf. All embryos were imaged at 24 hpf.

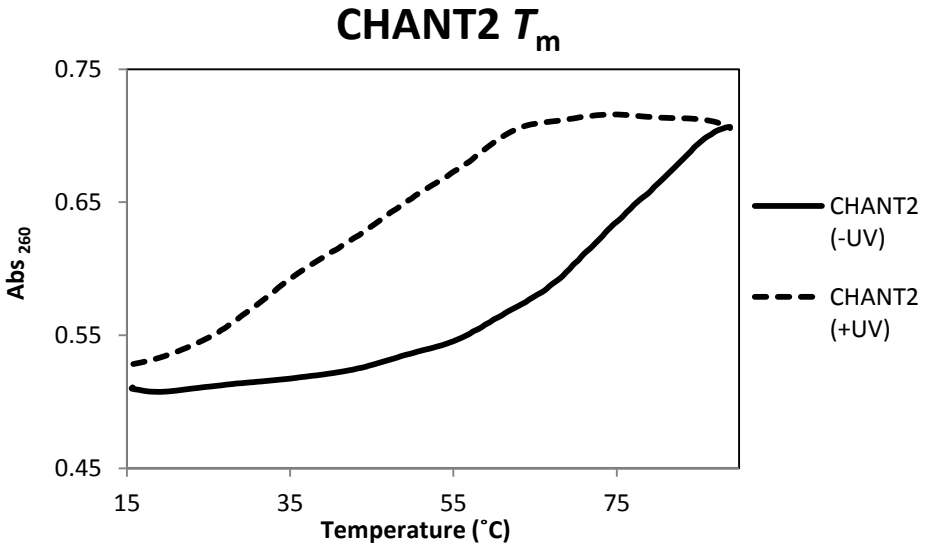

Figure 2-8. Melting temperature data for CHANT2

Melting temperature analysis of CHANT1 showing a T_m of 71 °C prior to photolysis, and 33 °C post-photolysis, decreasing the melting temperature (ΔT_m) by 38 °C.

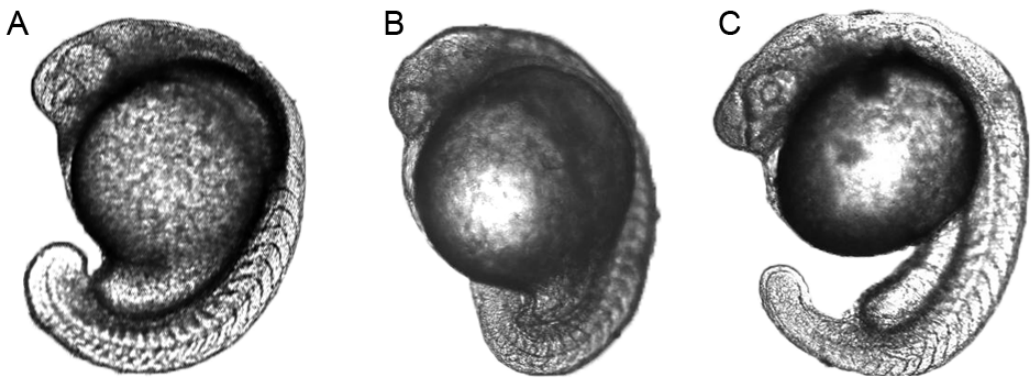

Figure 2-9. CHANT2 *in vivo* experiments.

A) Embryos injected at the 1-cell stage with 10 μM *let-7* miRNA showed *let-7* early induction phenotype. B) Embryos injected with 10 μM *let-7* miRNA + 50 μM CHANT2 antagomir showed *let-7* early induction phenotype prior to 365 nm irradiation. C) Embryos injected with 10 μM *let-7* miRNA + 50 μM CHANT2 developed normally after 365 nm irradiation for 10 min at 1 hpf. All embryos were imaged at 24 hpf.

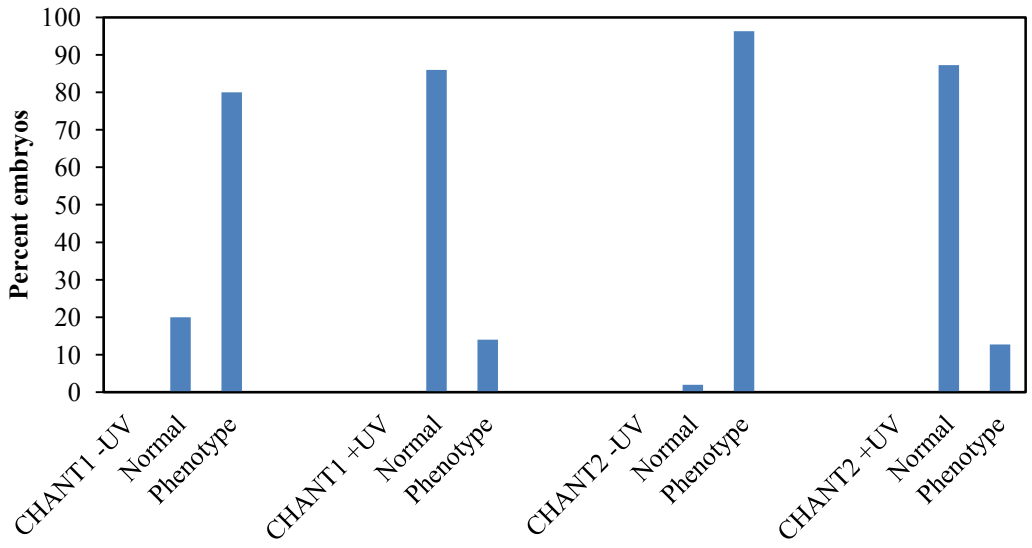

Figure 2-10. CHANT1 vs. CHANT2 *in vivo* efficiency.

C. Caged circular miRNA, CIRC*let7*

In addition to the caged hairpin antagomirs, which provide a method to "turn off" miRNA with light, caged circular *let-7* miRNA (CIRC*let7*) was designed to "turn on" exogenous miRNA with light. The circular design provides a way to introduce miRNA into a biological system and subsequently activate at the desired place and time by irradiating with 365 nm light.

Similar to the caged antagomirs, this caged miRNA uses fully 2′-O-methylated bases to limit degradation that is problematic with unmodified RNA. A complementary 22-mer 2′-OMe RNA miRNA and blocking strand were synthesized containing two PLs, a free amine on the 3′ end, and a disulfide on the 5′ end as shown in Figure 2-11. The 5′ and 3′ ends were linked together in a "circularization reaction" by first reacting the succinimide of a commercially available heterobifunctional linker with the 3′-amine. The 5′-disulfide was then reduced with TCEP, allowing subsequent reaction with the linker maleimide and resulting in a circularized oligonucleotide. Both the linear and circularized oligonucleotides were purified by HPLC (Figure 2-3, Table 2-2). Upon photolysis, the circular miRNA was linearized as shown in Figure 2-11. The phosphate group revealed on the 5' end of the biologically active miRNA allows for processing by the multi-protein RNA-induced silencing complex (RISC). Our lab's previous circular design for caged DNAzymes used Circligase for circularization, which limited the reaction to the picomole scale.[38] By using the heterobifunctional linker, more oligonucleotide can be circularized in a single reaction. Circularization yield, calculated from gel band intensity, was

determined to be 45% when performed on a 1 nmol scale (Figure 2-12). Additionally, a method was developed to purify the circular construct by HPLC without having to do lengthy gel extractions to remove linear starting material. Purity was confirmed by a well-resolved product peak on HPLC which was further analyzed using gel electrophoresis (Figures 2-3B, 2-12).

To test this circular miRNA *in vivo*, a 20 μM solution of CIRC*let7* was injected into zebrafish embryos at the one-cell stage. Half of the injected population was incubated in the dark at 28 °C (n = 18). The other half was irradiated with 365 nm light for 10 min at 1 hpf before incubation (n = 21). The embryos were analyzed and imaged at 24 hpf for phenotypic response. As shown in Figure 2-13, embryos injected with the caged miRNA developed normally, while embryos injected and irradiated developed with the *let-7* miRNA early induction phenotype. These results were seen in 100% of embryos injected, indicating that there was no background activity prior to photolysis and uncaging completely restored miRNA activity. Interestingly, the phenotype induced by the 2′-OMe RNA circular design varies slightly from the phenotype induced by the *let-7* miRNA. A 2′-OMe RNA control miRNA was injected into zebrafish embryos (Figure 2-14) to confirm that this was not a result of the circular construct, but rather a result of an analog used to induce the miRNA phenotype.

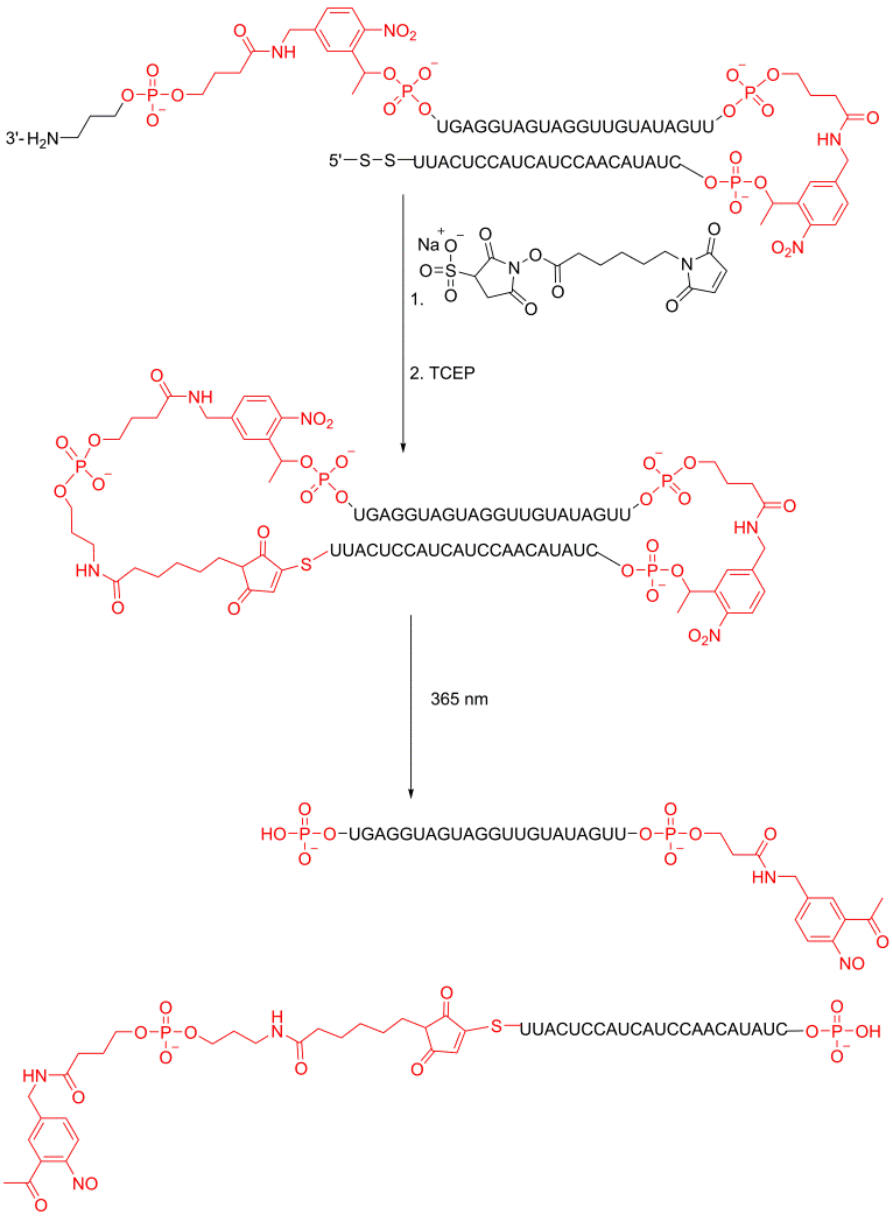

Figure 2-11. Synthesis and photocleavage of circular caged miRNA (CIRC*let7*)

A photocleavable oligonucleotide duplex with 3′-amine and 5′-thiol was circularized with a heterobifunctional crosslinker. The crosslinker was first reacted with the 3′-amine, and circularization proceeded after 5′ disulfide reduction with TCEP. Upon photolysis, the active miRNA strand was released with a 5′-phosphate for processing by RISC.

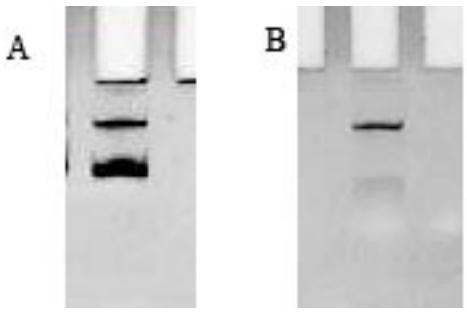

Figure 2-12. Gel electrophoresis of CIRC*let7* crude reaction mixture and CIRClet7 after HPLC purification.

A) Gel after CIRC*let7* circularization procedure used to calculate circularization yield by band intensity. ImageQuant TL 7.0 was used for band quantification using the rubber band subtraction method. Circularization yield was calculated to be 45%. B) Gel after HPLC purification of CIRC*let7* showing only circularized product. All gels were cast using 20% polyacrylamide and 7 M urea and run at 300 V for 45 min. Gels were stained with ethidium bromide.

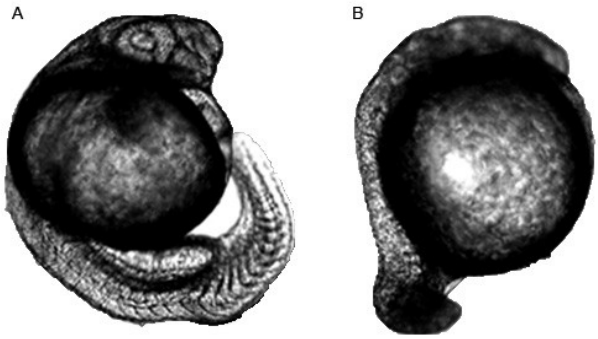

Figure 2-13. CIRC*let7 in vivo* experiments.

A) Zebrafish embryos injected with 20 μM CIRC*let7* and incubated in the dark developed normally. B) Embryos irradiated with 365 nm light developed with the early induction *let-7* miRNA phenotype. All embryos were imaged at 24 hpf.

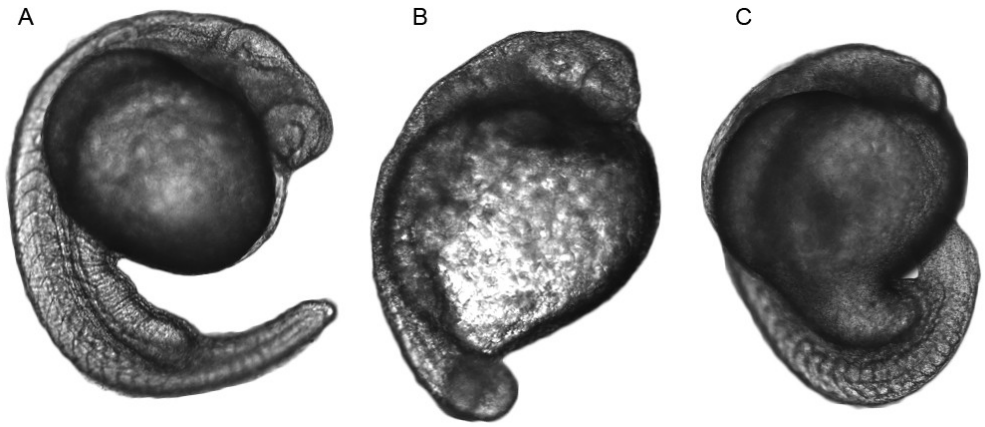

Figure 2-14. Comparison of control, RNA-induced phenotype, and 2′-OMe RNA-induced phenotype.

A) Uninjected control embryo imaged at 24 hpf showing normal development. B) Embryo injected with 15 μM *let-7* 2′-OMe RNA showing a variation of the *let-7* early induction phenotype. C) Embryo injected with 10 μM *let-7* RNA showing a variation of the *let-7* early induction phenotype.

IV. Conclusion

miRNAs are an abundant class of small gene-regulating RNAs, and our understanding of their diverse biological functions is still incomplete. New chemical tools, such as those introduced here, will make it possible to probe how each miRNA regulates a multitude of genes in different locations and at different times *in vivo*.

A set of caged antagomir and caged miRNA constructs have been designed with the ability to regulate miRNA from "on to off" as well as "off to on" with light. These tools were shown to control exogenously supplied miRNA and have the potential to control endogenous miRNA as well. These caged constructs are effective in zebrafish embryos and could readily be optimized for use in other model organisms, such as *Xenopus*[39] and *C. elegans*.[6,8] By using 2′-OMe RNA oligonucleotides, the synthesis of these constructs was greatly simplified, as these analogs can be prepared very successfully on solid support using commercially available phosphoramidites.

Two caged antagomir designs were designed, CHANT1 and CHANT2. With the addition of the second photocleavable linker in CHANT2, more antagomir bases were sterically blocked prior to irradiation without sacrificing antagomir activity post-photolysis. With the addition of a second PL, the blocking strand could be lengthened to diminish background activity seen in the first design. Previously, our lab described several examples of caged antisense hairpins with a similar design to CHANT1 using only one PL.[22,35] Based on this current study, it appears beneficial to incorporate a second PL in many caged hairpin constructs.

To introduce an exogenous miRNA and provide a method for turning a miRNA from "off to on", a circular caged miRNA was designed. CIRC*let7* is the first example of a caged miRNA, and was demonstrated in a zebrafish model system. As not all developmental programs stem from the downregulation of a miRNA, it is also useful to have a tool to probe the effects of miRNA upregulation in different systems. The tools described herein will provide new ways to probe miRNA function, which until now has been difficult to resolve with loss-of-function experiments. A direct follow-up to this work could be the use of light-activatible probes to determine more precisely the genes on which *let-7* miRNA acts in different locations and times in early embryo development, as it is known that there are multiple targets.[5] While these constructs have been developed specifically for *let-7* miRNA in zebrafish, these methods can very easily be applied to additional miRNAs in various biological systems.

V. References

(1) Mishima, Y. *Dev. Growth Differ.* **2011**.

(2) Lee, R. C.; Feinbaum, R. L.; Ambros, V. *Cell* **1993**, *75*, 843-854.

(3) Wu, L.; Belasco, J. G. *Mol. Cell* **2008**, *29*, 1-7.

(4) Esau, C. C. *Methods (San Diego, Calif.)* **2008**, *44*, 55-60.

(5) Kloosterman, W. P.; Wienholds, E.; Ketting, R. F.; Plasterk, R. H. A. *Nucleic Acids Res.* **2004**, *32*, 6284-6291.

(6) Stenvang, J.; Petri, A.; Lindow, M.; Obad, S.; Kauppinen, S. *Silence* **2012**, *3*, 1.

(7) Krutzfeldt, J.; Rajewsky, N.; Braich, R.; Rajeev, K. G.; Tuschl, T.; Manoharan, M.; Stoffel, M. *Nature* **2005**, *438*, 685-689.

(8) Zheng, G.; Ambros, V.; Li, W. H. *Silence* **2010**, *1*, 9.

(9) Tang, X.; Dmochowski, I. J. *Mol. BioSyst.* **2007**, *3*, 100-110.

(10) Deiters, A. *Curr. Opin. Chem. Biol.* **2009**, *13*, 678-686.

(11) Dmochowski, I. J.; Tang, X. *BioTechniques* **2007**, *43*, 161, 163, 165 passim.

(12) Shestopalov, I. A.; Chen, J. K. *Zebrafish* **2010**, *7*, 31-40.

(13) Shah, S.; Rangarajan, S.; Friedman, S. H. *Angew. Chem., Int. Ed.* **2005**, *44*, 1328-1332.

(14) Jain, P. K.; Shah, S.; Friedman, S. H. *J. Am. Chem. Soc.* **2010**, *133*, 440-446.

(15) Kala, A.; Jain, P. K.; Karunakaran, D.; Shah, S.; Friedman, S. H. *Nat. Protocols* **2014**, *9*, 11-20.

(16) Blidner, R. A.; Svoboda, K. R.; Hammer, R. P.; Monroe, W. T. *Mol. BioSyst.* **2008**, *4*, 431-440.

(17) Kala, A.; Friedman, S. H. *Pharm. Res.* **2011**, *28*, 3050-3057.

(18) Zheng, G.; Cochella, L.; Liu, J.; Hobert, O.; Li, W.-h. *ACS Chem. Biol.* **2011**, *6*, 1332-1338.

(19) Connelly, C. M.; Uprety, R.; Hemphill, J.; Deiters, A. *Mol. BioSyst.* **2012**, *8*, 2987-2993.

(20) Reinhart, B. J.; Slack, F. J.; Basson, M.; Pasquinelli, A. E.; Bettinger, J. C.; Rougvie, A. E.; Horvitz, H. R.; Ruvkun, G. *Nature* **2000**, *403*, 901-906.

(21) Ambros, V. *Nat. Methods* **2008**, *14*, 1036-1040.

(22) Tang, X.; Maegawa, S.; Weinberg, E.; Dmochowski, I. *J. Am. Chem. Soc.* **2007**, *129*, 11000-11001.

(23) Richards, J. L.; Seward, G. K.; Wang, Y. H.; Dmochowski, I. J. *ChemBioChem* **2010**, *11*, 320-324.

(24) Wu, L.; Wang, Y.; Wu, J.; Lv, C.; Wang, J.; Tang, X. *Nucleic Acids Res.* **2012**.

(25) Yamazoe, S.; Shestopalov, I. A.; Provost, E.; Leach, S. D.; Chen, J. K. *Angew. Chem., Int. Ed. Engl.* **2012**, *51*, 6908-6911.

(26) Tang, X.; Su, M.; Yu, L.; Lv, C.; Wang, J.; Li, Z. *Nucleic Acids Res.* **2010**, *38*, 3848-3855.

(27) Matteucci, M. D.; Caruthers, M. H. *J. Am. Chem. Soc.* **1981**, *103*, 3185-3191.

(28) Sinha, N. D.; Biernat, J.; McManus, J.; Koster, H. *Nucleic Acids Res.* **1984**, *12*, 4539-4557.

(29) Ellington, A.; Pollard, J. D. In *Current Protocols in Molecular Biology*; John Wiley & Sons, Inc.: 2001.

(30) Westerfield, M. *The Zebrafish Book. A Guide for the Laboratory Use of Zebrafish (Danio rerio)*; 4th Edition ed.; University of Oregon Press, 2000.

(31) Lewis, B. P.; Burge, C. B.; Bartel, D. P. *Cell* **2005**, *120*, 15-20.

(32) Lewis, B. P.; Shih, I. h.; Jones-Rhoades, M. W.; Bartel, D. P.; Burge, C. B. *Cell* **2003**, *115*, 787-798.

(33) Tang, X.; Dmochowski, I. J. *Angew. Chem., Int. Ed.* **2006**, *45*, 3523-3526.

(34) Tang, X.; Maegawa, S.; Weinberg, E. S.; Dmochowski, I. J. *J. Am. Chem. Soc.* **2007**, *129*, 11000-11001.

(35) Tang, X.; Swaminathan, J.; Gewirtz, A. M.; Dmochowski, I. J. *Nucleic Acids Res.* **2008**, *36*, 559-569.

(36) Richards, J. L.; Tang, X.; Turetsky, A.; Dmochowski, I. J. *Bioorg. Med. Chem. Lett.* **2008**, *18*, 6255-6258.

(37) Zheng, G.; Cochella, L.; Liu, J.; Hobert, O.; Li, W. H. *ACS Chem. Biol.* **2011**, *6*, 1332-1338.

(38) Richards, J. L.; Seward, G. K.; Wang, Y.-H.; Dmochowski, I. J. *Chembiochem : a European journal of chemical biology* **2010**, *11*, 320-324.

(39) Schneider, P. N.; Olthoff, J. T.; Matthews, A. J.; Houston, D. W. *Genesis (New York, N.Y. : 2000)* **2011**, *49*, 117-123.

Chapter 3

Ruthenium-caged antisense morpholinos for regulating gene expression in zebrafish embryos

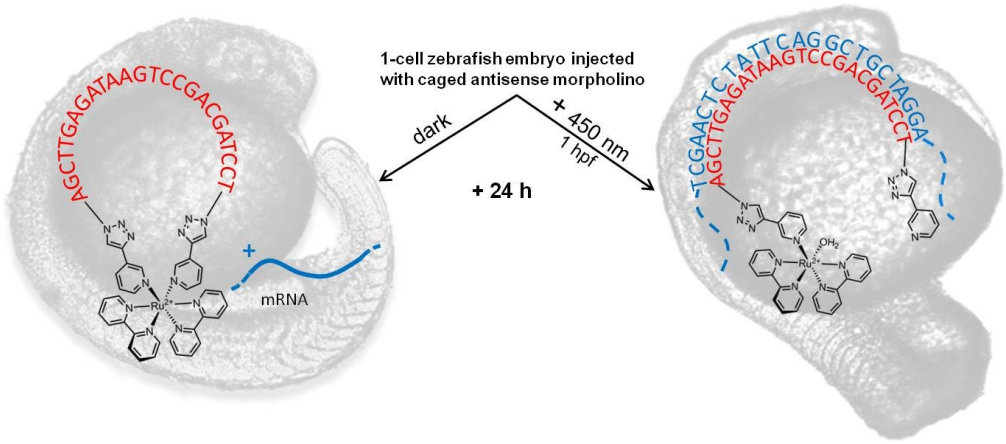

This chapter was adapted from a submitted manuscript:

Julianne C. Griepenburg,[1] Teresa L. Rapp,[1] Patrick J. Carroll, [1] James Eberwine,[2] Ivan J. Dmochowski[1*]

Contribution from Departments of Chemistry[1] and Pharmacology[2],

University of Pennsylvania, 231 South 34th Street, Philadelphia, PA 19104

J. C. Griepenburg performed RuBEP design, characterization, DNA and morpholino work, *in vivo* studies
T. L. Rapp performed RuBEP synthesis, purification, and characterization
P. J. Carroll solved crystal structure.
J. Eberwine and I. J. Dmochowski are funding authors.
[*] Corresponding author

I. Introduction

Photochemical methods for regulating the structure, function, and/or localization of molecular species provide a powerful toolkit for manipulating advanced materials as well as complex biological systems. For example, channelrhodopsin—a single component, light-activated cation channel protein from algae—was co-opted in the development of pioneering optogenetic approaches for manipulating the activity of specific neurons and controlling animal behavior.[1] More generally, "caged" molecules,[2] whose latent biological activity can be revealed with light, have been widely adopted, particularly for the study of amino acids,[3] peptides,[4] neurotransmitters,[5] and metal ions.[6] In each case, photoactivation with high spatiotemporal control can be achieved using a focused laser beam of suitable wavelength. Less investigated are caged oligonucleotides, despite the central roles played by DNA and RNA in Biology, and the tantalizing potential for being able to turn genes "on" or "off" with light. Synthetic challenges of site-specifically incorporating one or more photolabile moieties within a large oligonucleotide, and limitations arising from the available near-UV-activatible caging moieties, have slowed the development of such oligos.

A particular focus for caged oligo development has been antisense morpholinos, which are commonly used to block mRNA translation and modify pre-mRNA splicing in a variety of model organisms, including mouse, zebrafish, frog, sea urchin, and chick.[7] Morpholino antisense oligos are also being investigated for therapeutic applications in humans. Robust methods for photoregulating MO antisense knockdown should enable

the study of multiple, *in vivo* gene functions at specific locations and times, while also reducing the potential for systemic toxicity.

Initial caged antisense oligos from our lab[8-10] and the Chen lab[11-13] employed DNA hairpin-like designs with the antisense oligo conjugated to a shorter, complementary sense strand via a photocleavable linker. Deiters et al. subsequently presented caged morpholinos where multiple photocaged nucleotide monomers were incorporated during solid-phase synthesis.[14] In this example, morpholino-mRNA hybridization was sterically blocked until the caging groups were released from the nucleobases.[14] A newer design strategy, presented by Yamazoe et al.,[15] Wang et al.,[16] and Wu et al.,[17] has involved "circularizing" the oligonucleotide, by attaching the 5′ and 3′ ends with a photocleavable linker. The covalent linkage enforces the closed circular conformation, which prevents efficient MO hybridization to target mRNA; photocleavage restores the linear, biologically active MO. All of these approaches have employed a photocleavable linker, such as *o*-nitrobenzyl or hydroxycoumarin, which yields optimally to near-UV irradiation.[18]

To expand *in vivo* applications using caged oligos, there is need for synthetically versatile photolinkers that can be activated at visible or near-IR wavelengths as near-UV light has poor tissue penetration and can be toxic at high exposure levels.[19-21] Previous strategies include the use of near-IR-to-UV upconversion nanoparticles to achieve siRNA photoactivation in cells and tissues,[20] however, this approach limits the potential for multiplexing experiments involving two (or more) orthogonally caged compounds.

Recently, Yamazoe et al. presented a 465 nm activatable coumarin derivative for MO caging.[22] Here, we exploit versatile ruthenium photochemistry to achieve caged oligos that are efficiently activated with visible light.

Ruthenium complexes of the general type $[Ru(bipyridine)_2(X)_2]^{2+}$, where X = amine,[23] nitrile,[24] pyridine,[25] or thioether[26] ligands, have been shown to undergo facile ligand exchange with solvent upon irradiation with visible one-photon or near-IR two-photon excitation.[1,27] Biologically active small molecules can be directly ligated to the Ru^{2+} center, and then released with visible light.[27] In 2003 Etchenique and coworkers first applied this Ru-ligand exchange property by caging a potassium channel blocker, 4-aminopyridine,[25] and have since caged several neurotransmitters.[23,28,29] More recently, Turro's lab has investigated the ruthenium polypyridyl complexes for their potential as photodynamic drugs.[4,9] Building on these and other Ru-caging examples,[3,12,28,30-32] we set out to develop a Ru-photolinker amenable to caging oligos and other large biomolecules, with the goals of bypassing the harsh synthetic conditions typically required for ligand substitution at Ru^{2+}, and avoiding direct reaction between biomolecules and Ru^{2+}.

Here, we report the synthesis, characterization, and application of the first Ru-photolinker, $[Ru(bipyridine)_2(3\text{-ethynylpyridine})_2]Cl_2$ (RuBEP) (Scheme 3-1). The bis-alkyne functionality enabled circularization of an oligonucleotide containing azides at both 5′ and 3′ termini via [3+2] azide-alkyne copper(I)-mediated cycloaddition reactions.[33,34] In this way, the octahedral Ru^{2+} center remained coordinatively saturated,

and side-reactions between Ru^{2+} and the nucleobases were avoided. Photolysis at 450 nm restored the linear, biologically active oligo (Scheme 3-1).

II. Experimental procedures

A. Synthesis of $[Ru(bpy)_2(3\text{-ethynylpyridine})_2](PF_6)_2$ (RuBEP)

$Ru(bpy)_2Cl_2$ (101.8 mg, 0.20 mmol) and $AgSO_3CF_3$ (105 mg, 0.41 mmol) were suspended in distilled methanol (10 mL). Solution was placed in the freezer overnight under nitrogen. The solution was then brought to rt, filtered to remove AgCl, and 3-ethynylpyridine (3EP, 201.7 mg, 0.40 mmol) was added. The reaction was heated to 75 ^oC for 5 h until no further changes were observed by UV-Vis spectroscopy (Figure 3-1). The methanol was removed under reduced pressure and product was redissolved in boiling water. Solid ammonium hexafluorophosphate was added to the chilled solution until a light orange precipitate was formed. This was vacuum filtered, washed twice with cold water and dried. Compound was further purified by 1.5 x 15 cm silica column (230-400 mesh) with 9:1 dichloromethane:acetonitrile as eluent and isolated in 71% yield (106.6 mg, 0.12 mmol). The water-soluble chloride salt was synthesized by addition of tetrabutylammoniom chloride to a solution of $[Ru(bpy)_2(3EP)_2][PF_6]_2$ dissolved in acetone. The synthetic scheme is shown in Scheme 3-2.

^{1}H NMR (500 MHz, CD_3CN) 3.74 (s, 1H, 3EP-H_5), 7.33 (dd, 1H, J = 7.9, 3EP-H_3), 7.39 (ddd, 1H, J = 6.7, bpy-H_3), 7.82 (ddd, 1H, J = 6.4, bpy-H_6), 7.90 (d, 1H, J = 5.4, bpy-H_1), 7.95 (dd, 1H, J = 5.8, 3EP-H_2), 7.97 (dd, 1H, J = 7.6, bpy-H_2), 8.19 (td, 1H, J = 7.9, bpy-H_7), 8.31 (d, 1H, J = 8.2, bpy-H_4), 8.32 (d, 1H, J = 5.2, 3EP-H_1), 8.38 (s, 1H, 3EP-H_4), 8.40 (d, 1H, J = 7.9, bpy-H_5), 8.95 (d, 1H, J = 5.2, bpy-H_8).

^{13}C NMR (500 MHz, CD_3CN) 78.8, 84.5, 122.8, 124.9, 125.2, 126.9, 128.7, 129.0, 138.9, 139.2, 142.1, 153.5, 153.7, 154.5, 156.5, 158.6, 158.7.

Anal. Calc. for $C_{34}H_{12}N_6RuP_2F_{12}$: C, 65.90; H, 4.23; N, 13.56. Found: C, 66.2; H, 4.30; N, 13.7. MS(ES): *m/2z* 310.06, expected: *m/2z* 310.06

B. Circularization procedure for DNA and morpholino

Reactions were performed on a 10 - 12 nmol scale. Mono-azido DNA and bis-azido DNA was purchased from Integrated DNA Technologies, Coralville, Iowa. Bis-azido morpholinos (Figure 3-2) were custom ordered from GeneTools, Philomath, Oregon. Bis-azido oligonucleotides were premixed with RuBEP at the indicated stoichiometric ratios. Cu(I)Br was dissolved in 3:1 DMSO/t-butanol to make a 0.1 M solution. TBTA ([(1-benzyl-1*H*-1,2,3-triazol-4-yl)methyl]amine) (Anaspec, Freemont, CA) was dissolved in 3:1 DMSO/t-butanol to make a 0.1 M solution. Cu(I)Br and TBTA were mixed in a 1:2 ratio and preincubated. The azide/alkyne solution volume was adjusted to 25 μL (for morpholino reactions) and 50 μL (for DNA reactions). 12% v/v of

the Cu(I)Br/TBTA solution was added to the oligonucleotide solution. Table 3-1 shows relative stoichiometries for click reactions. Solutions were sparged with N_2 and sealed tightly with parafilm. Reactions proceeded for 3 h (DNA) and 24-48 h (MO). Temperatures varying from RT to 55 °C were tested, and no significant correlation was found between temperature and product formation. Additionally, vortexing or not mixing did not seem to change product formation. After reaction completion, a NAP-5 desalting column (GE Healthcare) was used to remove unreacted RuBEP, Cu(I)Br, and TBTA. Circular product was stored in aqueous solution at -20 °C.

Table 3-1. Stoichiometries for DNA and MO circularization reactions

Reagent	nmol
Azido-oligo	10 - 12 nmol
RuBEP	10.0
Cu(1)Br	100.0
TBTA	200.0

C. HPLC purification for N_3-DNA, Ru-DNA, N_3-DNA-N_3, and Ru-cDNA

A gradient of increasing acetonitrile in 0.05 M triethylammonium acetate in H_2O was used with a Zorbax reverse-phase C18 column (Table 3-2). The column was heated to 40 °C during purification. Product elution times are indicated on HPLC traces (Figure 3-3). All purifications were performed on an Agilent 1200 Analytical HPLC using a diode-array detector at 260 nm.

D. Gel-shift assay and PAGE analysis

DNA constructs (25 pmol) were analyzed on 15 % or 20% polyacrylamide, 7M urea gels using Ambion Loading Buffer II (Invitrogen, Grand Island, NY). Gels were run at 300 V for 45 min and stained for 15 minutes with EtBr. Gels were imaged with a Typhoon FLA 7000 imaging system (GE Healthcare Life Sciences, Pittsburgh, PA).

Morpholino constructs (25 pmol) were analyzed using a gel-shift assay. 15% or 20% polyacrylamide, native gels were run with NativePAGE Sample Buffer (4x) (Invitrogen, Grand Island, NY). Running buffer (1X TBE) was cooled to 10 °C on ice and cast gel was preincubated in cold buffer before loading. Samples were prehybridized by heating to 80 °C for 40 minutes and immediately cooled in an ice bath for 10 min. Gels were run in an ice bath for 120 min at 100 V and subsequently stained for 15 minutes with EtBr. Gels were imaged with a Typhoon FLA 7000 imaging system (GE Healthcare Life Sciences, Pittsburgh, PA).

E. Light Sources

A Luxeon III Star® Royal Blue© LED was used for uncaging experiments, purchased from Quadica Developments Inc. (Ontario, Canada). Power measured at the sample was 14 mW/cm^2 with a maximum output wavelength of 450 nm.

A Sapphire Galaxy Blue handheld laser was purchased from Beam of Light Technologies (Oregon, USA) and used to determine the quantum yield of RuBEP. Power measured at the sample was 53 mW/cm^2, with a maximum output wavelength of 450 nm.

F. Molecular beacon hybridization assay

A molecular beacon complementary to bis-azido oligo sequence was designed, with fluorophore, 6-FAM on the 5′ end, quencher, BHQ1 on the 3′ end and a 6-nt complementary stem (Table 3-7). Caging was monitored by the opening of the molecular beacon in the presence of oligonucleotide. Circular oligo was hybridized to the molecular beacon, excited at 494 nm, and fluorescence intensity at 523 nm was quantified. For comparison, the fully complementary linear bis-azido oligo as well as a mismatch sequence, were also monitored. The circular oligo was then exposed to 450 nm light (3 min 14 mW/cm^2), and rehybridized to the molecular beacon. All solutions were made to 1 pmol/μL with a 50 μL volume. All samples were prehybridized prior to analysis, by heating to 80 °C for 30 min, and immediately incubated on ice for 10 min. Samples were analyzed at 10 °C.

Table 3-2. Gradient used for Ru-DNA and Ru-cDNA HPLC purification

Time (min)	% Acetonitrile	% 0.05 M TEAA
0.0	90	10
40.0	40	60
50.0	20	80

G. Zebrafish microinjection experimental details

Zebrafish embryos were obtained from the CDB Zebrafish Core Facilty at the University of Pennsylvania Perelman School of Medicine. All embryos obtained were TLF x TLF (WT). Zebrafish embryo injection solutions were prepared to contain a final

concentration of 0.1 M KCl and 0.25% phenol red dye. All injections were performed at the one-cell stage and injected into the cell compartment only. A Harvard Apparatus PLI-100 pico-injector was used to inject controlled volumes. Injection volume was calibrated to dispense 5 nL per embryo. Zebrafish embryos were incubated at 28 °C in E3 zebrafish medium. All embryos were incubated in the dark, except for irradiated samples, which were exposed to 450 nm light (14 mW/cm^2) for the stated time and returned to the dark incubator. Embryo micrographs were collected at 24 hpf with an Olympus FV1000 laser scanning confocal microscope using transmitted light imaging. A 10x air objective was used for single embryo imaging and 4x air objective was used for multiple embryo imaging.

H. Materials

Organic reagents and solvents were used as purchased from the following chemical sources: Methanol, methylene chloride (HPLC grade), acetonitrile (HPLC grade), and acetone were purchased from Fisher Scientific. *Cis*-dichloro-bis(2,2'-bipyridine)ruthenium(II) (98%), 3-ethynylpyridine (96%), silver trifluoromethansulfonate (99+%), ammonium hexafluorophosphate (99.5%), acetonitrile-d^3 (99.8 atom%), tetrabutylammonium chloride hydrate (98%), deuterium oxide (99.8 atom%) were purchased from Acros Organics.

Complementary DNA oligonucleotides, azido-DNA oligonucleotides, and molecular beacons were custom synthesized and HPLC purified by Integrated DNA

technologies (Coralville, IA). Azido-MOs were custom synthesized by Gene Tools (Philomath, Oregon). All gel reagents were purchased from Bio-Rad (Hercules, CA). TBTA ligand (Tris[(1-benzyl-1*H*-1,2,3-triazol-4-yl)methyl]amine) was purchased through Anaspec (Fremont, CA). Zebrafish embryos were obtained through the CDB Zebrafish Core Facilty at the University of Pennsylvania Perelman School of Medicine.

I. Instrumentation

A Luxeon III Star® Royal Blue© LED was used for uncaging experiments post-click reactions, including *in vivo* work. It was purchased from Quadica Developments Inc. (Ontario, Canada) with a maximum output wavelength of 450 nm. Measured power at sample was 14 mW/cm^2.

A sapphire Galaxy Blue handheld laser was purchased from Beam of Light Technologies (Oregon, USA) and used to determine the quantum yield of RuBEP. Measured power at the sample was 53 mW/cm^2, with a maximum output wavelength of 450 nm.

UV-Visible spectroscopy was performed using an Agilent 8453 UV-Visible spectrometer (Agilent Technologies, Germany) in water unless otherwise specified. ^1H NMR spectra were obtained on a Bruker DMX 500 spectrometer, and ^{13}C NMR spectra were obtained using a Bruker AVIII cryo500 probe spectrometer at the University of Pennsylvania NMR facility and were recorded at room temperature. The ^1H and ^{13}C spectra were referenced to the central line of the solvent residual or to TMS at 0.00 ppm.

^{1}H NMR and ^{13}C NMR chemical shifts (δ) are given in parts per million and reported to a precision of ± 0.01 and ± 0.1 ppm, respectively. Proton coupling constants (J) are given in Hz and reported to a precision of ± 0.1 Hz.

High-resolution mass spectra (HRMS) were obtained using electrospray ionization (ESI) mass spectrometry on a Micromass Autospec at the Mass Spectrometry Facility in the Department of Chemistry at the University of Pennsylvania. Irradiated sample was analyzed via direct infusion nanospray with a Thermo ORBI trap XL mass spectrometer at 60 K resolution. Gels were imaged with a Typhoon FLA 7000 imaging system (GE Healthcare Life Sciences, Pittsburgh, PA).

All purifications were performed on an Agilent 1200 Analytical HPLC using a diode-array detector set to 260 nm. A 5-micron Zorbax semi-preparatory C18 column (9.4 x 215 mm) was used for all reverse-phase purifications.

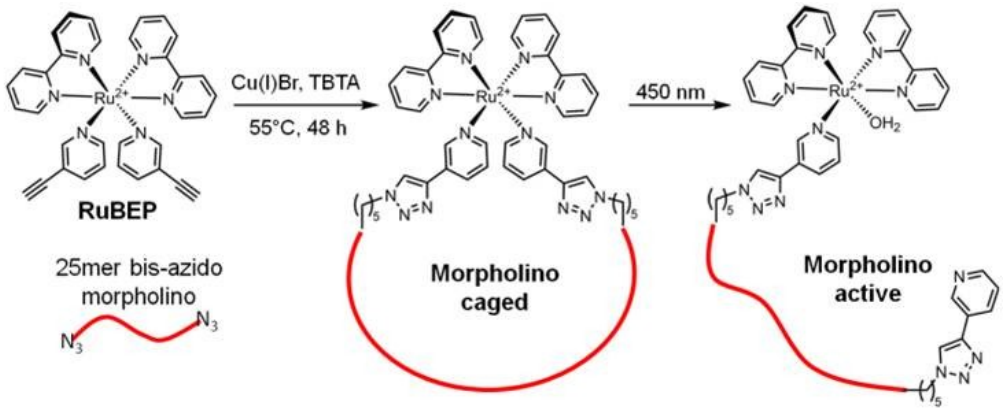

Scheme 3-1. RuBEP conjugation and irradiation

Photolinker RuBEP conjugation with 25mer bis-azido morpholino to form "caged" antisense MO. 1,4-regioisomers of 1,2,3-triazoles are the sole product of the copper(I)-catalyzed azide-alkyne cycloaddition (CuAAC). Subsequent 450-nm irradiation restores biologically active MO.

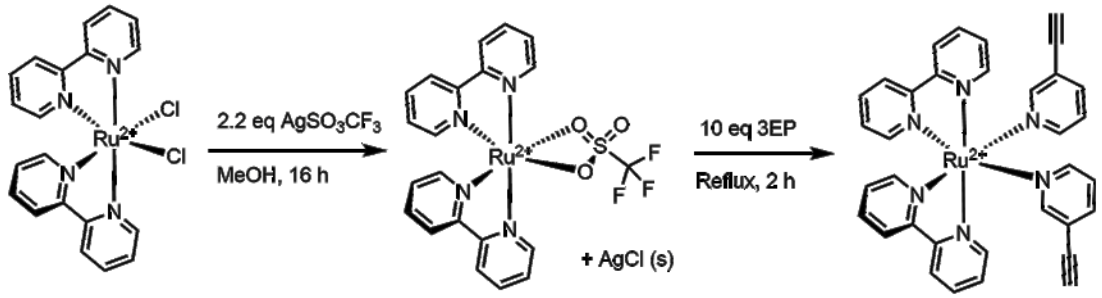

Scheme 3-2. Synthetic scheme of RuBEP

RuBEP was synthesized from $Ru(bpy)_2Cl_2$ via a two-step synthesis.

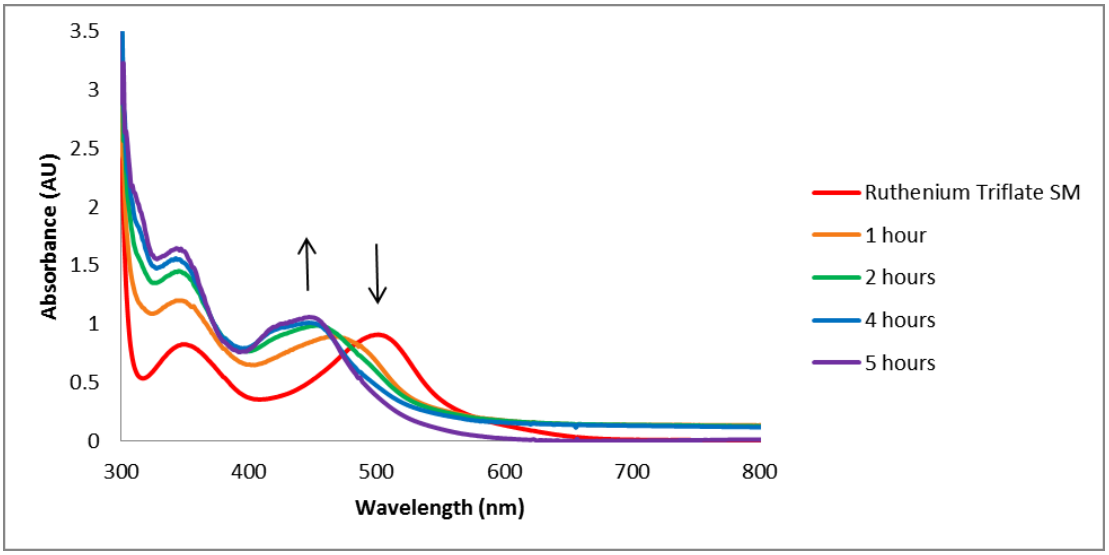

Figure 3-1. UV/Vis monitoring product formation

UV-Vis spectra of RuBEP synthesis reacted in methanolat75 ^{o}C. The peak at 520 nm was due to $Rubpy_2OTf$, which disappeared as RuBEP was formed to give the double peak near 450 nm.

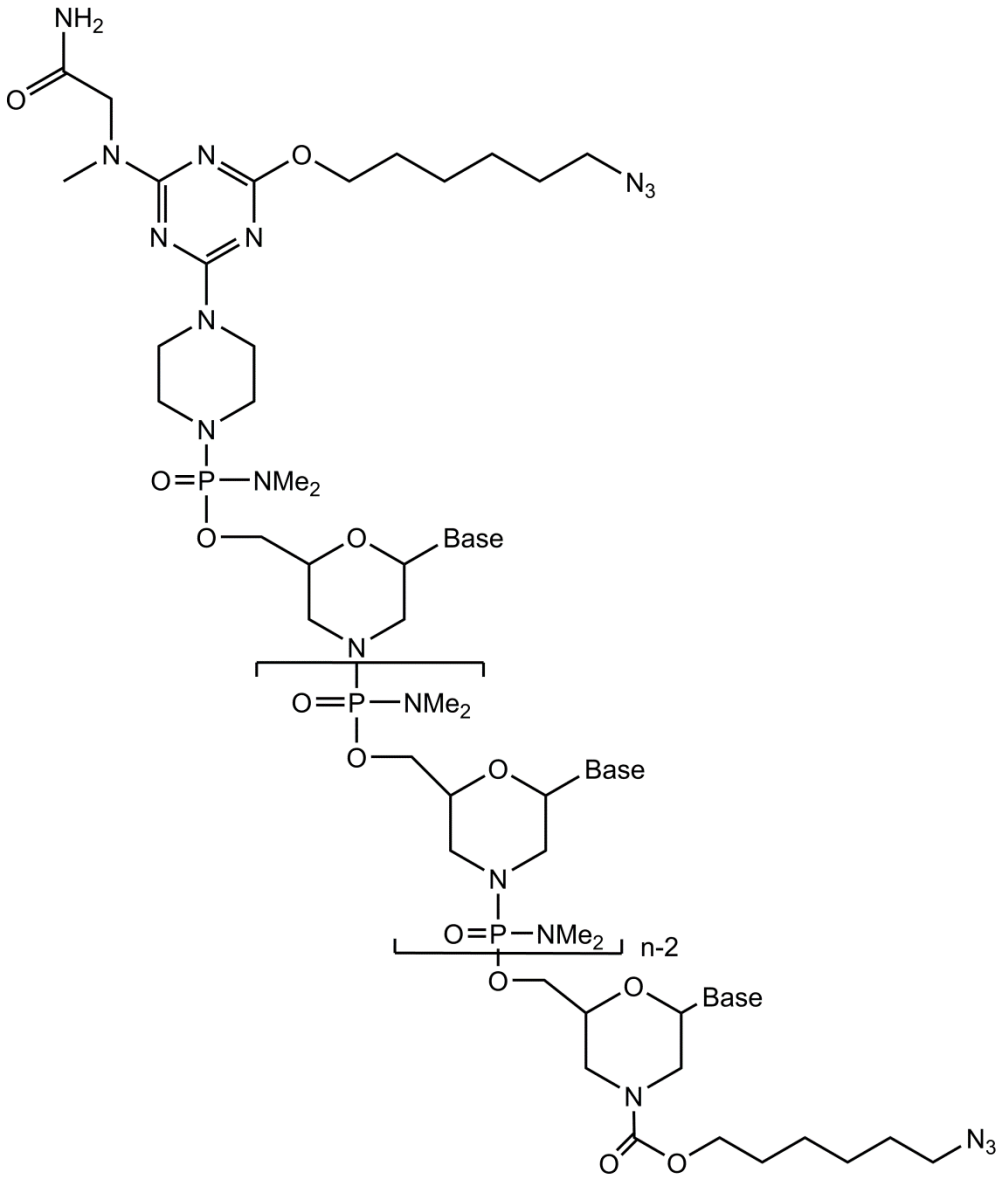

Figure 3-2. Structure of bis-azido morpholino

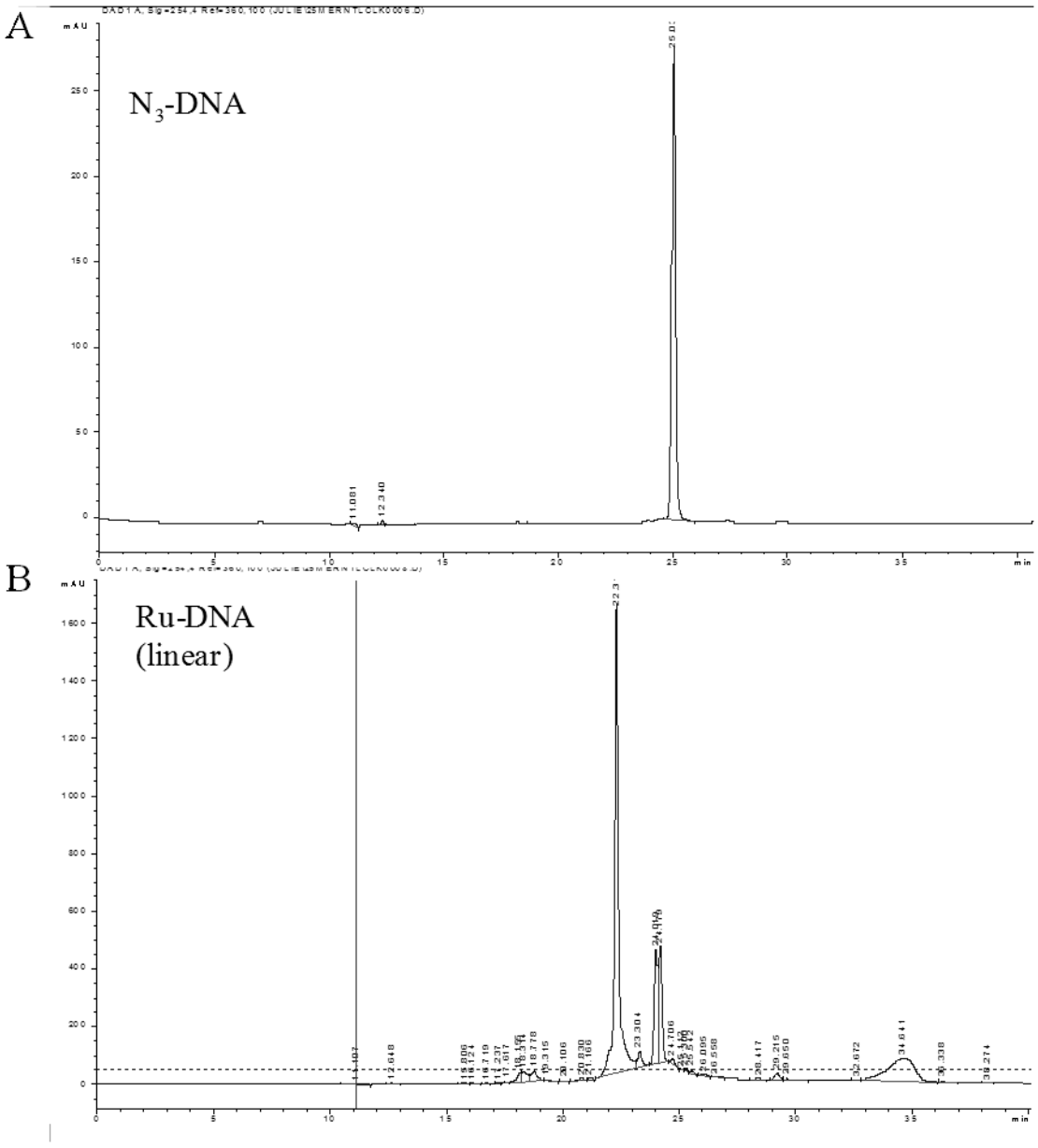

Figure 3-3. HPLC traces for N_3-DNA.

A) N_3-DNA eluted at 25.0 min and B) Ru-DNA after click reaction eluted at 22.3 and 24.1 min using gradient shown in Table 3-2.

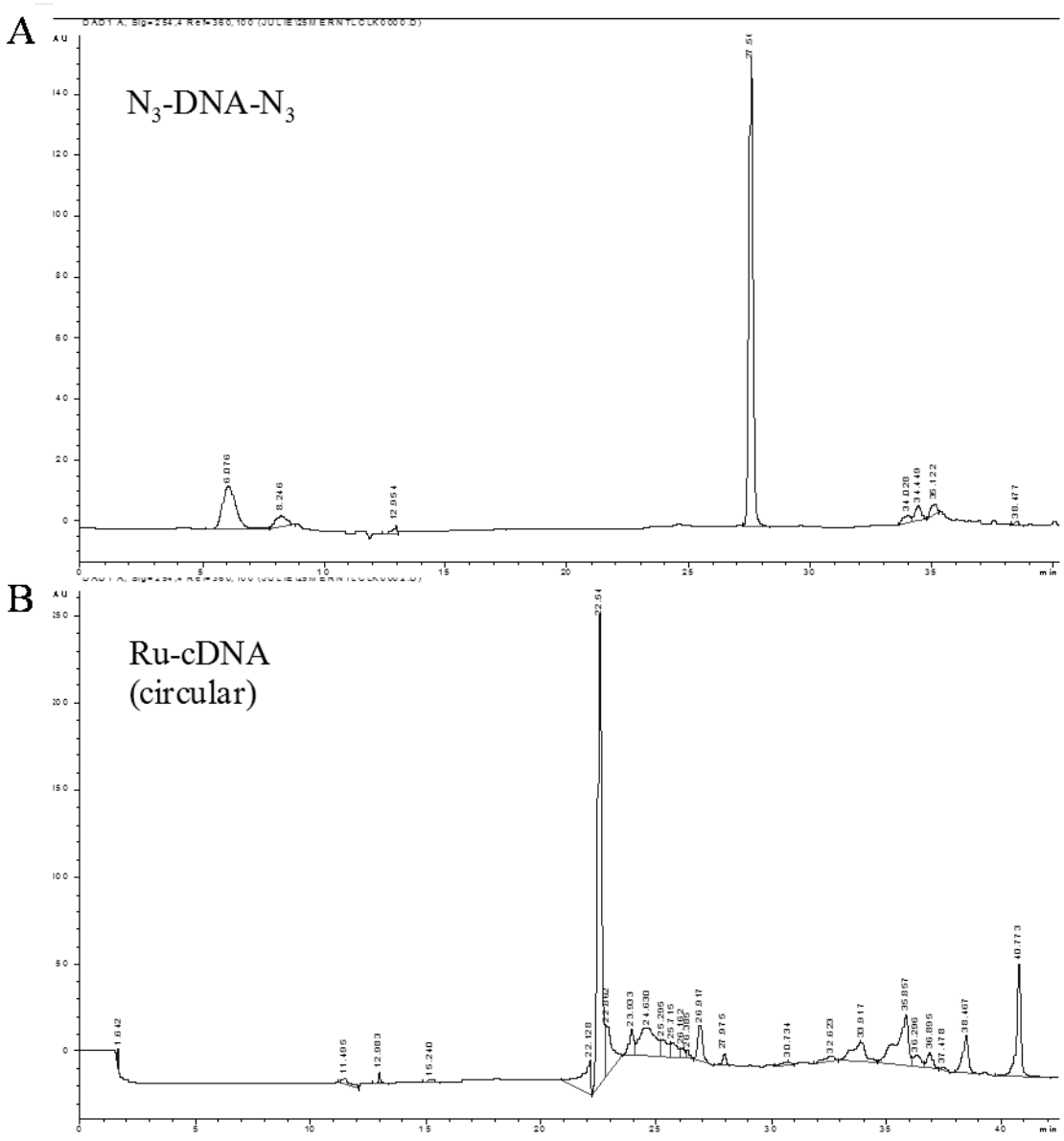

Figure 3-4. HPLC traces for N_3-DNA-N_3

A) N_3-DNA-N_3 eluted at 27.5 min and B) Ru-cDNA after click reaction eluted at 22.5 min using gradient shown in Table 3-2.

III. Results and Discussion

A. RuBEP

The RuBEP photolinker was synthesized from $Ru(bpy)_2Cl_2$ and 3-ethynylpyridine (3EP) by modifying a published procedure.[9] Reaction progress was monitored by the appearance of an MLCT band at 450 nm (Figure 3-1). Precipitation with tetrabutylammonium chloride produced the water-soluble chloride salt, RuBEP, which was characterized by X-ray crystallography (Appendix A), ESI-MS (Figure 3-6), ^1H and ^{13}C NMR (Figure 3-7), and elemental. X-ray crystallography revealed a 92° angle between alkyne linkers, confirming correct geometry for circularization applications (Figure A1-1).

Photodissociation of the 3-ethynylpyridine ligand from RuBEP was monitored by LCMS (Figure 3-6), UV-Vis (Figure 3-5) and NMR (Figure 3-7) spectroscopies. Upon continuous irradiation of RuBEP in water with 450 nm light (53 mW/cm^2), the λ_{max} red-shifted from 450 nm to 473 nm (Figure 3-5). Photolysis of the bulk RuBEP solution (80 μM) was detectable within the first 20 s, with complete dissociation in 5 min. In addition to the wavelength shift, a very obvious color change was also present, as shown in Figure 3-5, inset. The orange photo-product ($[Ru(bpy)_2(3EP)(OH_2)]^{2+}$) was consistent with previously characterized $[Ru(bpy)_2(pyr)(OH_2)]^{2+}$ complexes.[35] Two isosbestic points were observed (Figure 3-5), consistent with the exchange of one ligand for a solvent.[24] ^1H NMR also showed the exchange of only one 3EP ligand with a solvent water

molecule, based on an observed shift in alkyne peak and change in integration (Figure 3-7). HR-MS also confirmed the photoproduct assignment with a mass change from 620 Da to 552 Da (Figure 3-6).

To probe toxicity of RuBEP *in vivo*, 1-cell stage zebrafish embryos were microinjected with 1 mM RuBEP and subjected to either 450 nm light (14 mW/cm^2, 5 min), or incubated in the dark. Concentrations for *in vivo* experiments are significantly lower than this concentration, typically 0.1 - 0.5 mM. Both batches of embryos were observed to remain healthy and develop normally, whether incubated in the dark or irradiated with visible light, and survival rates were comparable to the uninjected control.

To determine the efficiency of ligand exchange, the quantum yield in water under ambient oxygen (ϕ= 0.33 +/- 0.06) was determined by fitting the initial kinetics of the photoreaction (Figure 3-8). The quantum yield for RuBEP was determined to be comparable to the quantum yield of ligand exchange measured for $Ru(bpy)_2(pyridine)_2Cl_2$, showing that the electronics of the added alkyne does not have much effect on the efficiency.[25] The uncaging efficiency for RuBEP—defined as ε_{450} times ϕ—was determined to be 2.0 x 10^3 $M^{-1}cm^{-1}$ at 450 nm, which is much higher than measured for typical organic chromophores activated at near-UV wavelengths. Commonly used nitrobenzyl derivitives, such as the o-nitrobenzyl caging group used in previous caging methods in our lab have 1-P uncaging efficiencies less than 100 $M^{-1}cm^{-2}$ at 365 nm.[4,36]

B. Ru-cDNA

Initial efforts in circularization were focused on using a DNA oligonucleotide. Although DNA does not have antisense activity in zebrafish embryos, the use of DNA allowed for proof-of-concept experiments and protocol development due to ease of solubility and ability to purify using reverse-phase HPLC. Using RuBEP as photolinker, circularization protocols were initially investigated using a bis-azido 25mer DNA oligonucleotide.

The [3+2] Cu(I)-mediated cycloaddition reaction was performed at a stoichiometry of 1.2 DNA:1 RuBEP, and monitored by polyacrylamide gel electrophoresis. A time-course gel was used to follow reaction progression and product formation. A band migrating faster than the bis-azido DNA appeared within the first 15 min of reaction (Figure 3-9). A faster migrating band is consistent with circularization, as a more compact, circular structure would have this effect. Additionally, the positive charge contributed by RuBEP could also play a role in gel migration speed. To confirm that this was the Ru circularized DNA (Ru-cDNA) and not RuBEP clicked to two linear DNA oligos (DNA-RuBEP-DNA), a mono-azido DNA was subjected to the same reaction conditions, which resulted in a slower migrating band (Figure 3-10).

In addition to circular product, formation of polymer and dimer also occurred. This is especially apparent with the bis-azido DNA (Figure 3-9, lanes 2-3), which is expected due to the two azides. Although the 1.2:1 DNA to RuBEP stoichiometry should favor only one linker per oligo and subsequent circularization, other 1:1 structures could

form as well such as Ru-DNA-Ru-DNA, and an equal combination of RuBEP-DNA-RuBEP and DNA-RuBEP-DNA. These side products became less apparent on the gel after the first 30 minutes of reaction (Figure 3-9) which is likely because these RuBEP-DNA polymers were less soluble and didn't remain in solution with extended reaction times. The mono-clicked product is visible on the gel in the first 15 minutes (Figure 3-9, Lane 2), showing that initially one side reacts, and then due to stoichiometry and concentration favoring circularization, an intramolecular reaction occurs. As expected, significantly less polymer formation was formed with the mono-azide DNA reaction than with RuBEP (Figure 3-10, Lane 2). A secondary band migrating slower than the linear Ru-DNA was the only significant side product, likely a DNA-RuBEP-DNA dimer due to the presence of two alkynes on RuBEP.

The reaction products for both the Ru-cDNA and Ru-DNA were readily isolated by reverse-phase HPLC (Figures 3-3 A-B, Table 3-2). The retention times for the mono-azide and bis-azido DNA differed by 2.5 min (25.0 vs 27.5 min for mono- vs. bis-azido DNA). However, retention time for both Ru-DNA and Ru-cDNA were both very similar (22.3 vs 22.5 min for Ru-DNA vs Ru-cDNA). These two constructs are very similar in many aspects such as hydrophobicity, charge, and molecular weight, making HPLC separation very challenging with reverse phase and ion-exchange methods. To circumvent this, reaction conditions were optimized so that no Ru-DNA remained in the Ru-cDNA reaction. The Ru-cDNA and Ru-DNA could be readily separated from other reaction products using reverse-phase HPLC. Figure 3-11 shows successful isolation of

pure Ru-cDNA after HPLC purification. Circularization occurred with greater than 80% efficiency (determined by gel band intensity quantification) and approximately 25% was recovered after HPLC purification.

To probe circularization and caging, a molecular beacon (MB) complementary to the N_3-DNA-N_3 sequence was designed with fluorophore 6-FAM on the 5′ end and quencher BHQ1 on the 3′ end, with a 6-nt complementary stem (Table 3-7). A calibration curve was made with DNA:MB ratios of 0:1 to 5:1 to confirm opening of the molecular beacon with complementary bis-azido DNA (Figure 3-12). With RuBEP holding the 25mer DNA in a circular conformation, the ability to fully hybridize to a complementary DNA is hindered. Four different conditions were tested. MB with a scrambled sequence MB with a fully complementary bis-azido linear sequence, MB with Ru-cDNA, and MB with Ru-cDNA exposed to 450 nm (14 mW/cm^2, 5 min) (Table 3-7). Caging, indicative of circularization, was monitored by the opening of the molecular beacon in the presence of oligonucleotide. Ru-cDNA was hybridized to the molecular beacon, and fluorescence intensity at 523 nm was quantified. Fluorescence intensity for the linear DNA was normalized to 100% (Figure 3-13). For comparison, the fully complementary linear bis-azido DNA as well as a DNA scramble sequence were also monitored. Circularization and caging of the Ru-cDNA was confirmed by a 2.3-fold lower fluorescence intensity when compared to the linear complementary DNA (Table 3-3), under thermal annealing conditions that greatly favored hybridization. After visible light exposure, fluorescence intensity was restored to match the intensity of the bis-azido complementary DNA. This

confirms complete uncaging and hybridization restoration upon short exposure to blue light.

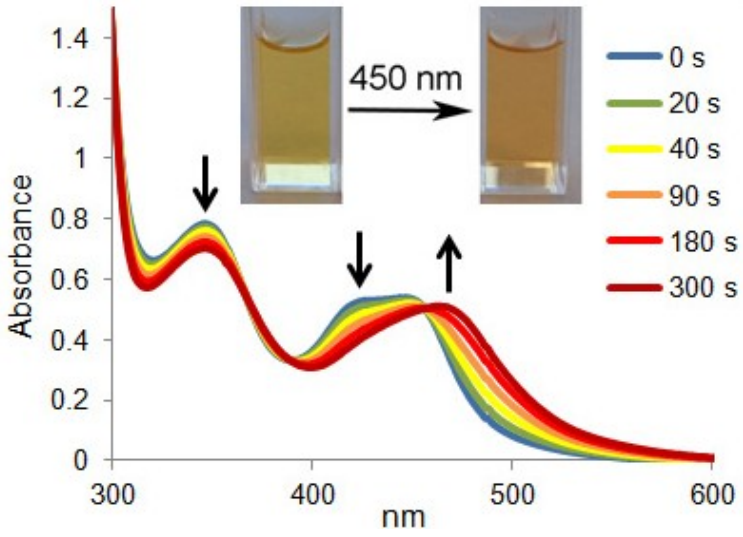

Figure 3-5. Change in UV-Vis spectrum of RuBEP upon 450-nm focal irradiation.

RuBEP in H_2O was continuously irradiated with 450 nm (53 mW/cm^2) and wavelength shift was monitored. Two isosbestic points were detected. A yellow to orange color change was visible upon ligand exchange (inset).

A

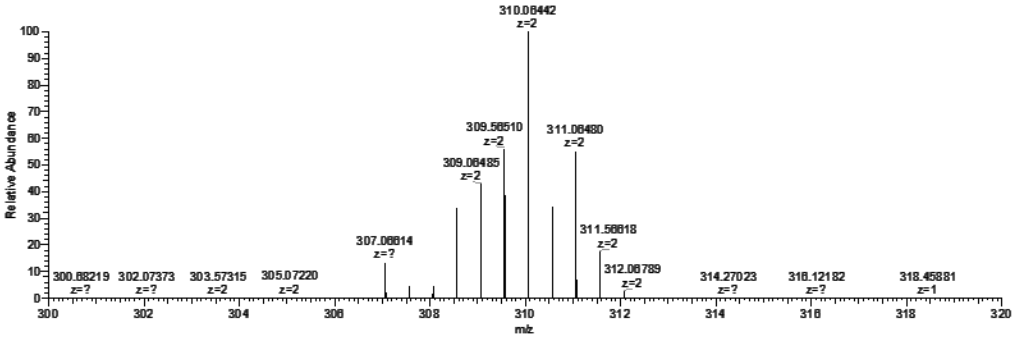

B

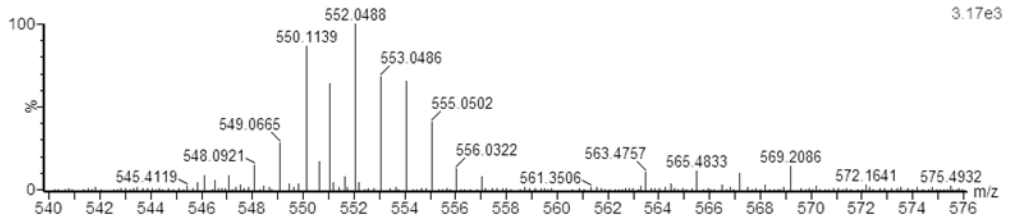

Figure 3-6. Electrospray mass spectrometry of [RuBEP])$PF_6)_2$ +/- light

A) RuBEP PF_6 salt before irradiation, showing a doubly charged species at 310.06 Da. Expected mass = 620.13 Da (z=1), 310.06 Da (z=2) B) RuBEP + 450 nm (5 min, 14 mW/cm^2) showing singly charged species at 552.05 Da, confirming the exchange of one 3EP ligand upon irradiation. Expected mass = 552.02 Da (z=1)

A

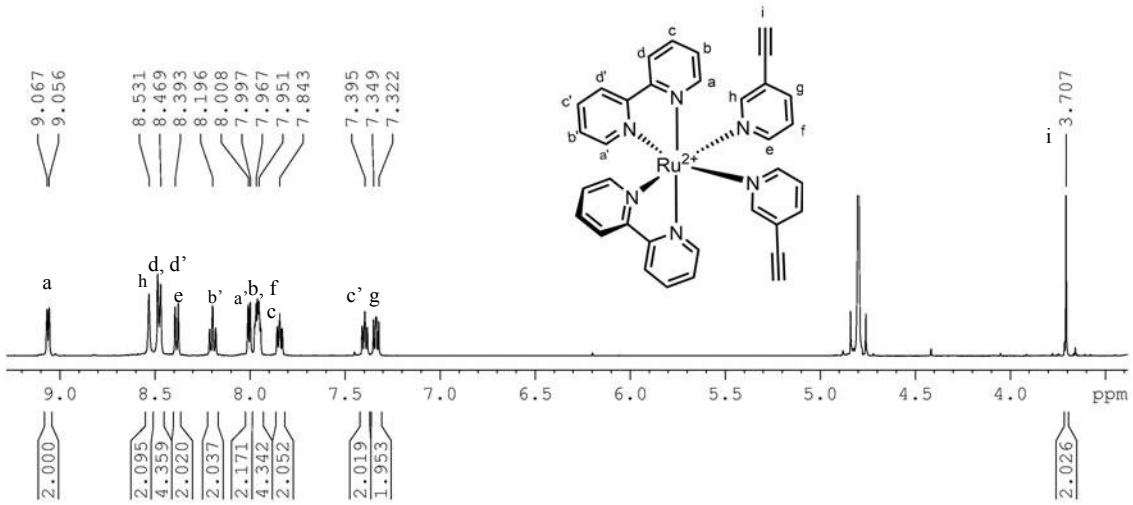

B

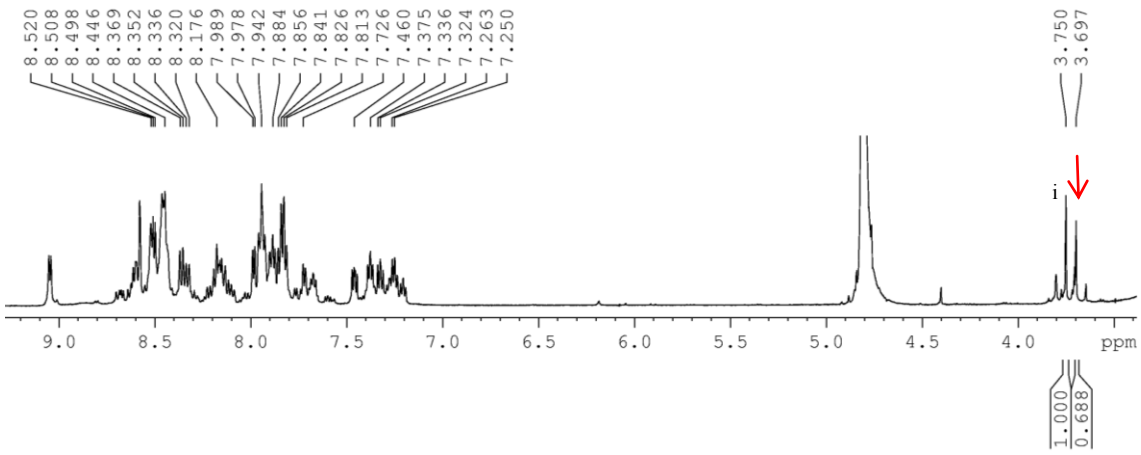

Figure 3-7. ^{1}H NMR, pre- and post-photolysis of RuBEP in D_2O.

A) Pre-photolysis 1H NMR. B) Post-photolysis 1H NMR (+450 nm, 5 min, 14 mW/cm2) showing the appearance of a free 3-EP peak, and change in integration for bound 3-EP peak. The appearance of a second alkyne peak confirms one ligand exchange with solvent (D_2O).

A

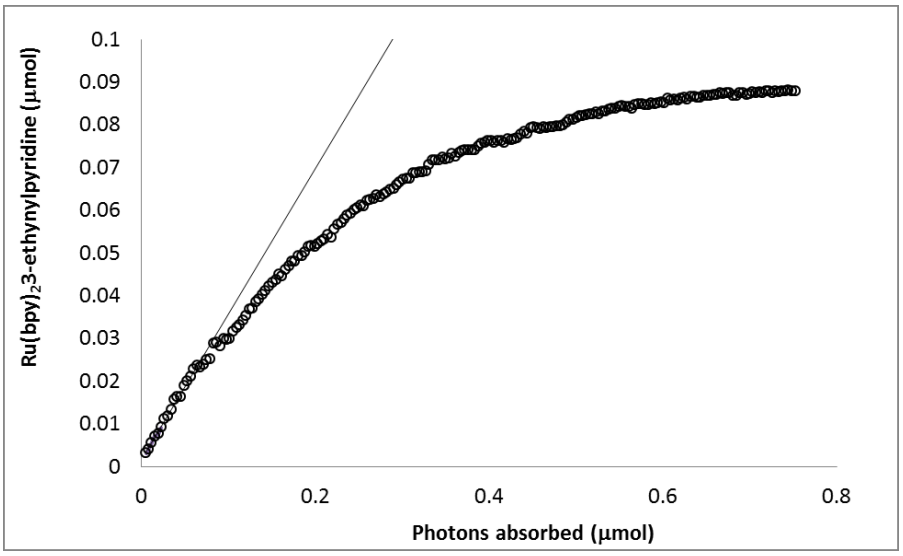

B

Moles Product $Ru(bpy)_2 3EP(OH_2)$ = initial moles RuBEP – current moles RuBEP (1)

$$\text{current moles RuBEP} = \left(\frac{\text{Abs}-\varepsilon_p[\text{RuBEP}]_i}{\varepsilon_s-\varepsilon_p}\right)\times V_{cuvet} \quad (2)$$

$$\text{photons absorbed} = \frac{E}{P_l} \quad (3)$$

Where:

P_l = net power of the laser during the trial (mW)
E = energy of 450 nm light (J/photon)
ε_s = extinction coefficient of RuBEP (starting material) at 475 nm = 1800 $M^{-1}cm^{-1}$
ε_p = extinction coefficient of $Rubpy_2(3EP)(H_2O)$ (product) at 475 nm = 3800 $M^{-1}cm^{-1}$

Figure 3-8. Quantuim yield determination of RuBEP.

A) Kinetics trace of ligand dissociation of 14 μM RuBEP (0.2 OD) upon exposure 450 nm laser (53 mW/cm^2) under ambient conditions. Abs_{473} was monitored to determine formation of product, $Ru(bpy)_2(3\text{-}EP)(H_2O)Cl_2$. B) Equations for quantum yield of photorelease calculation. Quantum yield was determined to be 0.33 ± 0.06.

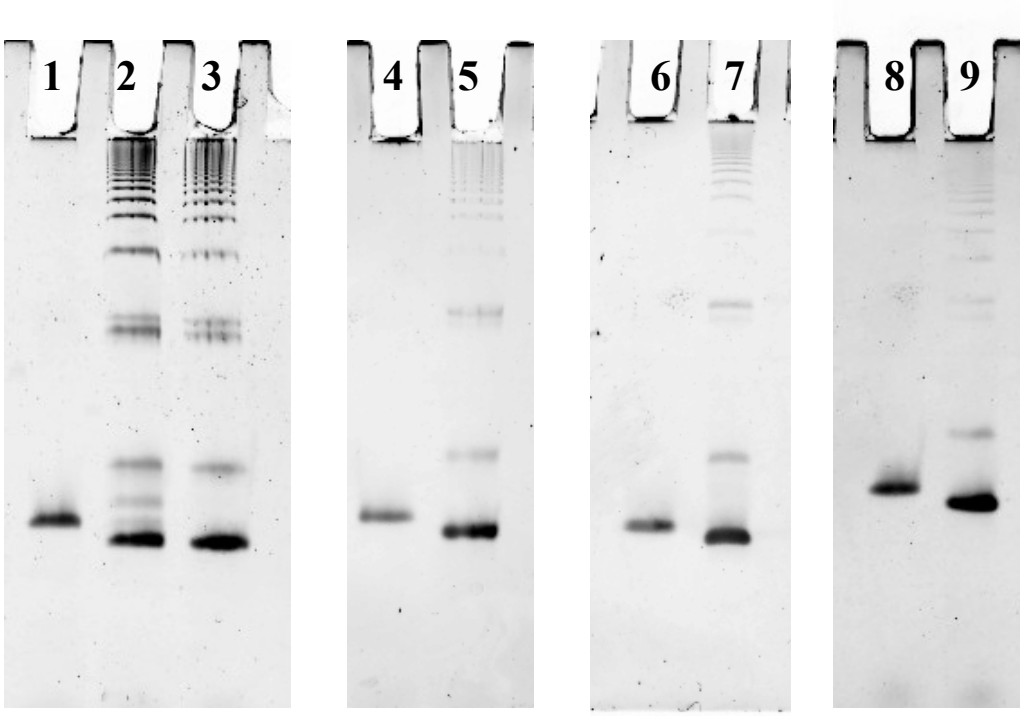

1 – N_3-DNA-N_3
2 – 15 min rxn
3 – 30 min rxn

4 – N_3-DNA-N_3
5 – 1 h rxn

6 – N_3-DNA-N_3
7 – 2 h rxn

8 – N_3-DNA-N_3
9 – 3 h rxn

Figure 3-9. Time-course gel of DNA circularization

25 pmol aliquots were removed over the course of the DNA circularization reaction. Each aliquot was run on a 15% PAGE/ 7M urea gel at 300 V for 45 min and stained for 15 min with EtBr. Click reaction aliquots were compared to the linear bis-azido DNA migration (lanes 1, 4, 6, 8). Circular product appeared as the fastest migrating band, within the first 15 min of the reaction, with more product formation at 3 h (lane 9).

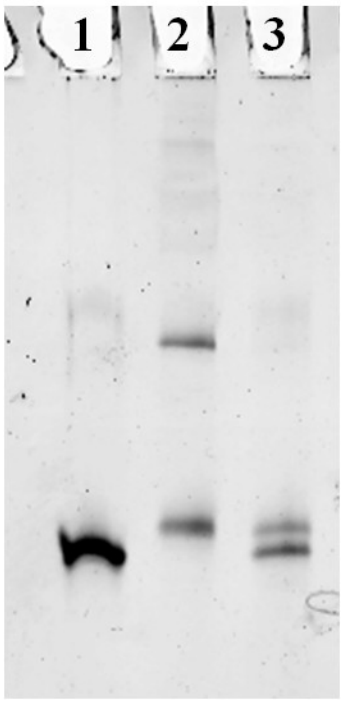

Figure 3-10. Mono-azide DNA click reaction

Lane 1 – N_3-DNA only, Lane 2 – N_3-DNA clicked, Lane 3 – N_3-DNA clicked + 450 nm light.

A mono-azido DNA 25mer was subjected to the same conditions given above for the bis-azide DNA. The circularization efficiency was monitored on a 15% PAGE/7 M urea gel, run for 45 min at 300 V. The gel was stained for 15 min with EtBr. A band (lane 3) running slower than the N_3-DNA appeared, and intensity was decreased after photolysis. Only 50% decrease in photoloysis was seen, as only one 3EP ligand on RuBEP will exchange upon light exposure. The higher band in lane 2 is likely dimer, DNA-RuBEP-DNA.

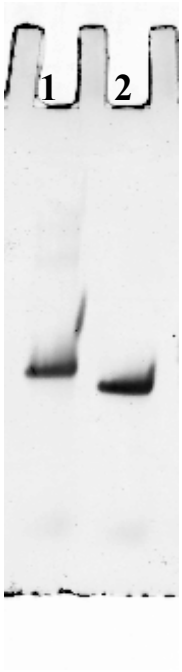

Figure 3-11. 20%, 7 M urea PAGE analysis of Ru-cDNA after HPLC purification

HPLC isolation of Ru-cDNA from Figure 3-4B. Lane 1. N_3-DNA-N_3 (T_R = 27.5), Lane 2. Ru-cDNA after HPLC purification (T_R = 22.5 min)

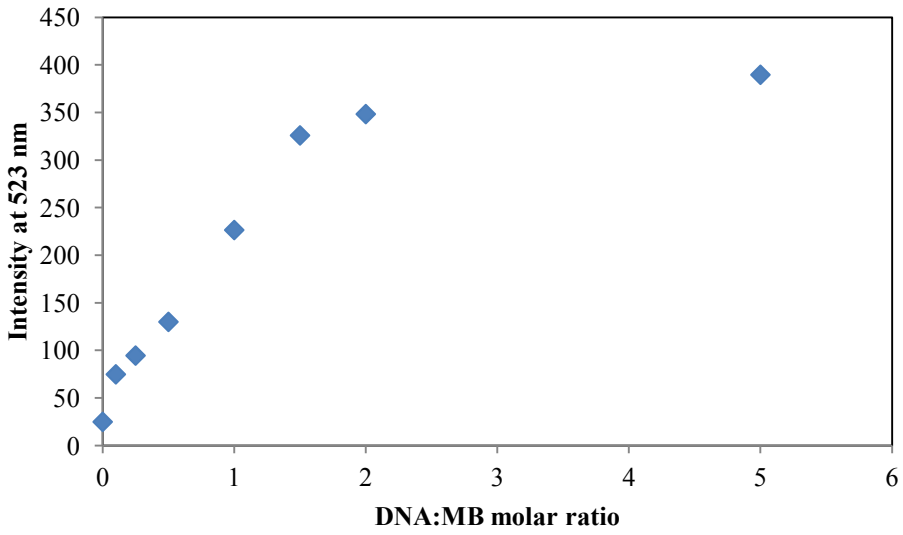

Figure 3-12. Calibration curve for molecular beacon targeting *ntl*

To confirm opening of MB in presence of fully complementary MO, linear *ntl*-MO was hybridized to MB in ratios ranging from 0.1:1 to 5:1 and fluorescence intensity was measured at 523 nmafter thermal annealing.

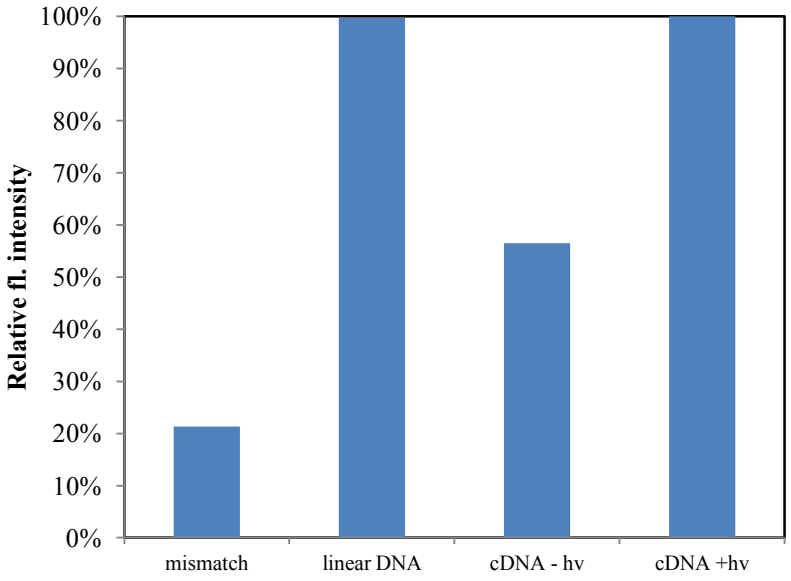

Figure 3-13. Molecular beacon hybridization assay for Ru-cDNA

Molecular beacon fluorescence assay showing less probe hybridization to caged Ru-cDNA compared to the linear DNA or Ru-cDNA after 3-min exposure to 450-nm light. Samples were annealed prior to molecular beacon assay to promote hybridization.

Table 3-3. Relative fluorescence intensities for molecular beacon targeting *ntl*-DNA

	Relative fl. intensity at 523 nm
background	0
mismatch	21.3%
circular caged	56.5%
complementary N_3-DNA-N_3	99.6%
circular uncaged	100%

C. Ru-cMO

In order to photoregulate gene expression in living zebrafish embryos, two early developmental zebrafish genes were targeted, *notail* (*ntl*) and *chordin* (*chd*), due to their well characterized and easily recognizable knockdown phenotypes with antisense MOs.[37] Examples of these knockdown phenotypes are shown in Figures 3-14 and 3-15. Upon knocking down *chd* with an antisense MO, zebrafish embryos will develop with a decreased head size, U-shaped somites, and a large "blood island" on the tail (Figure 3-14). Knocking down *ntl* with an antisense morpholino results in zebrafish embryos with a decreased head size, U-shaped somites, no notochord, and no posterior structures. These phenotypes can range from mild to severe depending on the morpholino dose. Control morpholino doses for both *chd* and *ntl* were titrated by injecting varying concentrations of morpholino to achieve the strongest phenotype while limiting toxicity and off-target effects. These optimal concentrations were found to be 0.5 mM and 0.25 mM for *chd* and *ntl*, respectively.

The RuBEP-DNA circularization conditions were subsequently applied to antisense MOs (Scheme 3-1). Bis-azido MOs were purchased from Gene Tools (Philomath, OR) and added to RuBEP in a 1.05:1 ratio in the presence of 10x Cu(I)Br and 20x chelator, TBTA (Table 3-1). These reaction conditions promoted reaction of one RuBEP per MO, thus favoring intramolecular reaction and circularization. Reaction conditions varied slightly depending on sequence, as solubility of morpholinos is related to the number of guanine residues in the sequence. For *chd*, 10.5 nmol MO was added to

10 nmol RuBEP in 25 µL. The reaction volume for *ntl* was increased to 100 µL to increase solubility (due to higher guanine content). The reaction proceeded for 24-48 h at rt. Although product was formed within the first 15 minutes of the reaction, product was maximized after 24-48 h (Figure 3-18).

Due to the neutral charge of morpholinos, the click product, Ru-cMO could not be analyzed using standard PAGE or HPLC as Ru-cDNA was. Instead, formation of Ru-cMO was monitored by gel-shift assay employing a 25mer complementary DNA strand. The control MO or Ru-cMO was hybridized to a complementary DNA to provide charge density for gel migration. This MO:DNA hybrid was run on a 15% native polyacrylamide gel on ice (100 V, 120 min) and stained with ethidium bromide, shown in Figure 3-16. As expected, the complementary DNA (lane 1) ran slower when hybridized to linear bis-azido MO (lane 2). Upon circularization (lane 3), the Ru-cMO:DNA hybrid migrated even slower, which can be attributed to its weaker duplex stability. An additional band (band 4) is seen in lane 3 likely due to the less stable duplex causing dehybridization of some DNA during the gel-shift assay. Photoactivation at 450 nm (14 mW/cm^2, 3 min) resulted in complete uncaging, yielding a mono-Ru-functionalized linear MO that was hybridized to DNA (lane 4) and ran comparably to the MO:DNA hybrid (lane 2). All lanes contained stoichiometric complementary DNA (lowest band) to promote hybridization. For Ru-cMO-*chd*, QuantIT band quantification showed less than 5% unreacted bis-azido MO after 48-h RuBEP reaction (Figure 3-16). Typical reaction yields ranged from 87–95% circularization, determined by band size and intensity

quantification. No additional purification of Ru-cMO was necessary due to high circularization efficiency. Reaction efficiency for Ru-cMO-*ntl* was slightly lower and contained a linear Ru-MO side reaction, due to mono-azido MO impurity in the bis-azido MO obtained from Gene Tools (Figure 3-17).

A molecular beacon was designed targeting *chd*-MO, with a fluorophore (5'-FAM) and quencher (3'-BHQ1), and 6-nt complementary stem (Table 3-7). The molecular beacon fluorescence assay was performed to confirm caging of the Ru-cMO-*chd* construct. Fluorescence signal from the molecular beacon was very strong when hybridized to linear MO (Figure 3-19), setting the baseline for this measurement. By comparison, fluorescence intensity was 2.6-fold lower with Ru-cMO-*chd*, indicative of caging. After exposure to 450 nm light (14 mW/cm^2, 3 min) the fluorescence intensity was restored within error of the linear MO, confirming complete uncaging. These data agreed well with the gel-shift assay (Figure 3-16) which also showed that some hybridization occurred, although to a lesser extent than the linear control. This can be attributed to forced hybridization through heating and cooling in both the gel and the molecular beacon assay.

The circular construct, Ru-cMO-*chd,* was tested *in vivo* in living zebrafish embryos to assess the ability to photoregulate gene expression with RuBEP caged morpholinos. Ru-cMO-*chd* (514 pmol/μL) was microinjected into zebrafish embryos at the one-cell stage. Half of the injected embryos were incubated at 28 °C in the dark, while the other half were irradiated with 450 nm light (14 mW/cm^2, 5 min). Another

batch of embryos were injected with control linear bis-azido MO targeting *chd* at the same concentration. At 24 hpf, the embryos were scored for phenotypic response (Table 3-4) and imaged.[38] Figure 3-20(A-D, E) shows representative images of the phenotypic response and embryo phenotype scoring at 24 hpf. Figure 3-20A shows the uninjected control emrbyos, where 100% developed as expected for wildtype TLF x TLF zebrafish. In contrast, Figure 3-20D shows embryos injected with the control linear MO. These embryos developed with varying degrees of *chd* knockdown phenotype, with 95% showing a severe or moderate phenotype. A small percentage of these embryos (5%) developed normally, which can be attributed to injection error. Embryos injected with Ru-cMO-*chd* followed similar phenotypic trends as the controls. For the embryos incubated in the dark, >86% developed normally, comparable to the uninjected control. Embryos exposed to blue light developed similarly to the linear MO-*chd* control injection. Over 92% of the embryos developed with the *chd* knockdown phenotype, with greater than half of the embryos displaying a severe phenotype as was seen with the linear MO-*chd* control. This confirms that the retained Ru moiety on the uncaged MO does not affect MO activity *in vivo*. This is consistent with the molecular beacon assay, where Ru-cMO after uncaging behaved identical to linear bis-azido MO. The 8% of embryos with normal development can be attributed to injection variability.

To confirm sequence-specificity, identical experiments were performed with a second gene, *ntl*[39] (Figure 3-21). Similar caging results were obtained with Ru-cMO-*ntl*, however, background MO activity was slightly higher. Of the embryos incubated in the

dark, 4% developed with class IV phenotype (severe), however, a significant percentage (26%) developed with a class II phenotype. This background activity can be attributed to the linear Ru-MO due to the mono-azide impurity in the starting material from Gene Tools (Figure 3-17). The embryos irradiated with blue light developed with varying degrees of the *ntl* phenotype.

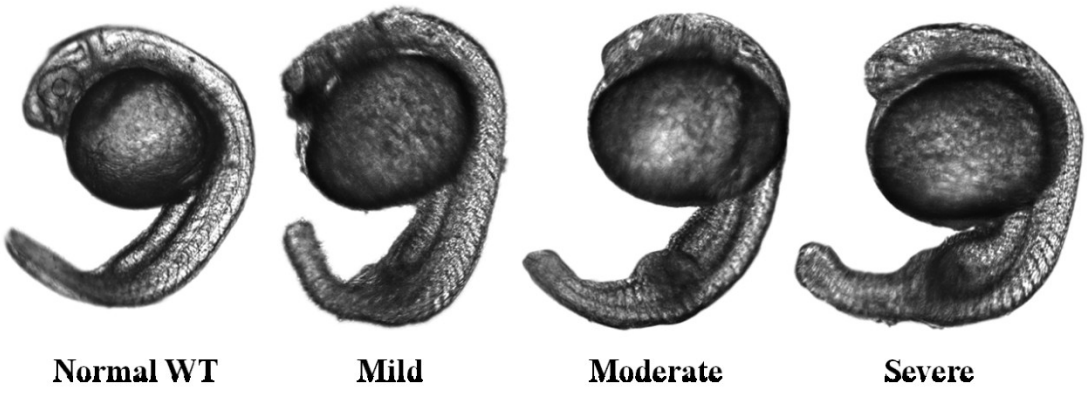

Figure 3-14. *chd*-MO knockdown phenotype

The no-*chordin* phenotype ranged from severe to mild where severe was identified by a significantly decreased head size, U-shaped somites, and a large blood island on the tail. Moderate and mild phenotypes were both identified by U-shaped somites and blood island, to varying degrees.

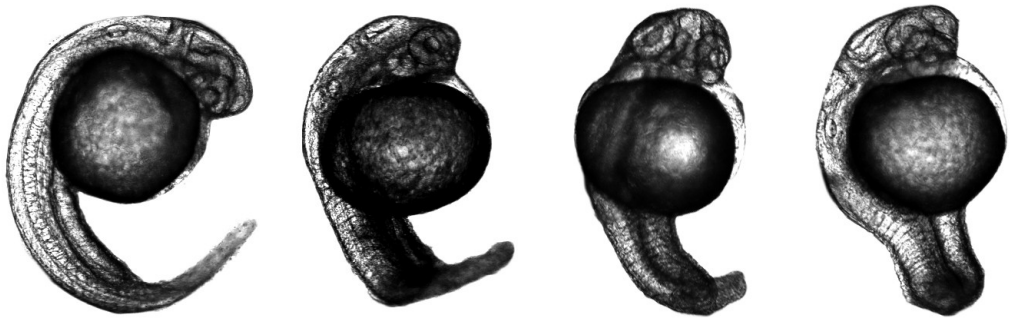

Normal WT (Class 1) **Class 2** **Class 3** **Class 4**

Figure 3-15. *ntl*-MO knockdown phenotype

Zebrafish embryos were injected at the 1-cell stage with 0.25 mM *ntl*-MO and imaged at 24 hpf. The *notail* morpholino knockdown phenotype ranged from severe (class 4) to mild (class 2) where severe is identified by a significantly decreased head size, U-shaped somites, no notochord, and no posterior structures. Class 3 is identified by U-shaped somites, no notochord, and significantly shortened posterior structures. Class 2 is identified by U-shaped somites, a shortened posterior axis, with the notochord still present.

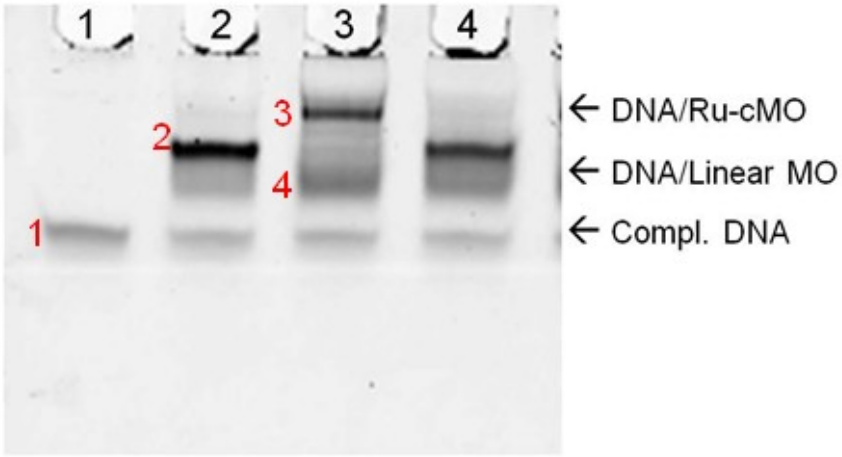

Figure 3-16. Gel-shift assay showing Ru-cMO formation and photolysis

15% native PAGE gel-shift assay showing formation of Ru-cMO-*chd* (lane 3), and subsequent photolysis with 450 nm light (14 mW/cm^2, 3 min) (lane 4). Complementary DNA and DNA/MO hybrid controls are show in lanes 1 and 2, respectively. Lane numbers are shown in black and band numbers are shown in red.

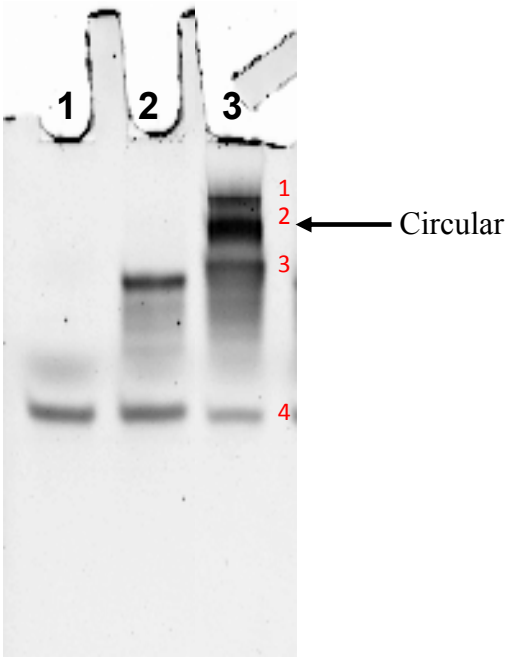

Figure 3-17. *ntl*-MO circularization

15% native PAGE gel-shift assay showing controls (lanes 1 and 2) and formation of Ru-cMO-*ntl* (lane 3). Circular product is indicated by the arrow. No additional purification was performed before *in vivo* testing. Due to initial impurities of bis-azido-*ntl* MO, the same circularization efficiency could not be achieved as with bis-azido-*chd* MO. Lane 1. complementary DNA, Lane 2. DNA: *ntl* MO hybrid, Lane 3. Click reaction 1.05:1 (MO: RuBEP), RT, 24 h. Lane numbers are shown in black and band numbers are shown in red. Band 4 represents complementary DNA, band 3 represents a singly clicked impurity as a result of initial N_3-MO impurity, band 2 represents Ru-cMO product, and band 1 represents dimerized product.

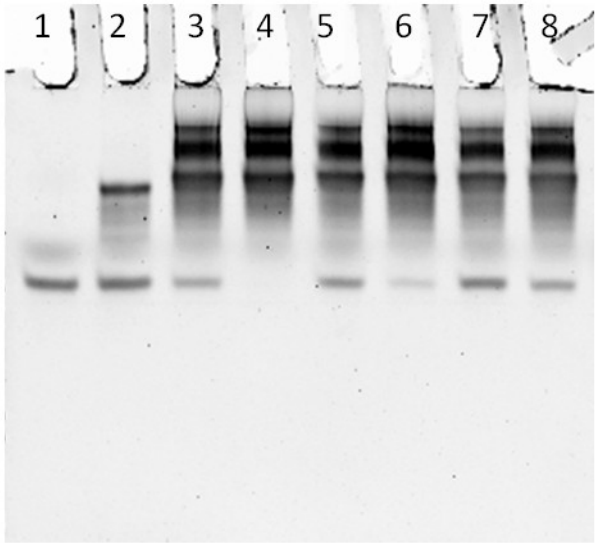

Figure 3-18. Time course gel-shift for Ru-cMO-*ntl*

15% native PAGE gel-shift assay showing controls (lanes 1 and 2) and formation of Ru-cMO-*ntl* (lanes 3-8). Circular product formation was monitored over a range of 15 min to 24 h. Lane 1: complementary DNA, lane 2: DNA/*ntl* MO hybrid, lane 3: 15 min rxn, lane 4: 30 min rxn, lane 5: 1 h rxn, lane 6: 6 h rxn, lane 7: 16 h rxn, lane 8: 24 h rxn. Band assignments are outlined in Figure 3-17.

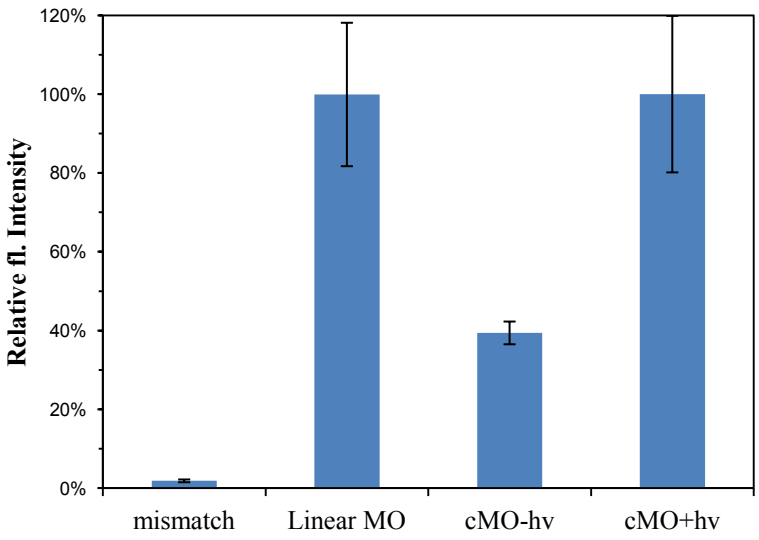

Figure 3-19. Molecular beacon assay showing Ru-cMO-*chd* caging

Molecular beacon fluorescence assay showing less probe hybridization to caged Ru-cMO compared to the linear MO or Ru-cMO after 3-min exposure to 450-nm light. Samples were annealed prior to molecular beacon assay to promote hybridization.

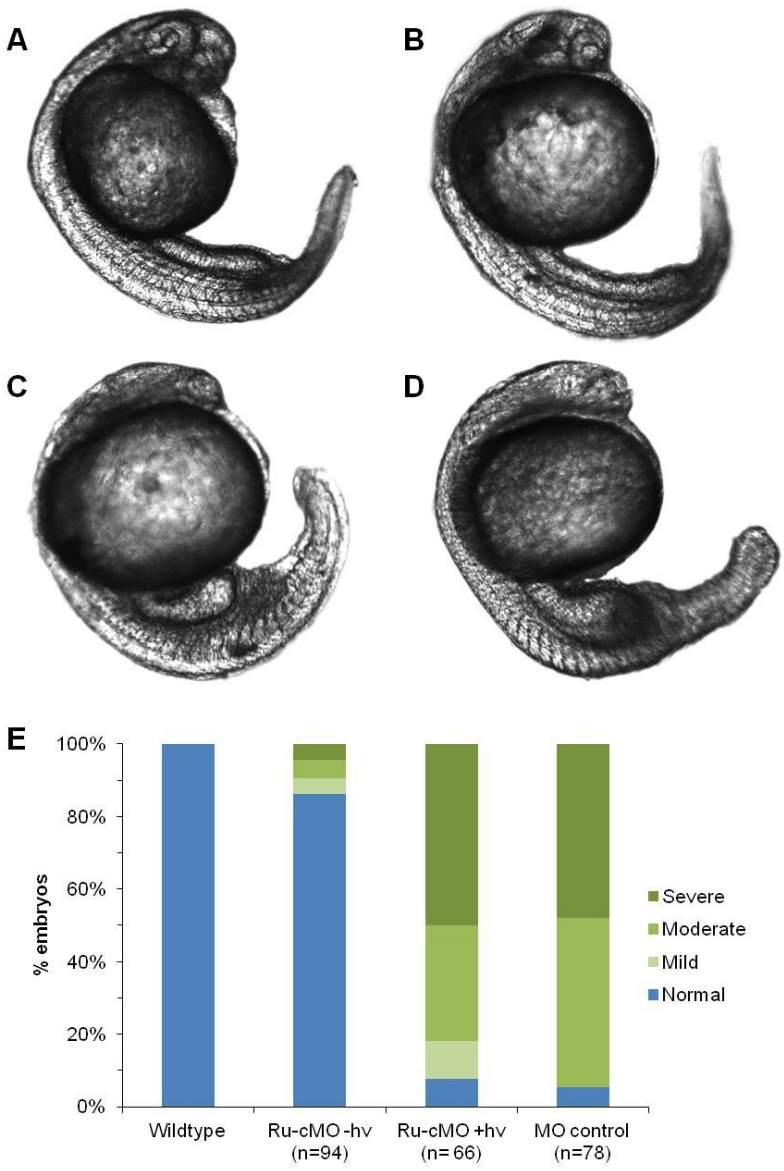

Figure 3-20. *in vivo* testing of Ru-cMO-*chd*

Representative images of 24-28 hpf zebrafish embryos, showing different degrees of *chd* knockdown phenotype: A) Wildtype control embryo, uninjected. B) Ru-cMO-*chd*, incubated in the dark, showing normal development. C) Ru-cMO-*chd*, irradiated for 5 min at 1 hpf with 450-nm light, showing no-chordin phenotype. D) Bis-azido morpholino control showing no-chordin phenotype. All embryos were injected at 1-cell stage. E) Percent of embryos showing each of four phenotypic responses.

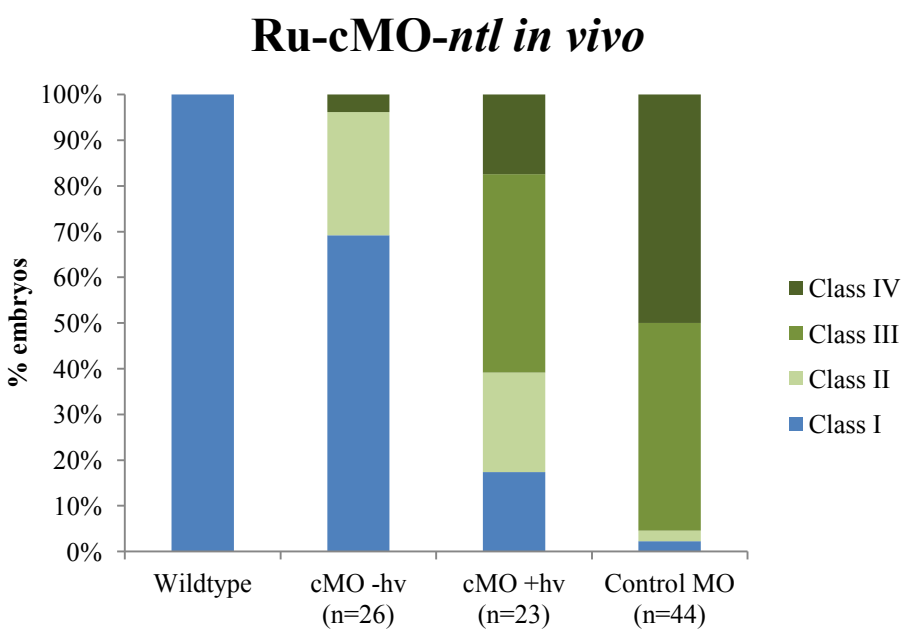

Figure 3-21. Ru-cMO-*ntl in vivo* data

Zebrafish embryos were injected with MO control at the 1-cell stage with 0.25 mM *ntl*-MO and imaged at 24 hpf. For Ru-cMO, zebrafish embryos were injected at the 1-cell stage with 0.25 mM Ru-cMO-*ntl*. Half of the embyros were irradiated (450 nm, 14 mW/cm^2, 5 min) at 1 hpf, while the other half were incubated in the dark. Embryos were scored for phenotype at 24 hpf.

Table 3-4. Phenotypic scoring for Ru-cMO-*chd in vivo*

	Wildtype	**Ru-cMO -hν**	**Ru-cMO +hν**	**MO control**
n value	>100	94	66	78
Normal	100.0%	86.2%	7.6%	5.3%
Mild	0.0%	4.3%	10.6%	0.0%
Moderate	0.0%	5.3%	31.8%	46.7%
Severe	0.0%	4.3%	50.0%	48.0%

Table 3-5. Phenotypic scoring for Ru-cMO-*ntl in vivo*

	Wildtype	**Ru-cMO -hν**	**Ru-cMO +hν**	**MO control**
n value	>100	26	23	44
Class I	100.0%	69.2%	17.4%	2.3%
Class II	0.0%	26.9%	21.7%	2.3%
Class III	0.0%	0.0%	43.5%	45.5%
Class IV	0.0%	3.8%	17.4%	50.0%

Table 3-6. Ru-cMO MALDI data.

Samples were analyzed using 3-hydroxypicolinic acid (3-HPA) matrix in linear positive ion mode on a Bruker Ultraflex III MALDI TOF/TOF mass spectrometer.

	Expected mass (Da)	**MALDI mass (Da)**
Ru-cMO-*chd*	9561	9567
Ru-cMO-*ntl*	9357	9385

Table 3-7. Oligonucleotide sequences, 5′ to 3′

DNA	GACTTGAGGCAGGCATATTTCCGAT
Reverse complement	ATCGGAAATATGCCTGCCTCAAGTC
Molecular beacon	6FAM-CCACCCATCGGAAATATGCCTGCCTCAAGTCGGGTGG-BHQ1
***chd*-MO**	ATCCACAGCAGCCCCTCCATCATCC
***chd* reverse complement**	GGATGATGGAGGGGCTGCTGTGGAT
***chd* molecular beacon**	6FAM-CGGGCGGGATGATGGAGGGGCTGCTGTGGATCGCCCG-BHQ1
ntl*-MO	AGCTTGAGATAAGTCCGACGATCCT
***ntl* reverse complement**	AGGATCGTCGGACTTATCTCAAGCT
DNA scramble	AAAAAAAAAAAAAAAAAAAAAAAA

IV. Conclusion

The first example of a ruthenium photolinker, RuBEP, was synthesized and characterized. RuBEP can be synthesized in high yields with a two-step synthesis. RuBEP undergoes ligand dissociation with a high quantum yield upon exposure to 450 nm light. This ligand exchange is very clean and efficient, making RuBEP an optimal photolinker for use in biological systems, and thus, RuBEP was used to cage DNA and MO oligonuclotides. The alkyne groups on the 3-ethynylpyridine ligands reacted with bis-azide-functionalized oligonucleotides to form cyclized, caged oligos in good yields and purity. These Ru-circularized oligos underwent efficient Ru^{2+}-ligand exchange upon 450-nm irradiation, to reveal the linear oligonucleotides. Ru-cMOs were tested *in vivo* and efficient caging of antisense activity was achieved when the oligo was circularized. Biological activity was restored upon 450 nm irradiation revealing the expected antisense knockdown phenotypes in zebrafish embryos. Complete restoration of biological activity confirmed that the pendant Ru^{2+} moiety did not adversely affect target hybridization or biological activity (Figure 3-20E). In addition to the broad *in vivo* applications for Ru-morpholinos, it is expected that RuBEP can be used to cage many other azide-functionalized biomolecules, e.g., peptides, lipids, oligosaccharides. Finally, the versatile 1-P and 2-P inorganic photochemistry of $[Ru(bipyridine)_2(X)_2]^{2+}$ complexes motivates further development of Ru photolinkers to allow multiplexed caging/uncaging for diverse applications.

V. References

(1) Boyden, E. S.; Zhang, F.; Bamberg, E.; Nagel, G.; Deisseroth, K. *Nat. Neurosci.* **2005**, *8*, 1263-1268.

(2) Young, D. D.; Deiters, A. *Org. Biomol. Chem.* **2007**, *5*, 999-1005.

(3) Salierno, M.; Fameli, C.; Etchenique, R. *Eur. J. Inorg. Chem.* **2008**, *2008*, 1125-1128.

(4) Gatterdam, V.; Ramadass, R.; Stoess, T.; Fichte, M. A. H.; Wachtveitl, J.; Heckel, A.; Tampé, R. *Angew. Chem., Int. Ed. Engl.* **2014**, *53*, 5680-5684.

(5) Ellis-Davies, G. C. R. *Beilstein J. Org. Chem.* **2013**, *9*, 64-73.

(6) Ellis-Davies, G. C. R. *Chem. Rev.* **2008**, *108*, 1603-1613.

(7) Eisen, J. S.; Smith, J. C. *Development (Cambridge, England)* **2008**, *135*, 1735-1743.

(8) Tang, X.; Maegawa, S.; Weinberg, E. S.; Dmochowski, I. J. *J. Am. Chem. Soc.* **2007**, *129*, 11000-11001.

(9) Tang, X.; Dmochowski, I. J. *Angew. Chem., Int. Ed. Engl.* **2006**, *45*, 3523-3526.

(10) Tang, X.; Dmochowski, I. J. *Molec. BioSyst.* **2007**, *3*, 100-110.

(11) Ouyang, X.; Shestopalov, I. A.; Sinha, S.; Zheng, G.; Pitt, C. L.; Li, W. H.; Olson, A. J.; Chen, J. K. *J. Am. Chem. Soc.* **2009**, *131*, 13255-13269.

(12) Shestopalov, I. A.; Sinha, S.; Chen, J. K. *Nat. Chem. Biol.* **2007**, *3*, 650-651.

(13) Shestopalov, I. A.; Chen, J. K. *Methods Cell Biol.* **2011**, *104*, 151-172.

(14) Deiters, A.; Garner, R. A.; Lusic, H.; Govan, J. M.; Dush, M.; Nascone-Yoder, N. M.; Yoder, J. A. *J. Am. Chem. Soc.* **2010**, *132*, 15644-15650.

(15) Yamazoe, S.; Shestopalov, I. A.; Provost, E.; Leach, S. D.; Chen, J. K. *Angew. Chem., Int. Ed. Engl.* **2012**, *51*, 6908-6911.

(16) Wang, Y.; Wu, L.; Wang, P.; Lv, C.; Yang, Z.; Tang, X. *Nucleic Acids Res.* **2012**, *40*, 11155-11162.

(17) Wu, L.; Wang, Y.; Wu, J.; Lv, C.; Wang, J.; Tang, X. *Nucleic Acids Res.* **2013**, *41*, 677-686.

(18) Ando, H.; Furuta, T.; Tsien, R. Y.; Okamoto, H. *Nat. Genet.* **2001**, *28*, 317-325.

(19) Pawley, J. B. *Handbook of Biological Confocal Microscopy*; 3rd ed.; Springer, 2006.

(20) Jayakumar, M. K. G.; Idris, N. M.; Zhang, Y. *Proc. Natl. Acad. Sci. U. S. A.* **2012**.

(21) Stoien, J. D.; Wang, R. J. *Proc. Natl. Acad. Sci. U. S. A.* **1974**, *71*, 3961-3965.

(22) Yamazoe, S.; Liu, Q.; McQuade, L. E.; Deiters, A.; Chen, J. K. *Angewandte Chemie International Edition* **2014**, n/a-n/a.

(23) Zayat, L.; Salierno, M.; Etchenique, R. *Inorg. Chem.* **2006**, *45*, 1728-1731.

(24) Sears, R. B.; Joyce, L. E.; Ojaimi, M.; Gallucci, J. C.; Thummel, R. P.; Turro, C. *J. Inorg. Biochem.* **2013**, *121*, 77-87.

(25) Zayat, L.; Calero, C.; Albores, P.; Baraldo, L.; Etchenique, R. *J. Am. Chem. Soc.* **2003**, *125*, 882-883.

(26) Garner, R. N.; Joyce, L. E.; Turro, C. *Inorg. Chem.* **2011**, *50*, 4384-4391.

(27) Zayat, L.; Filevich, O.; Baraldo, L. M.; Etchenique, R. *Philos. Trans. A Math Phys. Eng. Sci.* **2013**, *371*, 20120330.

(28) Filevich, O.; Etchenique, R. *Photochem. Photobiol. Sci.* **2013**, *12*, 1565-1570.

(29) Fino, E.; Araya, R.; Peterka, D. S.; Salierno, M.; Etchenique, R.; Yuste, R. *Front. Neural Circuits* **2009**, *3*.

(30) Filevich, O.; Salierno, M.; Etchenique, R. *J. Inorg. Biochem.* **2010**, *104*, 1248-1251.

(31) Salierno, M.; Marceca, E.; Peterka, D. S.; Yuste, R.; Etchenique, R. *J. Inorg. Biochem.* **2010**, *104*, 418-422.

(32) Rial Verde, E. M.; Zayat, L.; Etchenique, R.; Yuste, R. *Front. Neural Circuits* **2008**, *2*, 2.

(33) Tornoe, C. W.; Christensen, C.; Meldal, M. *J. Org. Chem.* **2002**, *67*, 3057-3064.

(34) Rostovtsev, V. V.; Green, L. G.; Fokin, V. V.; Sharpless, K. B. *Angew. Chem., Int. Ed. Engl.* **2002**, *41*, 2596-2599.

(35) Bryant, J. R.; Mayer, J. M. *J. Am. Chem. Soc.* **2003**, *125*, 10351-10361.

(36) Furuta, T.; Wang, S. S.-H.; Dantzker, J. L.; Dore, T. M.; Bybee, W. J.; Callaway, E. M.; Denk, W.; Tsien, R. Y. *Proc. Natl. Acad. Sci. U. S. A.* **1999**, *96*, 1193-1200.

(37) Nasevicius, A.; Ekker, S. C. *Nat Genet.* **2000**, *26*, 216-220.

(38) Westerfield, M. *The Zebrafish Book. A Guide for the Laboratory Use of Zebrafish (Danio rerio)*; 4th Edition ed.; University of Oregon Press, 2000.

(39) Tallafuss, A.; Gibson, D.; Morcos, P.; Li, Y.; Seredick, S.; Eisen, J.; Washbourne, P. *Development (Cambridge, England)* **2012**, *139*, 1691-1699.

Chapter 4

Caging metal ions with light-responsive nano-polymersomes

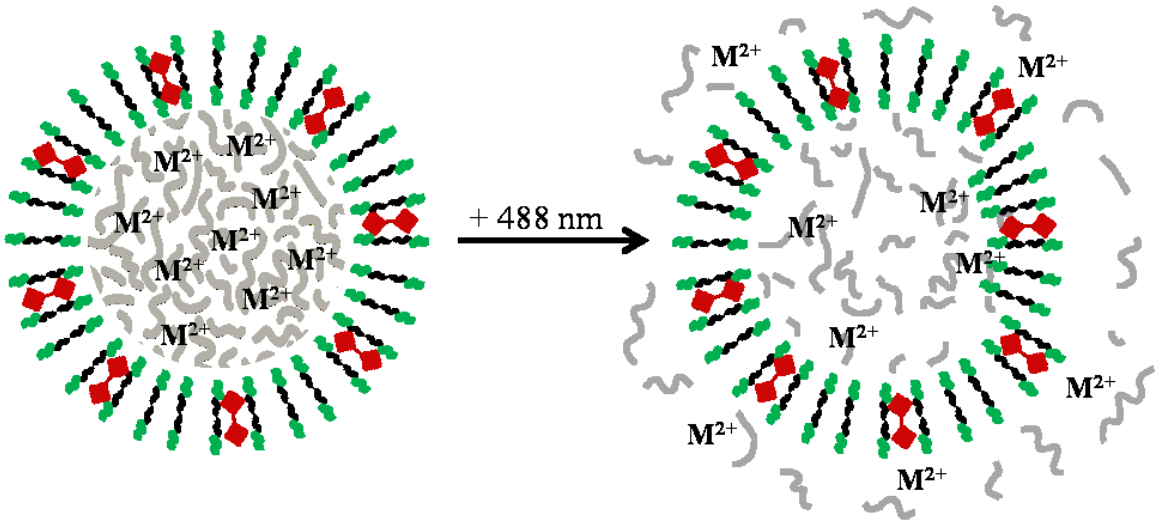

This chapter is adapted from a submitted manuscript.

Julianne C. Griepenburg,[‡ a] Nimil Sood,[‡b] Kevin Vargo,[b] Dewight Williams,[c] Jeff Rawson,[d] Michael J. Therien,[d] Daniel A. Hammer,[b,e] Ivan J. Dmochowski*[,a]

[a]Department of Chemistry, University of Pennsylvania,
231 South 34th Street, Philadelphia, PA 19104
[b]Department of Chemical and Biomolecular Engineering, University of Pennsylvania, 220 South 33rd Street, Philadelphia, PA 19104
[c]Department of Biochemistry and Biophysics, Perelman School of Medicine, University of Pennsylvania, 3700 Hamilton Walk, Philadelphia, PA 19104
[d]Department of Chemistry, Duke University,
124 Science Drive, Durham, NC 27708
[e]Department of Bioengineering, University of Pennsylvania,
210 South 33rd Street, 240 Skirkanich Hall, Philadelphia, PA 19104

J. C. Griepenburg and N. Sood contributed equally to this work.
K. Vargo and D. Williams performed cryo-TEM.
J. Rawson synthesized PZn_2.
M. J. Therien, D. A. Hammer, and I. J. Dmochowski are funding authors.

I. Introduction

The caging and precise spatiotemporal release of bio-active compounds is becoming increasingly important in the field of nanomedicine. A particular focus has been the development of chemical cages for metal ions, such as Zn^{2+} and Ca^{2+}. Zinc is required for normal cell function and important for both intracellular and extracellular signaling. Lack of zinc homeostasis can retard growth and lead to immunodeficiency.[1-3] The biological importance of Ca^{2+} has been studied extensively in muscle contraction, cell signaling, gene regulation, thrombosis, wound healing, and cell death.[4] Deficiencies in zinc and calcium are common in the human population, and can lead to many neurological, cardiovascular, and endocrine disorders.[4,5] Strategies for further probing the biological functions of these metal ions involve metal ion delivery to localized sites, which has the advantage of avoiding homeostatic disruption in non-target areas.

Traditional approaches for caging metal ions have employed inorganic coordination chemistry, where one or more multivalent ligands coordinates the metal ion, and the release of the caged ion is achieved by modulating the dissociation constant, K_D, for the ligand-metal ion complex. A family of ligands has been developed for Zn^{2+} and Ca^{2+} with weak and strong affinities.[4,6-8] A common challenge with small-molecule ligands is the lack of specificity where similar ions can compete for binding to the active site.[8] An extension of the thermodynamically-driven release of metal ions is incorporation of stimulus responsiveness. Light has been used in conjunction with coordination chemistry to provide a binary system that switches from caged to uncaged

for both Zn^{2+} and Ca^{2+}. In these systems, photoactive moieties such as *o*-nitrobenzyl, fluoroionophores, and nitrodibenzofurans, were used for Zn^{2+} and Ca^{2+} caging.[9-13] These systems, however, require high doses of near-UV light for uncaging, which limits biological compatibility and depth penetration in biological systems. Light penetration into tissue can be improved with longer wavelengths or 2-photon excitation. However, there are limited examples of caging metal ions with visible or NIR light. One example by Canto *et al*. used spiropyran receptors conjugated to single-wall nanotubes (SWNTs) for the reversible trapping and release of Zn^{2+} with visible light.[14]

Encapsulation within stimulus-responsive nanocarriers is a more generalizable approach to metal ion caging/release compared to molecularly caged systems. The release no longer depends on the ligand chemistry, enabling the same nanocarrier to be used for a variety of different metal ion systems, or even to deliver multiple metal ions simultaneously. Another advantage of nanocarriers over molecular cages is that the number of metal ions that can be caged is not limited by the valency of the chelator. One versatile class of nanocarriers is polymersomes, which are self-assembled bilayer vesicles synthesized from amphiphilic diblock copolymers.[15,16] They provide a large internal aqueous environment for hydrophilic encapsulation and a hyperthick membrane for hydrophobic encapsulation, and can be surface modified to provide targeting capabilities.[17-22]

The work presented here specifically utilizes photoresponsive nanoscale polymersomes for the encapsulation and delivery of metal ions with a visible light

trigger. Previous examples of photoresponsive nano-polymersomes were limited to incorporation of UV-active moieties within the diblock copolymer. Cabane *et al*. presented a UV-responsive nano-polymersome containing an *o*-nitrobenzyl moiety between the hydrophobic and hydrophilic polymer blocks, used to encapsulate and release small molecular weight dyes and proteins.[23] There are examples of other types of nanocarriers that can be made photoresponsive such as micelles with embedded 2 photon active photoswitches, reported by Zhang *et al*.[24]

Previous work done in our laboratory has shown that micron-scale polymersomes synthesized from poly(ethylene oxide)-poly(butadiene) (OB29, MW = 3800 g/mol) can be made photoresponsive through the addition of dextran in the aqueous core and meso-to-meso ethyne-bridged (porphinato)zinc(II) dimer, PZn_2, in the hydrophobic membrane. These vesicles undergo membrane deformation upon irradiation with visible light, as the incorporate PZn_2 is an effective chromophore in the visible to near-IR region.[17,25,26] Here, we present the extension of this work from micron-scale vesicles to vesicles that are 100 to 200 nanometers in diameter, a size regime amenable to the use of this system in biological applications. Additionally, we demonstrate the ability to tune photoresponsiveness of the system with visible light wavelength, irradiation time, and the presence of dextran in the core. The system presented here shows efficient encapsulation and release of a small molecule, fluorescein isothiocyanate (FITC), and two biologically relevant metal ions, Zn^{2+} and Ca^{2+}. This work is the first report of nano-polymersomes for the encapsulation of metal ions and release with visible light.

II. Experimental procedures

A. Self-assembly of micron-scale polymersomes

Micron-sized polymersomes were synthesized via a thin-film rehydration method.[26] Briefly, OB29 polymer solution (200 μL, 1 mM) in methylene chloride was deposited onto the surface of a roughened Teflon square. The film was placed in a glass vial and allowed to dry for 16-24 h to evaporate of the organic solvent. An aqueous buffer (2 mL) containing the hydrophilic encapsulant in 290 mOsm sucrose was added to the glass vial, submerging the polymer film entirely in the buffer. The glass vial was capped and placed in a 60 °C oven for 12-16 h. After heating, the glass vial was rapidly vortexed for 1 min to yield micron-sized polymersomes.

B. Self-assembly of nanoscale polymersomes

Nanoscale polymersomes were made by direct injection of aqueous buffer into a solution of DMSO containing polyethylene oxide–polybutadiene (PEO_{30}–PBD_{46}, denoted OB29, MW = 3800 g/mol). The final mixture contained 30% DMSO by volume. The DMSO-buffer mixture was immediately vortexed for 5 min to promote vesicle self-assembly. Vesicle size and monodispersity were tuned through polymer concentration, aqueous-to-organic volume ratio, and vortex time. To make light-responsive nano-polymersomes, a 10 mol% solution of PZn_2 (2123 g/mol) was added to the DMSO

solution prior to vortexing. Dextran (10 kDa) was added to the aqueous buffer to make a 10 mg/mL solution.

C. Encapsulation and purification

For micron-sized vesicles, hydrophilic encapsulants (fluorescently labeled oligonucleotides, 5 nmol) were added to the sucrose hydration solution prior to the vortexing. The polymersomes were purified to remove unencapsulated dextran and fluorescently labeled oligonucleotide by centrifugation in a density step gradient. Before centrifugation, the top layer contained the polymersome sample diluted in isosmotic PBS and the bottom layer contained a solution of sucrose and density gradient medium (80% sucrose/20% Optiprep by volume). The sample was spun at 10,000 RPM for 1 h at 4 ºC. The polymersomes migrated to the PBS and sucrose/Optiprep interface and were retrieved with a syringe. The polymersome sample was dialyzed against isosmotic PBS (overnight, 4 ºC) to remove any remaining dextran, unencapsulated oligonucleotides, and Optiprep in 50 kDa dialysis tubes (Thermo Scientific, Rockford, IL).

For nanoscale vesicles, hydrophilic encapsulants (dextran and oligo, FITC, or metal ions) were added to the aqueous buffer prior to solvent injection and vortexing. Fluorescein labeled morpholino (Fl-MO) loaded vesicles were synthesized by adding 5 nmol fl-MO to the 290 mOsm PBS hydration buffer. FITC-loaded vesicles were synthesized with a saturated solution of FITC in 290 mOsm PBS. Ca^{2+}-loaded vesicles were synthesized with 150 mM $CaCl_2$, and Zn^{2+}-loaded vesicles were synthesized with

150 mM $ZnSO_4$. After vortexing, vesicles were dialyzed against the corresponding buffer of equal osmolarity using a 50 kDa molecular weight cutoff dialysis cassette to remove free 10 kDa dextran and unencapsulated hydrophilic cargo. Metal ion samples were dialyzed against isosmotic NaCl for two days at 4 °C with at least two buffer changes. An additional separation step was performed on samples that would be used for release studies to ensure that all free encapsulant was removed. A 50 kDa molecular weight cutoff Amicon Ultra centrifugal filter was used to separate any remaining free hydrophilic encapsulant from the nanovesicles. The vesicles were spun at 10,000 rpm to concentrate, and resuspended in buffer for further washes. This process was repeated until free encapsulant could no longer be detected in the filtrate via UV/Vis absorbance. A representative UV/Vis (Figure 4-1) shows the removal of unencapsulated oligonucleotide with an Amicon centrifugal filter. The Abs_{260} measured in the flow-through decreases with increasing number of spin/wash cycles.

D. Dynamic light scattering measurements

Polymersome size distribution was measured using a Malvern NanoZS Zetasizer. Polymersome samples were diluted 10-fold in the corresponding aqueous buffer in 1 mL polystyrene cuvettes. Size is reported as intensity %.

E. Cryo-TEM measurements

Krishna P. Singh Center for Nantechnology: Lacey formvar/carbon grids (Ted Pella) were cleaned with chloroform to remove the formvar coating, carbon coated with a Quorum Q150 ES carbon coater (Quorum Technologies, UK), and cleaned with hydrogen/oxygen plasma for 15 seconds using a Solarus Advanced Plasma System 950 (Gatan, Pleasanton, CA). The polymersome sample (2 μL) was deposited onto the grid and inserted into a cryoplunger (Cp3, Gatan). The sample was blotted by hand with filter paper and plunged into liquid ethane. The samples were subsequently transferred to a Gatan CT3500TR cryoholder and inserted quickly into a JEOL 2100 HRTEM (JEOL, Tokyo, Japan) operating at 200 kV. Images were captured using an Orius SC200 digital camera.

Electron Microscopy Resource Laboratory: Lacy carbon grids were glow discharged for 20 seconds at 25 mA to create a hydrophilic surface. A volume of 3 microliters of polymersome sample was applied and a thin film was formed by blotting the grid with filter paper. Vitreous ice was formed by rapid plunging into liquid ethane cooled to -180 °C by liquid nitrogen. Frozen hydrated samples were observed at -178 °C in a FEI (Hillsboro, OR.) Tecnai-12 microscope operated at 80 keV at magnifications indicated in the figure legends. Images were recorded on a Gatan (Warrendale, PA) US 1000 2048² CCD camera. All particle measurements were performed in Digital Micrograph.

F. Cargo release from polymersomes

Light-responsive polymersomes (30 μL) were irradiated in a PDMS well placed on a 0.17-micron thick glass coverslip. An Olympus FV1000 confocal laser scanning microscope equipped with multiple visible laser lines (488, 515, 543, 633 nm) was used for irradiation. The sample was centered within the field of view of a 10x air objective (Olympus UPlanSApo, NA = 0.40) lens, and subsequently irradiated for 1, 2, 5, or 10 min without sample evaporation occurring. Positive control release (100% release) was achieved through the addition of a surfactant, Triton-X 100, to a final concentration of 0.1 vol%. Negative control samples (0% release) were kept at constant osmotic strength and were not irradiated.

G. Detection of cargo release from nano-polymersomes

Fluorescent oligonucleotide (Fl-MO): After irradiation, 25 μL of sample was removed from the PDMS well and placed into the filter of a 50 kDa molecular weight cutoff Amicon Ultra 0.5 mL centrifugal filter. PBS (100 mM, 75 μL) was added to the filter. The sample was centrifuged for 15 min at 10,000 rpm so that the released oligonucleotide (6,000 - 10,000 Da) would flow through the filter but all vesicles (intact or ruptured) and encapsulated oligonucleotide would remain in the filter. The flow-through was collected and analyzed for fluorescence using a Cary Eclipse Fluorescence spectrophotometer. The sample was placed in a small volume quartz cuvette (40 μL) and excited at 494 nm. The emission spectrum was collected from 504 - 650 nm, and

fluorescence intensity at 517 nm was used to calculate oligonucleotide release. Positive and negative control vesicles were subjected to the same conditions.

Fluorescein isothiocyanate (FITC): After irradiation, 25 μL of sample was removed from the PDMS well and placed into the filter of a 50 kDa molecular weight cutoff Amicon Ultra 0.5 mL centrifugal filter. PBS (100 mM, 75 μL) was added to the filter. The sample was centrifuged for 15 min at 10,000 rpm so that the released FITC dye (MW = 389.4 g/mol) would flow through the filter but all vesicles (intact or ruptured) and encapsulated dye would remain in the filter. The flow-through was collected and analyzed for fluorescence using a Cary Eclipse Fluorescence spectrophotometer. The sample was placed in a small volume quartz cuvette (40 μL) and excited at 494 nm. The emission spectrum was collected from 504 - 650 nm, and fluorescence intensity at 517 nm was used to calculate FITC release. Positive and negative control vesicles were subjected to the same conditions.

Ca^{2+}: After irradiation, 6.25 μL of sample was removed from the PDMS well and placed in a small volume quartz cuvette. A stock solution of Oregon Green 488 BAPTA-1 hexapotassium salt in water was prepared to 1 μM. Oregon green stock solution (5 μL) was added to the cuvette, and the Oregon Green/polymersome mixture was diluted 128-fold. The sample was excited at 495 nm and the emission spectrum was collected from 505 to 650 nm. The fluorescence intensity at 523 nm was used to calculate Ca^{2+} release. Positive control vesicles were achieved with the addition of Triton-X 100. Polymersome sample (6.25 μL) was added to a small volume cuvette and Triton-X 100 was added to

achieve a final concentration of 0.1% v/v. This sample was then diluted 128-fold, and analyzed for fluorescence intensity. Negative control vesicles were also diluted 128-fold and analyzed for fluorescence intensity, without additional light or surfactant treatment.

Zn^{2+}: After irradiation, 20 μL of sample was removed from the PDMS well, placed into the filter of a 50 kDa molecular weight cutoff Amicon Ultra 0.5 mL centrifugal filter, and diluted to 90 μL. The sample was centrifuged for 15 min and 10,000 rpm so that the released Zn^{2+} flowed through the filter but all vesicles (intact or ruptured) and encapsulated metal ions remained in the filter. The flow-through was collected and analyzed for fluorescence using a Cary Eclipse Fluorescence spectrophotometer. The sample was placed in a small volume quartz cuvette (40 μL) and 5 μL of Oregon Green dye was added. The sample was excited at 495 nm and the emission spectrum was collected from 505 to 650 nm, and fluorescence intensity at 523 nm was used to calculate Zn^{2+} release. For positive control vesicles, Triton-X 100 was added to the sample before filtering, to a final concentration of 0.1% v/v. Negative control vesicles were untreated, but also spun in centrifugal filters.

H. Microinjection into zebrafish embryos

Nano-polymersomes were concentrated in a 10 kDa molecular weight cutoff Amicon centrifugal filter. Sample volume was concentrated 4-fold from the original sample and used for injections with no additional preparation. Zebrafish embryos were obtained from the CDB Zebrafish Core Facilty at the University of Pennsylvania

Perelman School of Medicine. All embryos obtained were TLF x TLF (WT). All injections were performed at the one-cell stage and injected into the cell compartment only. A Harvard Apparatus PLI-100 pico-injector was used to inject controlled volumes. Injection volume was calibrated to dispense 10 nL per embryo. Embryos were imaged with an Olympus FV1000 laser scanning confocal microscope using transmitted light imaging, as well as imaged for PZn_2. A 10x air objective (Olympus UPlanSApo, NA = 0.40) was used for single embryo imaging and 4x air objective (Olympus UPlanSApo, NA = 0.16) was used for multiple embryo imaging.

I. Porphyrin dimer (PZn_2) wavelength shift determination

A CRi Multispectral Imaging System, NuanceFX camera attached to an Olympus IX81 inverted microscope, was used for measurement of PZn_2 emission spectrum before and after irradiation. Epi-fluorescence illumination was used for PZn_2 excitation with a mercury-arc lamp and 530–550 nm band-pass filter. A three-dimensional image cube measuring PZn_2 emission from 660–720 nm in 3-nm steps was collected by the camera through a 10x air objective (Olympus UPlanSApo, NA = 0.40). The PZn_2 emission spectrum was determined for select regions of interest using the Nuance 2.10 real component analysis software.

J. Materials

PEO_{30}–PBD_{46} (OB29) was purchased from Polymer Source (Quebec, Canada). Oregon Green 488 BAPTA-1 hexapotassium salt was purchased from Life Technologies (Grand Island, NY). PBS (10x), DMSO (ACS reagent grade), $CaCl_2$ (dihydrate), $ZnSO_4$ (heptahydrate), and Slide-a-lyzer G2 dialysis cassettes, were purchased from Fisher Scientific (Pittsburgh, PA). Amicon Ultra centrifugal filters were purchased from Millipore (Billerica, MA).

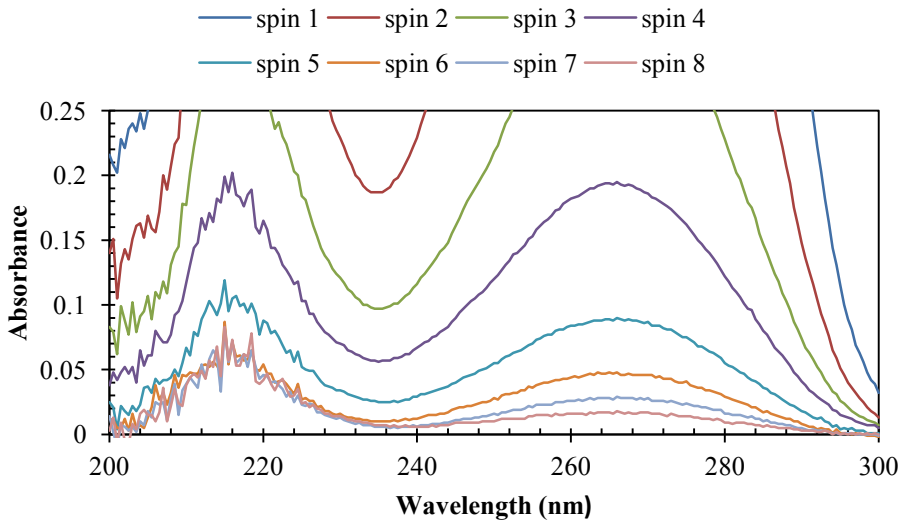

Figure 4-1. Abs_{260} measurement of Amicon flow-through for vesicle purification

Nanovesicles containing oligonucleotide were separated from free-oligonucleotide with an Amicon centrifugal filter. The flow-through for each spin/wash cycle was measured for Abs_{260} until free oligonucleotide was no longer detectable.

III. Results and discussion

A. Thin film self-assembly vs. Direct injection

A standard method of vesicle self assembly to maximize vesicle yield and monodispersity was developed. To yield micron-sized vesicles, 1 mM of polymer was cast onto a thin teflon film, incubated with the aqueous hydration solution, and vortexed to promote self-assembly.[26] To yield nano-vesicles through this same method, self-assembly is initiated through sonicating instead of vortexing. Although this method generated fairly monodisperse vesicles, the yield of vesicles was limited due to the amount of polymer that could be dried on the Teflon film. The concentration of polymer for the system was limited to 1 mM to achieve a smooth film.

To allow for higher concentrations of polymer to maximize nano-polymersome yield, a different method of self-assembly was investigated where a solution of polymer in DMSO was directly mixed into buffer. This direct injection method has many benefits over the thin-film method of self assembly. Primarily, this method allows for the incorporation of higher polymer concentrations, limited only by the solubility of the polymer in DMSO. By increasing the polymer concentration, the nanovesicle yield was significantly increased. Additionally, the polymer drying and hydration solution incubation steps were eliminated, shortening the vesicle preparation process. To achieve the maximum yield of vesicles, while preserving vesicle shape, size, and monodispersity, a variety of different self-assembly conditions were tested.

B. Effect of mixing, aqueous-to-organic ratio, and polymer concentration on self-assembly of nanoscale polymersomes

The effect of mixing was explored first for the direct injection self-assembly method. For the initial screening, no hydrophobic encapsulants (PZn_2) or hydrophilic encapsulants (dextran, cargo) were included in vesicle preparation. The vesicles were characterized dynamic light scattering (DLS), and cryo-TEM. Three methods of mixing were tested for their effect on vesicle size and monodispersity: stirring, sonicating, and vortexing. The first conditions tested were sonicating vs. stirring during the direct injection process. For stirred samples, a micro stir bar was placed into a 2 mL glass vial and placed on a magnetic stir plate. The organic (OB29 in DMSO) solution was injected into the aqueous solution (0.1 M PBS) while stirring. For sonicated samples, the organic solution was injected into the aqueous solution in a 2 mL glass vial while sonicating. Both samples were infused at a rate of 10 μL/min. The samples were dialyzed to remove the DMSO and both samples were characterized by DLS and cryo-TEM. A comparison of the two samples is shown in Figure 4-2. Stirring resulted in uniform particles, however, the average size of 60 nm is too small for the encapsulation of biomolecules, and not ideal for *in vivo* applications. Although DLS was promising for the sonicated sample, showing an average size of 150 nm, cryo-TEM showed a significant amount of complex, non-vesicular structures. The aqueous infusion rate was varied between slow infusion (10 μL/min) and direct injection, and no difference was observed on DLS or cryo-TEM. Direct injection was used for subsequent samples.

Vortexing was also explored as a method promoting self-assembly. Four different vortex durations (1, 5, 10, and 20 min) were tested for two different concentrations of polymer. A 1 mM solution of OB29 in DMSO was directly injected into PBS in a glass vial. The vial was immediately capped and each sample was continuously vortexed. The same series of samples were also made for 3 mM OB29 in DMSO. The samples were dialyzed to remove DMSO and then analyzed by DLS. A clear trend was seen for both polymer concentrations as shown in Figure 4-3. After 1 min of vortexing there were two peaks, likely representing both micelles, and unassembled polymer. As vortex time increased these peaks converged to one peak centered around 100 nm. There was no significant change after 5 min, indicating that the self-assembly process was complete. These samples were also analyzed by cryo-TEM (Figure 4-4) to determine the effect of vortex time on morphology. Consistent with DLS, the 1 min vortex sample showed a significant amount of micelle formation. The 5, 10, and 20 min vortexed samples showed unilamellar, monodisperse vesicles, with very limited presence of non-vesicular structures.

Another variable in the direct injection self-assembly process was the ratio of organic-to-aqueous solvent. Previous samples were made with 30% v/v DMSO in buffer. This percent was varied from 10, 30, 50, and 70% for four different polymer concentrations in DMSO. The vesicles were dialyzed to remove DMSO and analyzed with DLS and cryo-TEM. Figure 4-5 shows the negligible effect that the organic-to-aqueous ratio had on vesicle size determined by DLS for 1, 1.5, 2, and 3 mM OB29

concentrations. However, when these samples were visualized by cryo-TEM (Figure 4-6) a very significant difference in morphology was seen. Although unilamellar vesicles were present in all samples, 10% and 70% DMSO had a large amount of non-vesicular structures, such as worms and micelles. The 30% and 50% DMSO samples both yielded a large amount of uniform, unilamellar vesicles of the desired size. Because DMSO removal is necessary for biological applications, 30% DMSO was a better choice for this system.

The effect of concentration on vesicle size was also explored. Figure 4- shows a slight difference in vesicle size between 1, 1.5, 2, and 3 mM OB29 in 30% DMSO. Vesicles prepared with 1 mM and 3 mM OB29 resulted in slightly smaller vesicles. Vesicles prepared with 1.5 mM and 2 mM OB29 resulted in vesicles of a more desirable size, making these concentrations a reasonable choice for vesicle preparation.

Thorough self-assembly characterization resulted in the following optimized vesicle preparation conditions: Direct-solvent injection of 30% DMSO containing 1.5 - 2 mM OB29 into 0.1M PBS, immediately capped and vortexed for 5 min, followed by dialysis to remove DMSO. To make these vesicles light-responsive, 10 mol% PZn_2 was added to the polymer in DMSO solution. These vesicles were dialyzed and imaged with cryo-TEM to confirm the desired morphology and size with the addition of a hydrophobic encapsulant. Figure 4-8 shows vesicle size and morphology using the optimized conditions.

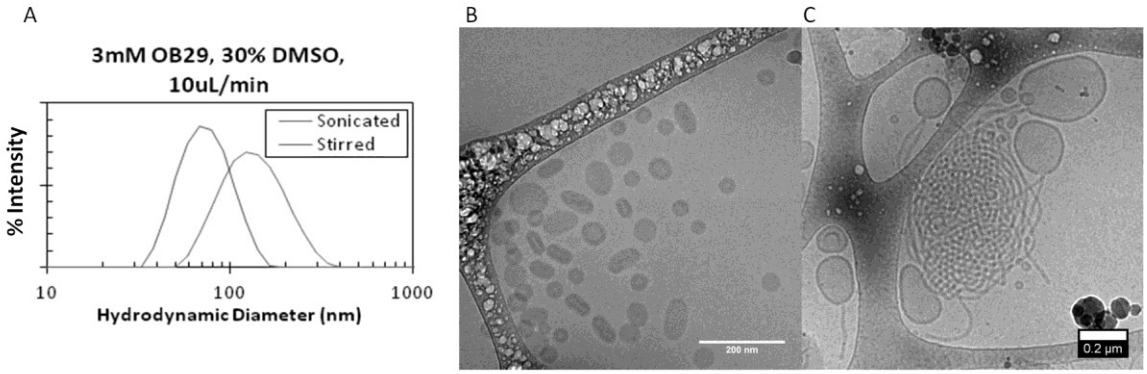

Figure 4-2. Effect of stirring vs. sonicating during nanovesicle self-assembly

A comparison of nanovesicles prepared with stirring vs. sonicating. Stirred samples resulted in uniform vesicles < 100 nm in diameter. Sonicated samples resulted in larger vesicles and asignificant amount of non-vesicular wormlike structures.

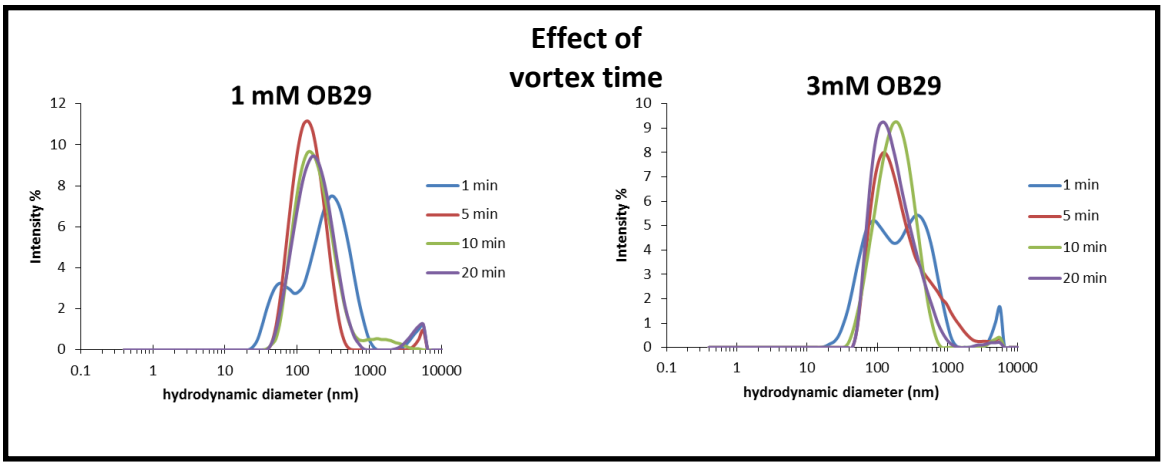

Figure 4-3. Effect of vortex time on nano-vesicle size

DLS showing the effect of vortex time on vesicle size. Vesicles were prepared by directly injecting OB29 in 30% DMSO into 0.1 M PBS followed by immediate vortexing. Vesicle size converged by 5 min for both concentrations.

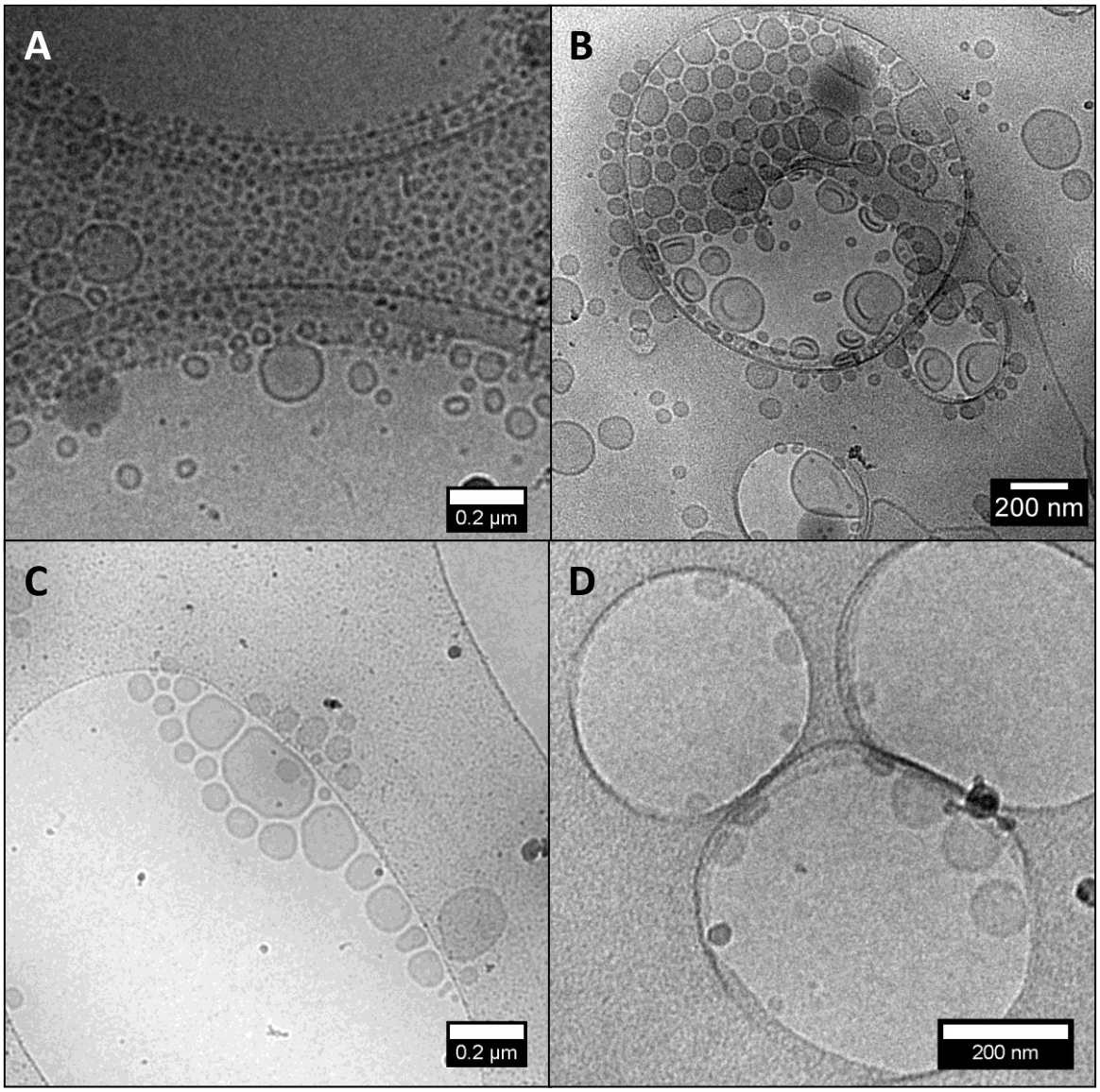

Figure 4-4. Effect of vortex time on nano-vesicle morphology

Cryo-TEM images showing the effect of vortex time on vesicle morphology. Vesicles were prepared by directly injecting OB29 in 30% DMSO into 0.1 M PBS followed by immediate vortexing. A) 1-min vortexing resulted in a large number of micelles. B) 5-min vortexing resulted in uniform, unilamellar vesicles. C, D) 10-min and 20-min vortexing showed no significant change from 5 min.

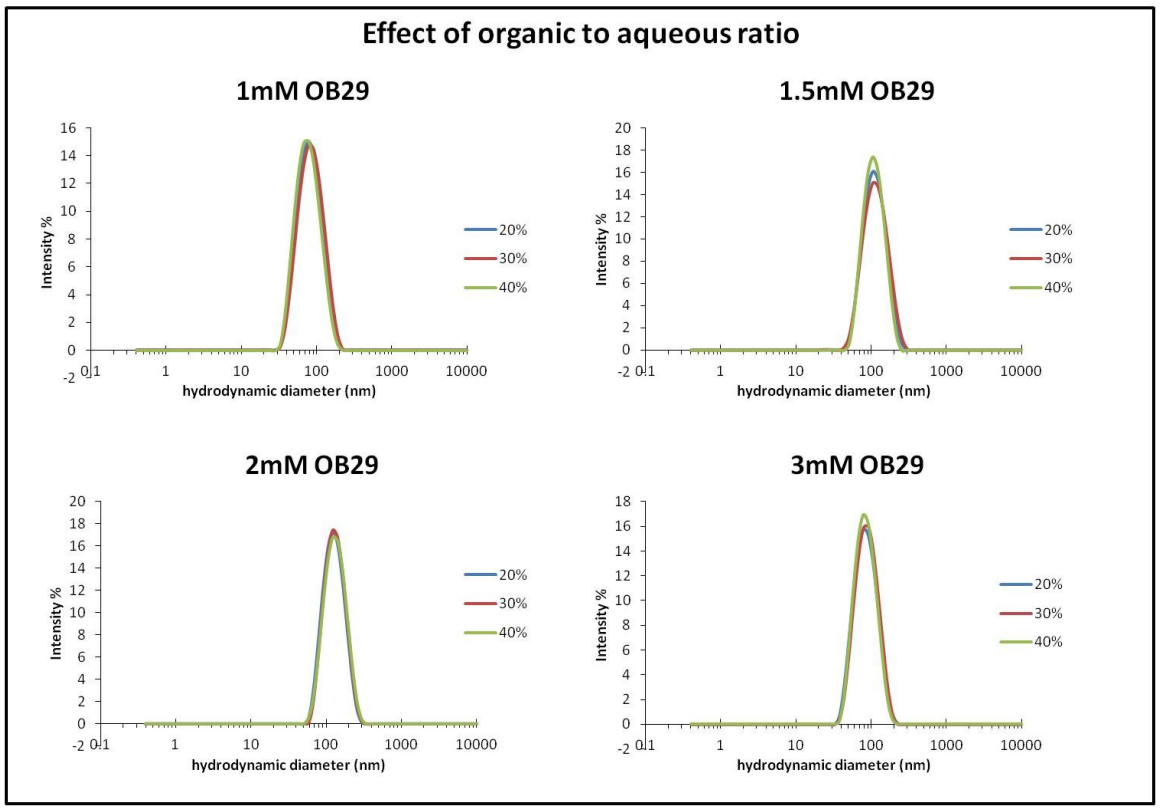

Figure 4-5. Effect of organic to aqueous ratio on nano-vesicle size

DLS measurements showing no significant effect on organic (OB29 in DMSO) to aqueous (0.1 M PBS) ratio. Legend % represents percent DMSO in final solution.

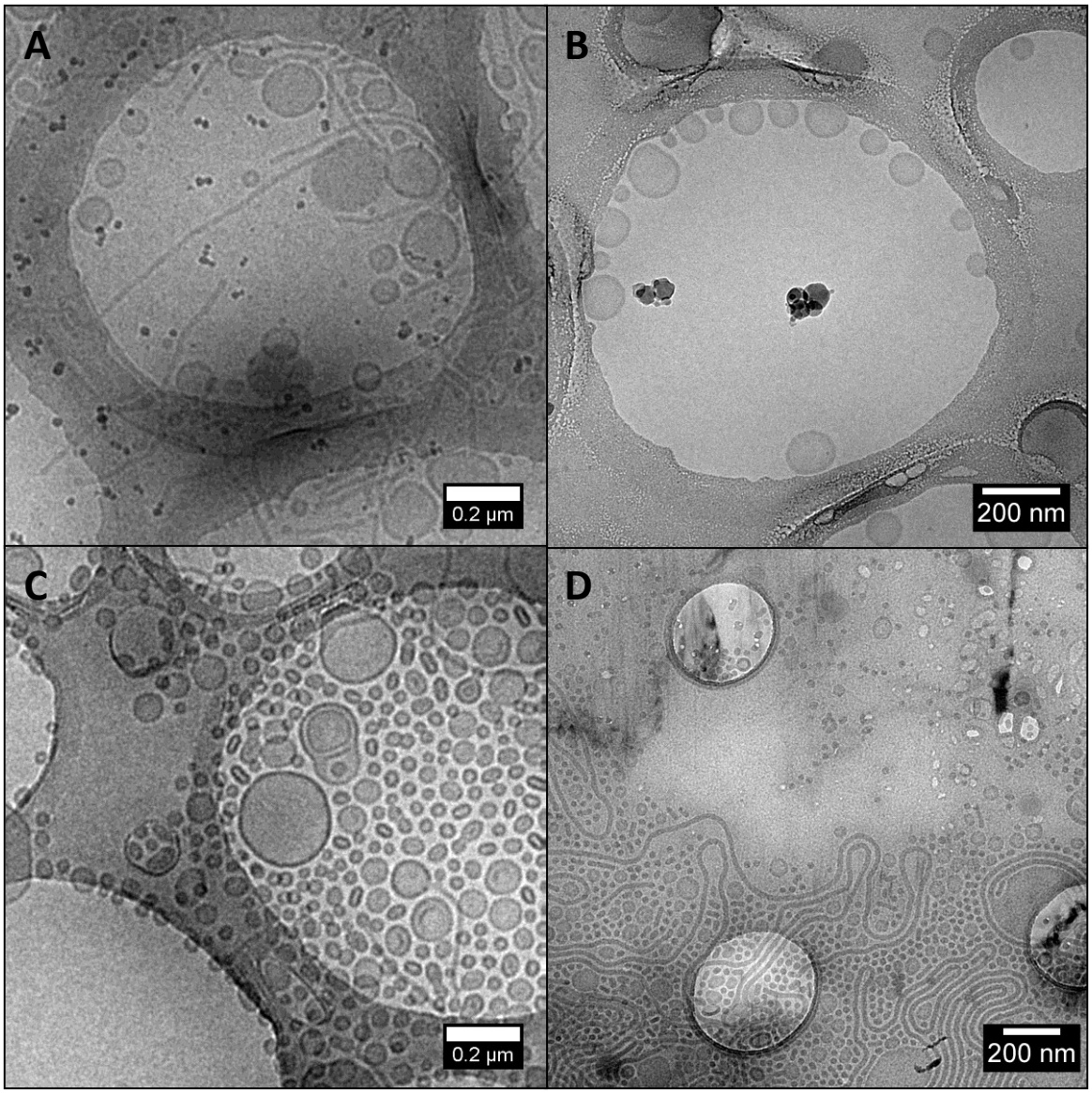

Figure 4-6. Effect of organic to aqueous ratio on vesicle morphology

Cryo-TEM images showing the effect of organic to aqueous ratio on vesicle morphology. A) 10% final DMSO resulted in vesicles and worms. B, C) 30% and 50% final DMSO resulted in uniform, unilamellar vesicles. D) 70% final DMSO resulted in vesicles and worms.

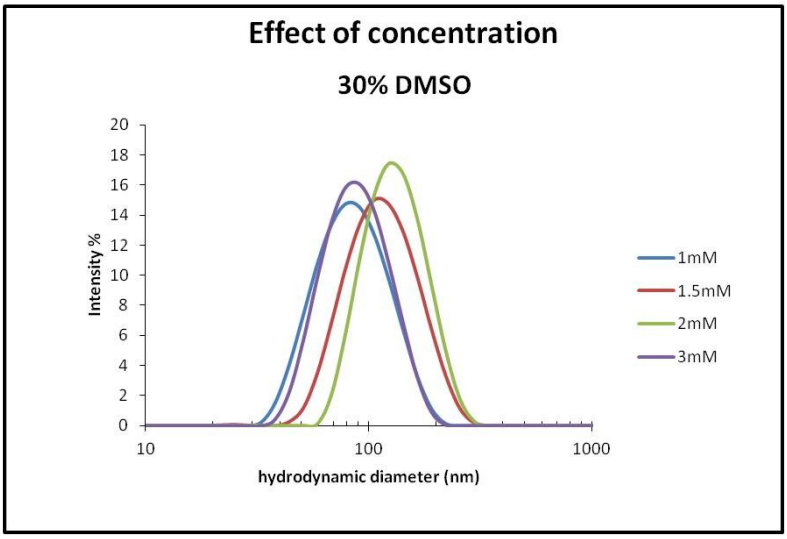

Figure 4-7. Effect of polymer concentration on nanovesicle size

DLS measurements showing differences in vesicle size with varying OB29 in DMSO concentration.

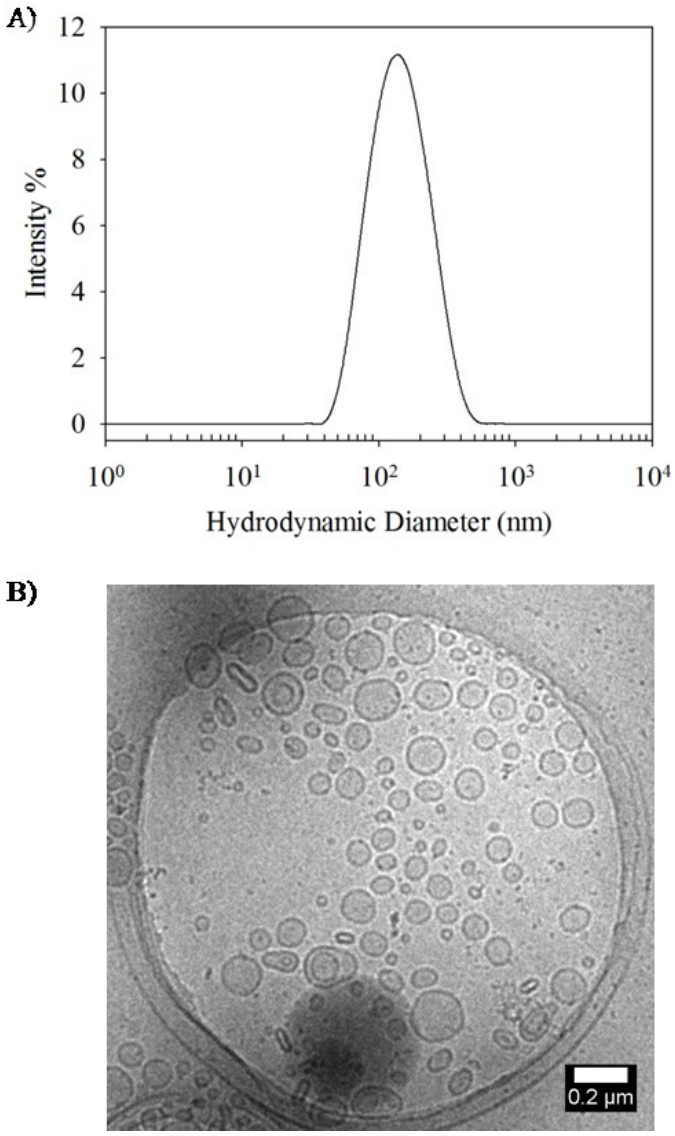

Figure 4-8. DLS and cryo-TEM showing final conditions for nanovesicle self-assembly

Vesicles prepared with DMSO containing 1.5 mM OB29 and 10% w/w of PZn_2, directly injected into 0.1 M PBS followed by 5 min of vortexing. Vesicles were dialyzed to remove DMSO. A) Size distribution of polymersomes in (B) as determined by dynamic light scattering. B) cryo-TEM image of polymersomes containing 10% PZn_2 in the membrane.

C. Nanovesicle rupture determined by PZn_2 emission shift

The *meso*-to-*meso* ethyne-bridged (porphinato)zinc(II) fluorophore (PZn_2, Figure 4-9) has been previously reported to undergo an emission shift in response to its environment; deformation of micron-scale OB29 vesicles was monitored by this approach .[27] Encapsulation within the nano-polymersome membrane restricts the mean PZn-PZn torsional angle, causing PZn_2 to adopt a more planar structure and red-shift in emission compared to emission in solution. Upon irradiation and membrane destabilization, PZn_2 encounters more free volume within the membrane and can increase its mean torsional angle, causing a blue-shift in emission relative to the unirradiated state.[27] Thus, PZn_2 emission wavelength is a convenient and accurate way to monitor membrane destabilization. We expect PZn_2 to maintain a similar conformation within nano-polymersomes as micron-polymersomes because the thickness of the hydrophobic membrane does not change.[28]

To probe nanovesicle rupture, vesicles were irradiated with visible light for increasing amounts of time (1, 5, 10, 20 min). A multispectral imaging camera was used to determine an aggregate PZn_2 emission of the bulk polyersome-containing solution after each irradiation period. PZn_2 emission blue-shifted from 714 nm to 705 nm with increasing irradiation times (Figure 4-10A), consistent with PZn_2 adopting a more twisted structure in a less conformationally restricted environment (Figure 4-10B). The quantum yield for release was not determined, however, 20-min irradiation correlated well with a

positive control release sample where a surfactant, Triton-X 100, was added to fully destabilize the membrane. These data were consistent with vesicle rupture.

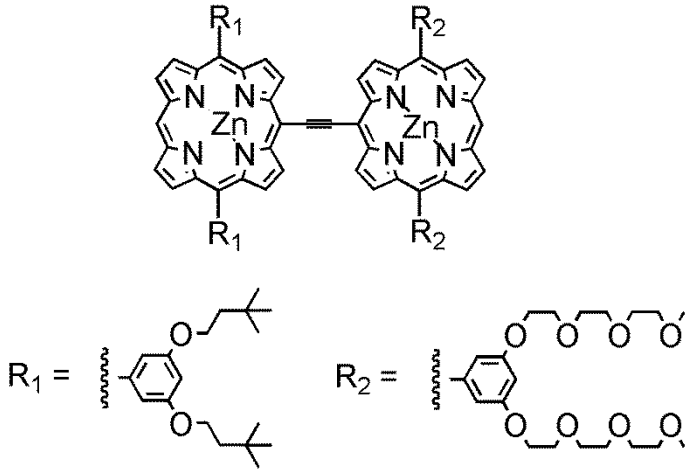

Figure 4-9. Structure of meso-to-meso ethyne-bridged (porphinato)zinc(II) dimer (PZn_2)

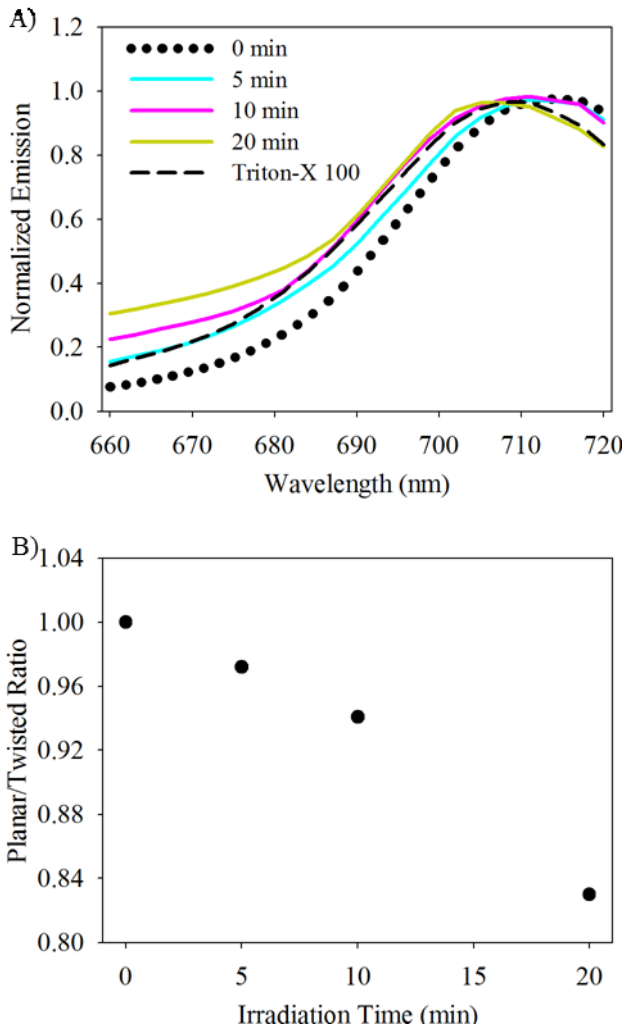

Figure 4-10. Membrane deformation detected by PZn_2 emission blue-shift.

A) The emission spectra for PZn_2 in nano-polymersomes were detected as function of irradiation time. The emission blue-shifted with increasing irradiation time. B) Normalized ratio of I_{714} (planar) to I_{705} (twisted).

D. Encapsulation and release of oligonucleotides

To confirm that oligonucleotides preferentially reside in the aqueous core, initial loading experiments were explored in micron-sized vesicles and confocal laser scanning microscopy (CSLM) was used for imaging. A 25-mer fluorescently labeled antisense morpholino (fl-MO) was purchased from Gene Tools (Philomath, WA) and loaded in micron vesicles according to methods described in section 4II-A and 4II-C. Micron-sized vesicles were imaged, and distribution of fluorescence was seen throughout the aqueous core as shown in Figure 4-11. A dual-loading experiment was performed to confirm localization of PZn_2 in the hydrophobic membrane and a 25-mer Alexa-488 labeled DNA in the aqueous core (Figure 4-12). Finally, control vesicles containing no aqueous or hydrophobic encapsulants were imaged to confirm fluorescent signal was due to PZn_2 and fluorescently labeled oligos (Figure 4-13).

Nanovesicles containing fl-MO were prepared by including 5 nmol of fl-MO in the aqueous solution (0.1 M PBS) prior to the self-assembly process. PZn_2 (10 mol%) and 10k dextran (10 mg/mL) were included to make the vesicles light-activatable. To quantify fl-MO loading in nanovesicles, unencapsulated fl-MO was separated and quantified. After self-assembly, the vesicles were dialyzed against 0.1 M PBS in a 3.5 kDA molecular weight cutoff dialysis cassette to remove DMSO, but retain all fl-MO. Unencapsulated fl-MO was then removed with a 50 kDa molecular weight cutoff Amicon centrifugal filter. Quantification of fl-MO with Abs_{260} revealed a total fl-MO encapsulation of 0.58 nmol, or 11.5% of the starting quantity. This quantity was

corroborated with quantification by the fluorophore with a standard curve. Attempts were made to increase fl-MO loading efficiency by increasing the starting quantity, however, this resulted in similar absolute loading. This suggests that the maximum amount of loading is governed by vesicle size and number, not by starting concentration.

Release experiments were done to determine the amount of fl-MO released as a function of irradiation time. fl-MO-loaded nanovesicles were placed in a PDMS well and irradiated with confocal lasers (488, 515, 543, 633 nm) for increasing amounts of time (0, 2, 10, 20 min). Positive (0.1% Triton-X 100) and negative (untreated) control samples were also prepared. Fl-MO was removed by sizing with an Amicon centrifugal filter. The released fl-MO was quantified by fluorescein emission (Figure 4-14). The percent release was calculated by dividing the fluorescence of the irradiated sample by the fluorescence of 100% release (Equation 1). A positive control was used as 100% release, and a negative control was subtracted out as background. These values were corrected for minor variations in volume. Percent release was plotted as a function of time, shown in Figure 4-15.

Equation 1: $$\frac{Em_{\,irradiated} - Em_{\,background}}{Em_{\,triton} - Em_{\,background}} \times 100\%$$

Within the first 2 min of irradiation, 9% of fl-MO was released. Release with time was fairly linear, and after 20 min of irradiation this release increased to 61%. Although this was a significant fractional release, the absolute quantity of fl-MO released after 20

min of irradiation was approximately 350 pmol per 1 mL sample. To make this feasible for *in vivo* antisense applications, this sample would have to be concentrated 1000-fold to 1 μL, risking particle aggregation. Thus, morpholino encapsulation and release with nano-polymersomes was not pursued further.

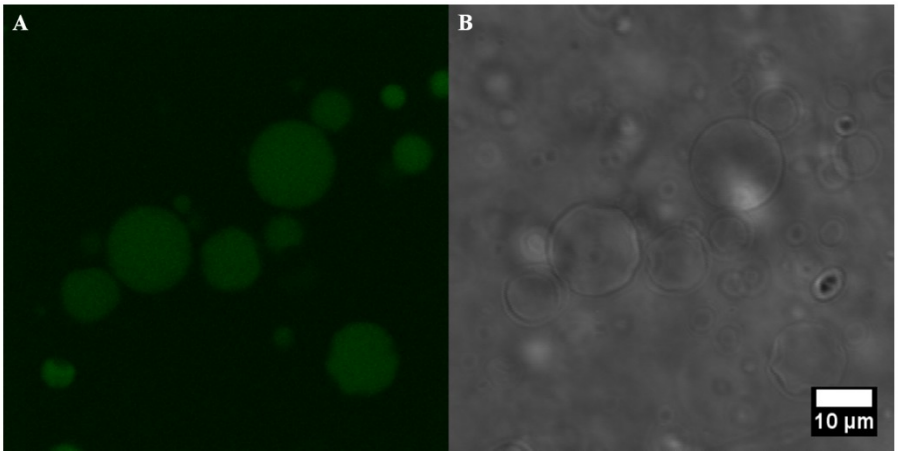

Figure 4-11. Encapsulation of fluorescein-labeled MO in micron vesicles

A) Fluorecein emission from fl-MO and B) DIC image. Scale bar represents 10 µm.

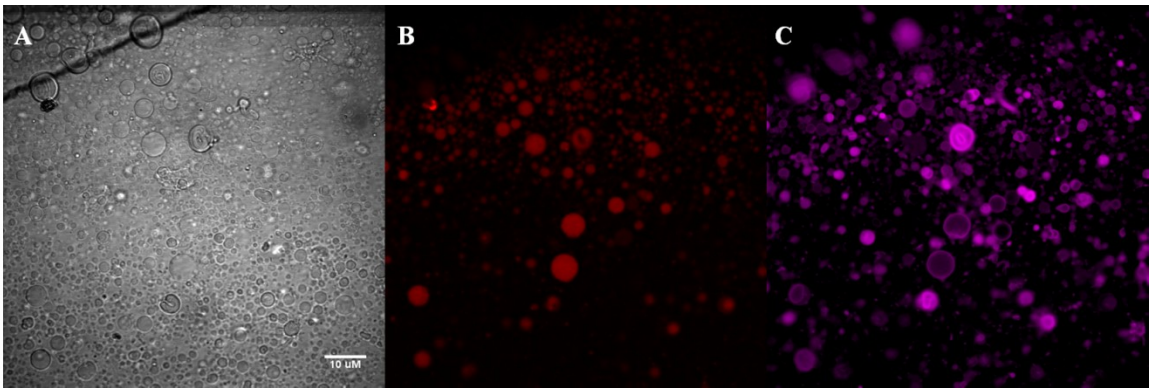

Figure 4-12. Dual encapsulation of Alexa 488-DNA and PZn_2 in micron vesicles

A) DIC image, B) Alexa-488 emission from DNA, and C) PZn_2 emission. Scale bar represents 10 µm.

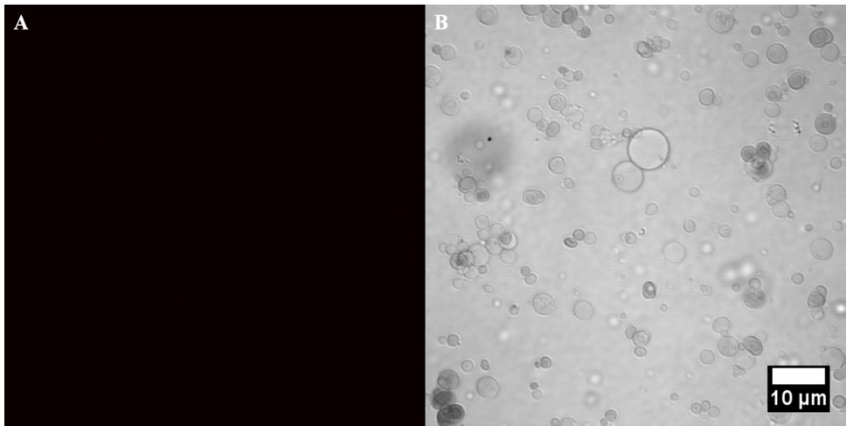

Figure 4-13. Unloaded micron vesicles

A) PZn_2 emission channel and B) DIC image. Scale bar represents 10 µm.

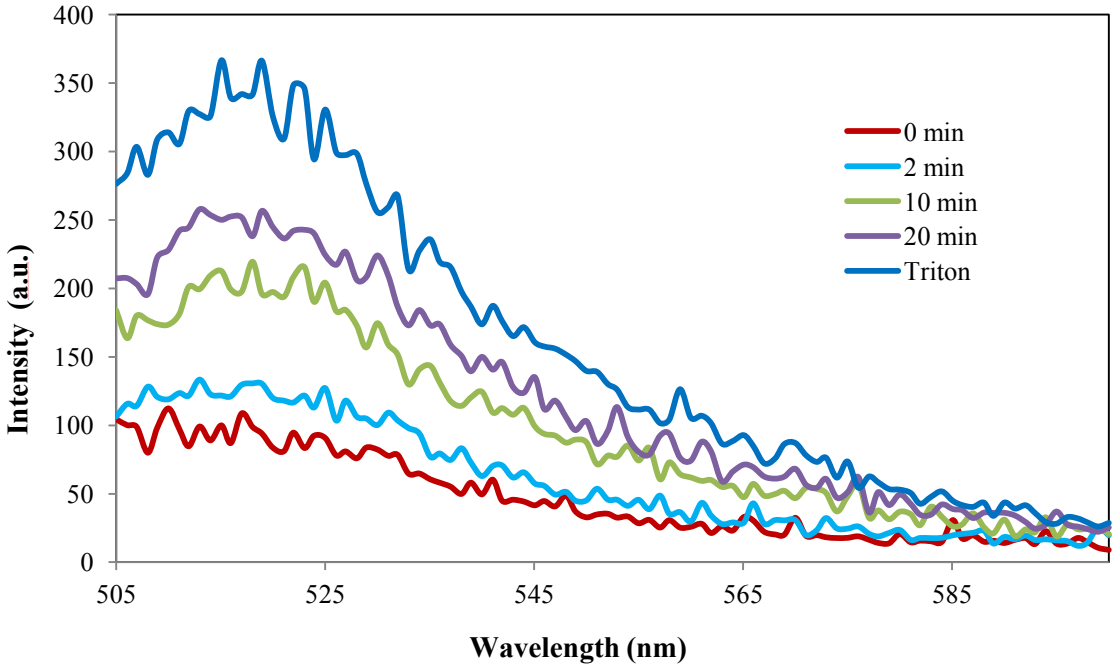

Figure 4-14. Fluorescence intensity of fl-MO as a function of irradiation time

Nano-vesicles containing fl-MO were irradiated for increasing amounts of time. Released fl-MO was separated out and quantified via emission at 517 nm. A positive control (0.1% Triton-X) and negative control were also analyzed for fl-MO release.

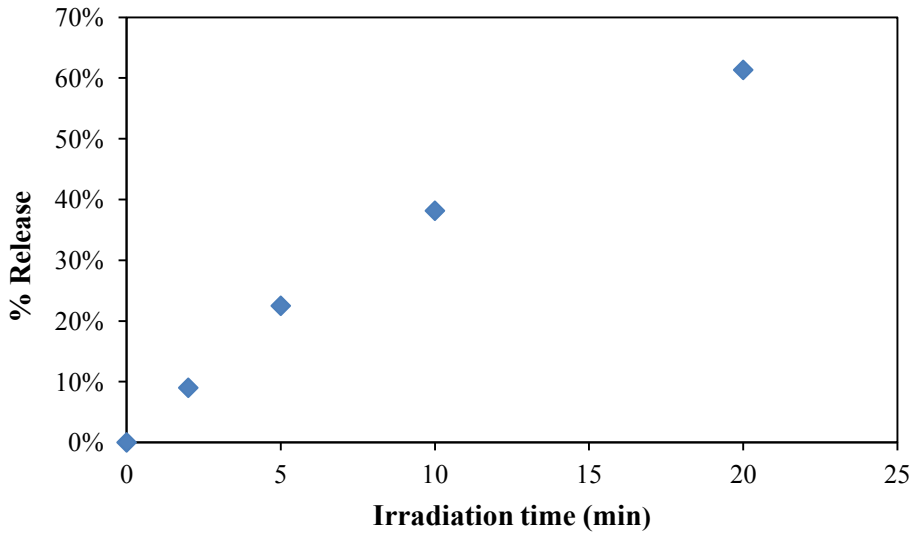

Figure 4-15. Release curve for fl-MO loaded nanovesicles

Fractional fl-MO release was calculated as a function of irradiation time with 488, 515, 543, and 633 nm according to Equation 1. Release percentages were calculated comparing full (100%) release with a surfactant (0.1% Triton-X).

E. FITC loading and release from nanovesicles

To further probe this photoresponsive nano-polymersome system, a model hydrophilic molecule, fluorescein isothiocyanate (FITC), was encapsulated. The photoresponse of the nano-polymersomes was tuned by the irradiation time, presence of dextran, and wavelength of light. Our previous work developed a generalized system for tuning the photoresponsiveness of micron-sized polymersomes.[26] It was determined that including a high molecular weight dextran in the aqueous core of polymersomes and PZn_2 in the membrane was required for vesicle rupture. It was concluded that dextran likely interacts with the inner leaflet of the bilayer membrane and reduces its elasticity, whereas PZn_2 (a highly absorptive chromophore with modest quantum yield) functions to generate heat upon irradiation. The combined effect produces an asymmetric thermal stretching of the membrane, ultimately causing rupture.[26] We translated these findings to photoresponsive nanovesicles, with a modification to encapsulate lower molecular weight dextran (10 kDa) in the aqueous core due to the smaller luminal volume of nano-polymersomes. It was also hypothesized that the membrane could be destabilized from the thermal expansion caused by PZn_2 alone because of the increased curvature of nanovesicles.

To assess the role for dextran, FITC was loaded into the aqueous core of nano-polymersomes with and without the inclusion of 10 kDa dextran in the aqueous core. Both systems were irradiated with either 488-nm laser, or via combination of four visible wavelength lasers (488, 515, 543, 633 nm). The combination of four lasers was chosen as

an extension of our previous work with micron-vesicles, corresponding to several absorbance features of PZn_2 in the polymersome membrane. The 488-nm laser was chosen as a single irradiation source as PZn_2 absorbs maximally near this wavelength. The release curves for these four conditions (+/- dextran, 488 nm/all lasers) are shown in Figure 4-16. As expected, percent release (calculated from Equation 1) was identical within experimental error when using 488 nm only (Figure 4-16B) vs. the combination of visible lasers (Figure 4-16D). This provided additional evidence that vesicle rupture was due to PZn_2 absorption and not a non-specific effect of irradiation, as the combined laser power was significantly greater than 488 nm alone. As hypothesized, due to the increased curvature, nano-polymersomes ruptured without dextran (Figure 4-16A, 4-16C), contrary to the previous micron-vesicle polymersome system. Nonetheless, dextran-loaded nanovesicles consistently exhibited higher % release under all conditions tested (Figure 4-16). Nano-polymersomes were also prepared without PZn_2 and dextran, and maximum irradiation of these vesicles resulted in negligible FITC release (Figure 4-17), which confirmed the need for PZn_2.

These four conditions (+/- dextran, 488 nm or all lasers) provided a versatile system that can be adapted to a variety of different experiments depending on factors such as laser availability and desired amount of cargo release. To better understand the mechanism of rupture, nano-polymersomes were imaged with cryo-TEM before and after irradiation (Figure 4-18). Figure 4-18A shows a large population of uniform, unilamellar vesicles before irradiation. After irradiation, a variety of non-vesicular structures were

present (Figure 4-18B). These images suggest a rupture mechanism where the membrane buckles and folds over itself, or is disrupted and reassembles. The mechanism is further corroborated by DLS, showing no significant change in size post-irradiation. The cryo-TEM images also provide insight as to why the release curves plateau without reaching 100% release. Figure 4-18B shows a large number of vesicles that reassembled after membrane deformation. It is likely that the entire contents of the vesicle does not get released prior to reassembly.

F. Loading and releasing metal ions with photoresponsive nano-polymersomes

To demonstrate the versatility of this system, encapsulation and release techniques were applied to two metal ions with importance in cellular processes. Ca^{2+} or Zn^{2+} was incorporated into the aqueous core of nano-polymersomes without any changes to the direct-injection self-assembly process and the hydrodynamic diameter was measured to confirm self-assembly (Figure 4-19). These vesicles were prepared both with and without 10 kDa dextran and subjected to varying irradiation times with 488-nm laser. Figure 4-20 shows release curves for Ca^{2+} (A) and Zn^{2+} (B). Both metal ions were successfully loaded and released from nano-polymersomes, with maximum release occurring for both ions after 10-min irradiation. Consistent with FITC photo-release, both metal ions were released from nano-polymersomes not containing dextran in the aqueous core, with a slightly lower fractional release. The concentration of Ca^{2+} after vesicle

rupture was determined to be 757 μM from vesicles containing dextran, and 428 μM from vesicles without dextran. The concentration of Zn^{2+} after vesicle rupture was 35 μM with dextran and 11 μM without dextran. This was determined by full release from vesicles with Triton-X 100 and quantified via corresponding Oregon Green-488 calibration curves. The average number of ions per vesicle was calculated to be 70,000, assuming a polymer density of 1 chain/nm^2, which has previously been used to calculate vesicle number.[29] Although the concentration of loaded Zn^{2+} is significantly lower compared to Ca^{2+}, it is appropriate for biological applications, as the cellular concentration of free Zn^{2+} is typically on the picomolar to nanomolar range.[30] Currently, DM-nitrophen (Millipore, Billerica, MA) is the most efficient caged Ca^{2+} chelator, based on its high calcium affinity before photolysis, and low affinity post-photolysis. Upon irradiation with UV light (365 nm), DM Nitrophen can provide up to a 600 μM jump in Ca^{2+} concentration in living neurons,[4] however, DM Nitrophen must be employed at similarly high concentration. As noted above, the nano-polymersome system can provide a similar Ca^{2+} concentration jump, with the added benefits of visible-light release, potential for greater biological stability, and the ability to encapsulate tens of thousands of ions per vesicle. Further optimization of nano-polymersomes may be possible, for example, to accelerate the rate and % yield of metal ion release.

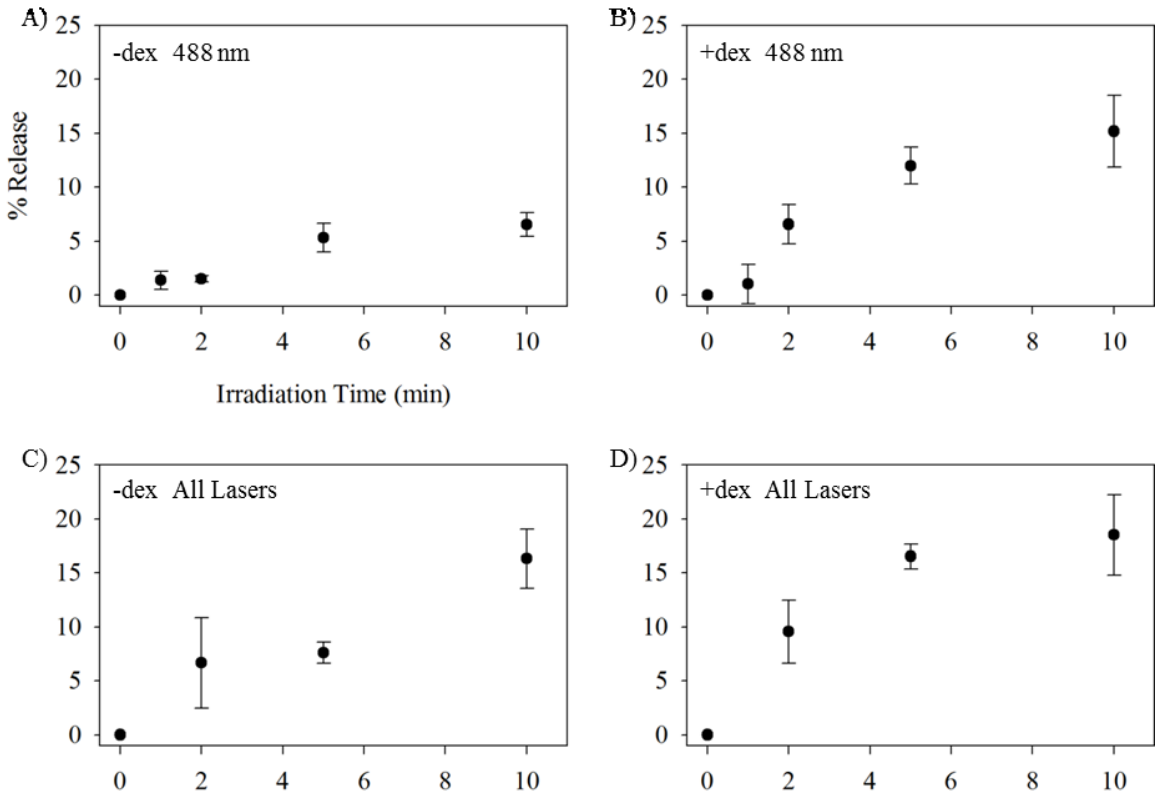

Figure 4-16. Release curve of FITC-loaded polymersomes

Nano-polymersomes containing PZn_2 in the membrane were irradiated for various amounts of time. A) Polymersomes containing no dextran in the core and irradiated with 488 nm laser. B) Polymersomes containing 10 kDa dextran in the core and irradiated with 488 nm laser. C) Polymersomes containing no dextran in the core and irradiated with 488, 515, 543, 633 nm lasers. D) Polymersomes containing 10 kDa dextran in the core and irradiated with 488, 515, 543, 633 nm lasers.

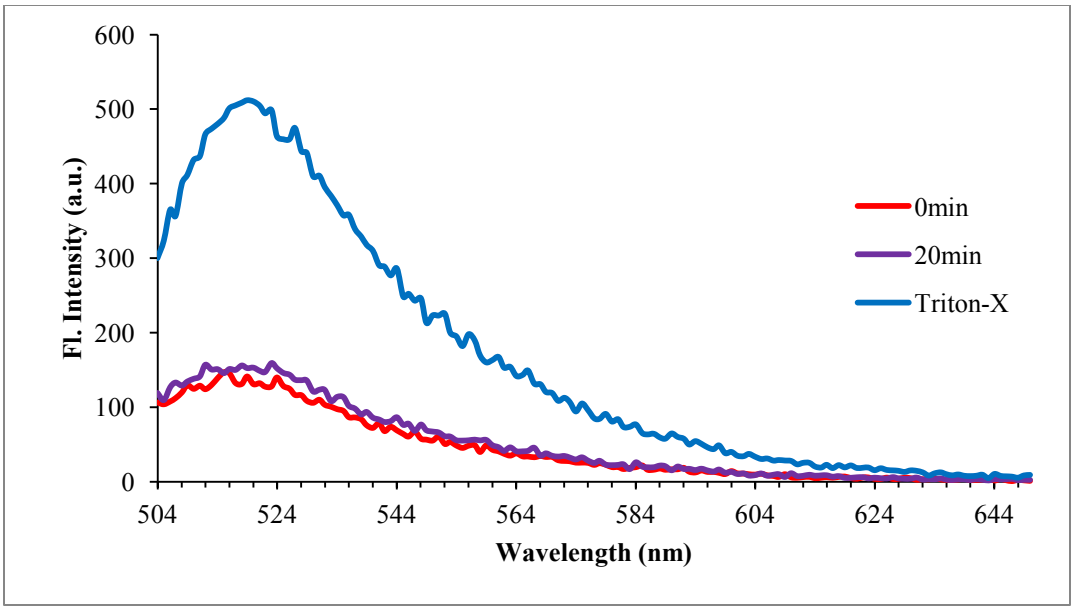

Figure 4-17. FITC release from nano-vesicles without PZn_2 or dextran

Nano-polymersomes were made without PZn_2 in the membrane or dextran in the aqueous core. These vesicles were subjected to 20-min irradiation (488, 515, 543, 633 nm), and fluorescence intensity was compared to a positive control sample (Triton-X added to 0.1 vol%). Release from these vesicles was negligible.

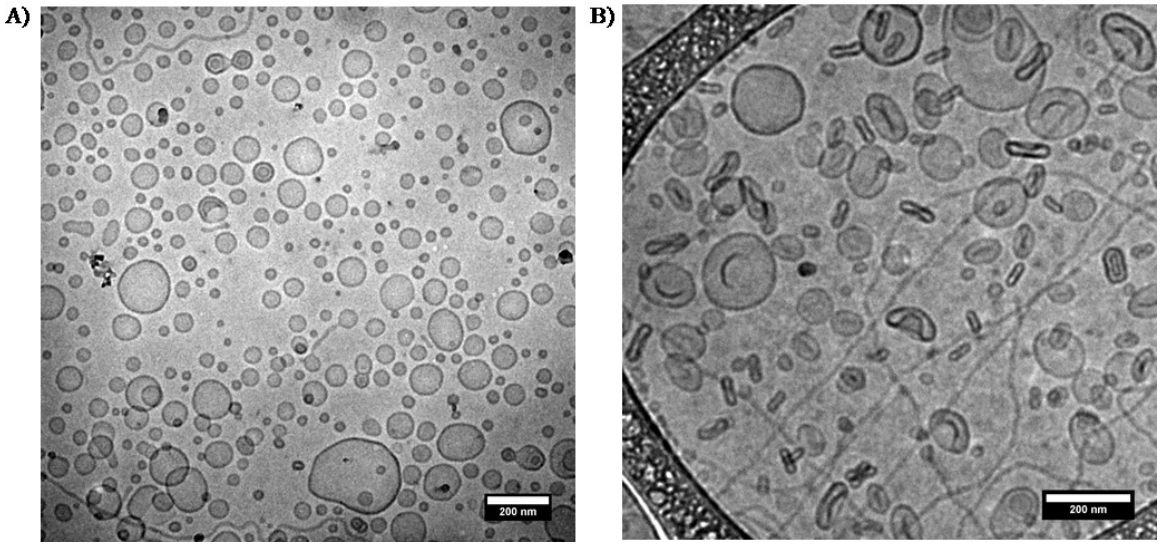

Figure 4-18. Morphological change in polymersomes after light irradiation.

Polymersomes containing 10% PZn_2 in the membrane and 10 kDa dextran and FITC in the core were imaged with cryo-TEM A) before light irradiation, and B) after 20-min irradiation with 488, 515, 543, 633 nm lasers.

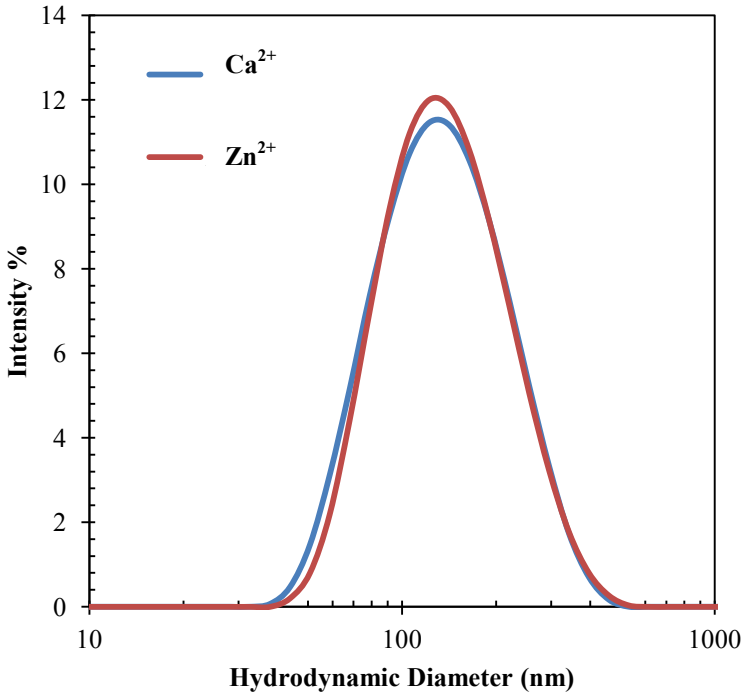

Figure 4-19: Hydrodynamic diameter of metal ion-loaded nanovesicles determined by DLS.

The hydrodynamic diameter of vesicles containing Ca^{2+} was determined to be 120 nm (blue) and vesicles containing Zn^{2+} was determined to be 120 nm (red).

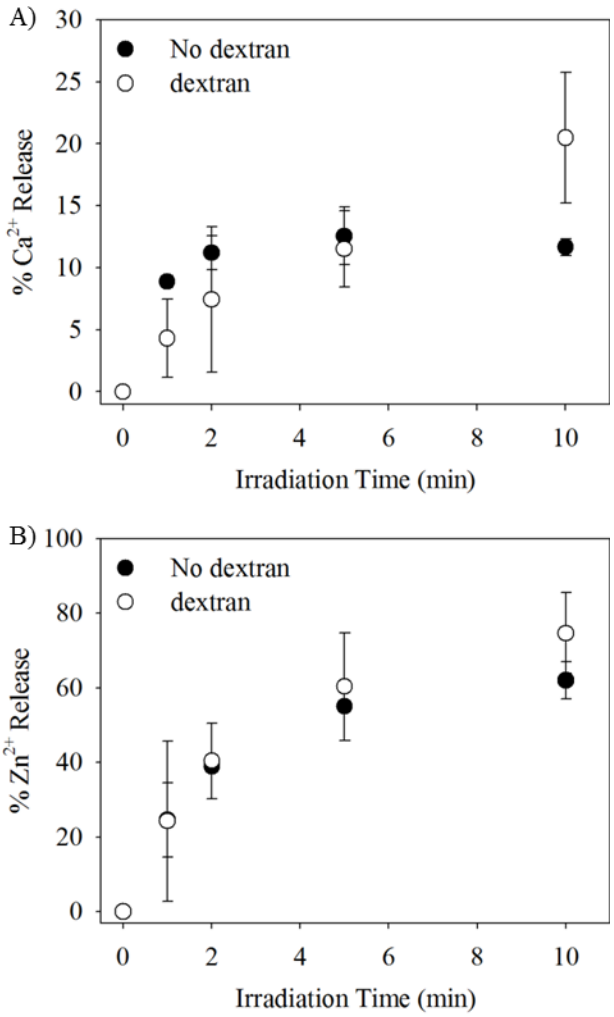

Figure 4-20. Release curves of metal ion-loaded polymersomes.

Nano-polymersomes containing PZn_2 in the membrane were irradiated for various amounts of time. A) Ca^{2+}-loaded polymersomes. B) Zn^{2+}-loaded polymersomes.

G. Nano-polymersomes *in vivo*

Initial screenings to determine *in vivo* applicability were explored. Nanovesicles were prepared with PZn_2 as a hydrophobic encapsulant and Texas-Red dextran in the aqueous core. Vesicles were microinjected into zebrafish embryos at the 1-cell stage. Immediately following injections, the embryos were imaged to determine vesicle dispersion. The embryos were imaged up through 30 hpf. Figure 4-21 A-B shows the embryos immediately after injection at the 1-cell stage. Both the PZn_2 (A) and Texas Red (B) channels show even distribution of the vesicles within the cellular compartment of the embryo only. Figure 4-20 C-D shows the embryos at 20 hpf, with PZn_2 (A) and Texas Red (B) still detectable, and still evenly distributed through the embryo. The embryos were monitored up through 30 hpf, and development and survival were comparable to the uninjected controls. Embryos injected later than the 1-cell stage did not show even distribution of vesicles throughout the cells, showing that the vesicles were not efficiently distributed through cytoplasmic streaming, rather incorporated during cellular division.

To confirm passive uptake of nano-polymersomes in cells, uptake studies were performed. Nano-vesicles prepared with PZn_2 were added to cultured macrophages and incubated for four hours. Cells were washed with PBS and imaged for PZn_2 emission within the cell (Figure 4-22). A z-stack image confirmed uptake within the cell and not just adherence to the cell surface.

A PZn_2 emission wavelength shift experiment was performed in zebrafish embryos to probe vesicle rupture *in vivo*. Nanovesicles (4x concentrated) were

microinjected into zebrafish embryos at the 1-cell stage. Confocal microscopy was used to confirm nano-vesicle injection and cellular distribution at the 4-cell stage. A single embryo was placed in a glass-bottom dish in E3 medium, and irradiated continuously with 488 nm with an ROI selected to include only the cellular compartment (rastering the ROI for 5 min). Embryos were imaged before (Figure 4-23A) and after (Figure 4-23B) irradiation to confirm that PZn_2 emission was still detectible, and to confirm that the embryo was not damaged in the irradiation process. A NuanceFX multispectral camera was used to measure the PZn_2 emission wavelength from the cellular compartment only before and after 5-min irradiation (Figure 4-23C). An identical wavelength shift was observed *in vivo* as was seen in bulk, confirming vesicle rupture in zebrafish embryos. The complete shift to 705 nm was seen with significantly less irradiation time *in vivo* than in the bulk sample (5 min vs. 20 min), likely due to the smaller volume being irradiated.

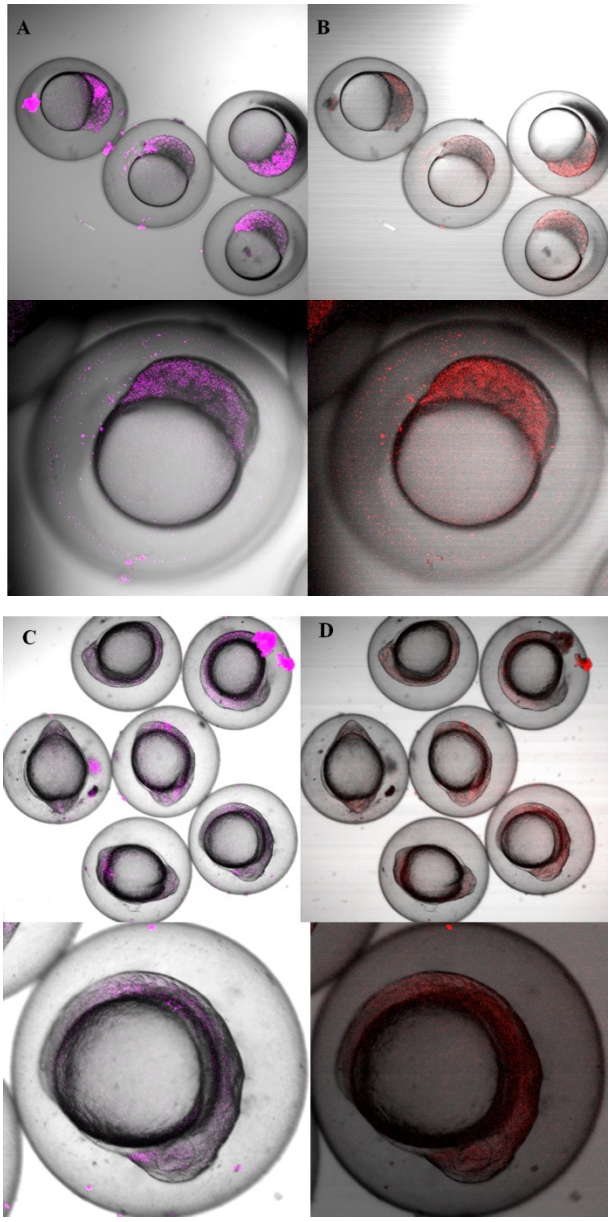

Figure 4-21. Confocal images of zebrafish embryos injected with nanovesicles.

Zebrafish embryos were microinjected with nanovesicles containing PZn_2 in the membrane (purple) and Texas-Red dextran (red) in the aqueous core. Embryos were imaged at A,B) 1-cell stage and C,D) 20 hpf to determine vesicle distribution and embryo viability. Single embryos were imaged with a 10x objective and multi-embryo images were imaged with a 4x objective.

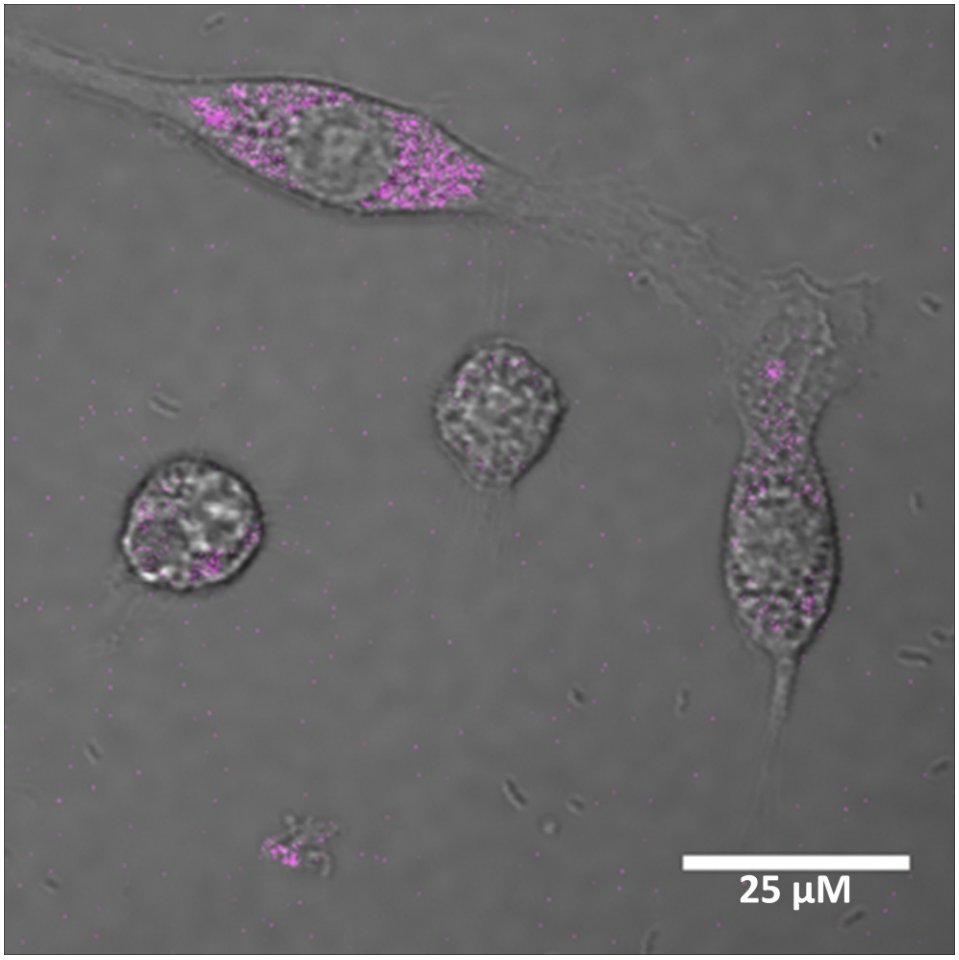

Figure 4-22. Cell uptake of nano-polymersomes

Nanovesicles containing PZn_2 were incubated with macrophages to confirm passive uptake. Cells were imaged after 4 h incubation.

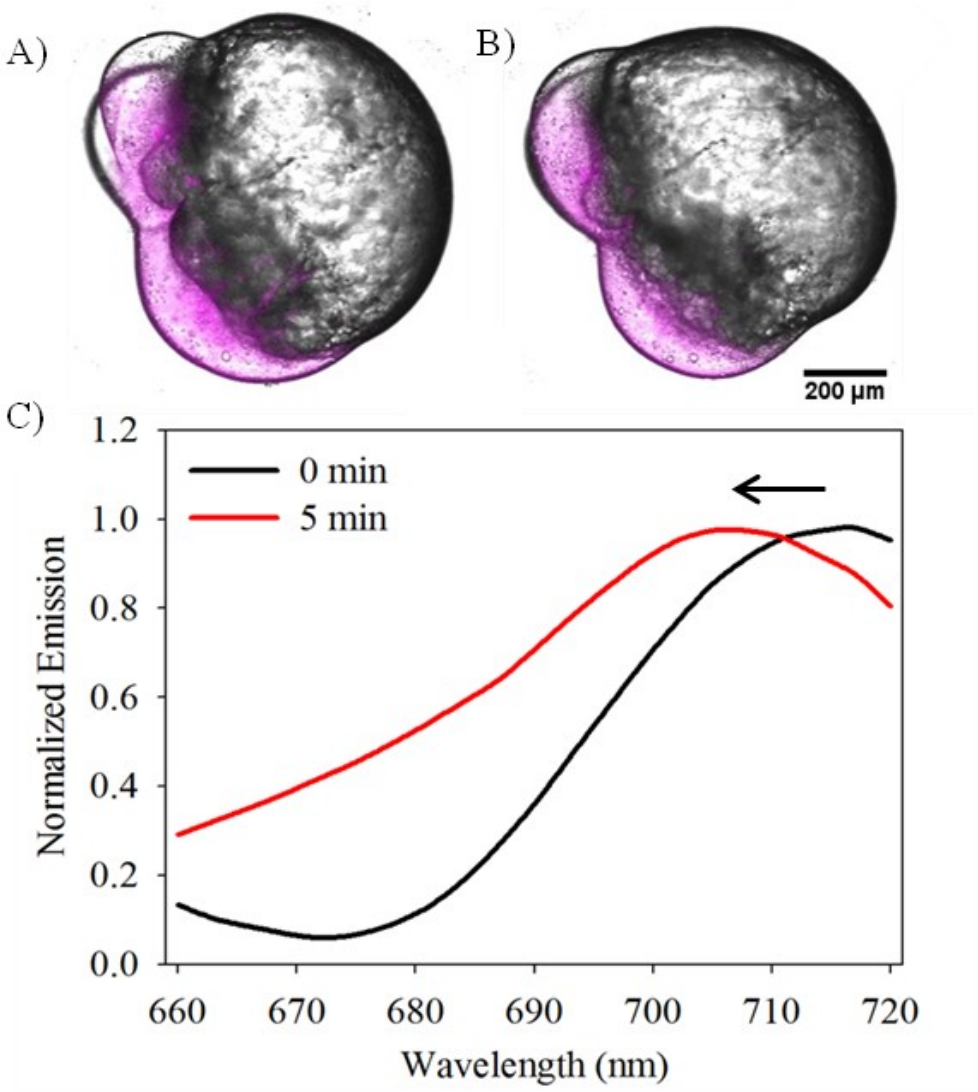

Figure 4-23. PZn_2 wavelength shift *in vivo*

A) PZn_2 emission in a zebrafish embryo before irradiation and B) after 5 min irradiation with 488, 515, 543 and 633 nm. C) The emission spectra for PZn_2 in nano-polymersomes were detected as function of irradiation time. The emission blue-shifted with increasing irradiation time.

IV. Conclusion:

We reported a visible light-responsive nano-polymersome system capable of encapsulating and releasing oligonucleotides, small molecules (FITC) and metal ions (Ca^{2+} and Zn^{2+}). This system uses PZn_2, a hydrophobic porphyrin photosensitizer, encapsulated in the membrane to provide thermal expansion and subsequent membrane rupture. The inclusion of dextran in the aqueous core was probed for FITC and metal ion systems, and shown to increase loading and fractional release. However, release can still be achieved without dextran, unlike our previously reported micron-sized photoresponsive polymersomes.[26]

Morpholino loading and release concentrations demonstrated were not sufficient for *in vivo* knockdown experiments, however, this system could still be useful in applications that require lower concentrations of oligo release. Importantly, we demonstrated metal ion release at concentrations suitable for cellular applications. Our system has many potential benefits over many previously reported caged chelators, namely, the use of 488-nm light, and the ability to encapsulate different metal ions without the need for modifying metal chelation or changing the self-assembly process. The PZn_2 emission shift provided a built-in reporter for vesicle rupture, which can be useful for confirming spatiotemporal release in biological systems. Additionally, due to the broad absorbance spectrum of PZn_2, it is feasible to extend future work to releasing with near-IR light, as PZn_2 has λ_{max} at 714 nm.[17] Finally, it was demonstrated that nanovesicles could be passively uptaken by cells, as well as microinjected into zebrafish

embryos with no detectable toxicity. Vesicle rupture *in vivo* was demonstrated through a PZn_2 emission shift.

V. References

(1) Bush, A. I. *Curr. Opin. Chem. Biol.* **2000**, *4*, 184-191.

(2) Curtain, C.; Separovic, F. *Eur. Biophys. J.* **2008**, *37*, 239-239.

(3) Lam, A.; Florez, C. M.; Mylvaganam, S.; Valiante, T.; Carlen, P. L.; Ohayon, E. L. *Epilepsia* **2014**, *55*, 224-224.

(4) Ellis-Davies, G. C. R. *Chem. Rev.* **2008**, *108*, 1603-1613.

(5) Kaur, K.; Gupta, R.; Saraf, S. A.; Saraf, S. K. *Compr. Rev. Food Sci. Food Saf.* **2014**, *13*, 358-376.

(6) Ellis-Davies, G. C. *Nat. Methods* **2007**, *4*, 619-628.

(7) Ellis-Davies, G. C. R. *Nat. Methods* **2007**, *4*, 619-628.

(8) Mbatia, H. W.; Burdette, S. C. *Biochemistry* **2012**, *51*, 7212-7224.

(9) Marcotte, N.; Plaza, P.; Lavabre, D.; Fery-Forgues, S.; Martin, M. M. *J. Phys. Chem. A* **2003**, *107*, 2394-2402.

(10) Momotake, A.; Lindegger, N.; Niggli, E.; Barsotti, R. J.; Ellis-Davies, G. C. R. *Nat. Methods* **2006**, *3*, 35-40.

(11) Bandara, H. M.; Kennedy, D. P.; Akin, E.; Incarvito, C. D.; Burdette, S. C. *Inorg. Chem.* **2009**, *48*, 8445-8455.

(12) Gwizdala, C.; Basa, P. N.; MacDonald, J. C.; Burdette, S. C. *Inorg. Chem.* **2013**, *52*, 8483-8494.

(13) Zhang, X.; Chen, Y. *Phys. Chem. Chem. Phys.* **2010**, *12*, 1177-1181.

(14) Canto, E. D.; Natali, M.; Movia, D.; Giordani, S. *Phys. Chem. Chem. Phys.* **2012**, *14*, 6034-6043.

(15) Discher, B. M.; Won, Y. Y.; Ege, D. S.; Lee, J. C. M.; Bates, F. S.; Discher, D. E.; Hammer, D. A. *Science* **1999**, *284*, 1143-1146.

(16) Kamat, N. P.; Katz, J. S.; Hammer, D. A. *J. Phys. Chem. Lett.* **2011**, *2*, 1612-1623.

(17) Ghoroghchian, P. P.; Frail, P. R.; Susumu, K.; Blessington, D.; Brannan, A. K.; Bates, F. S.; Chance, B.; Hammer, D. A.; Therien, M. J. *Proc. Natl. Acad. Sci. U. S. A.* **2005**, *102*, 2922-2927.

(18) Katz, J. S.; Zhong, S.; Ricart, B. G.; Pochan, D. J.; Hammer, D. A.; Burdick, J. A. *J. Am. Chem. Soc.* **2010**, *132*, 3654-3655.

(19) Christian, N. a.; Milone, M. C.; Ranka, S. S.; Li, G.; Frail, P. R.; Davis, K. P.; Bates, F. S.; Therien, M. J.; Ghoroghchian, P. P.; June, C. H.; Hammer, D. a. *Bioconjugate Chem.* **2007**, *18*, 31-40.

(20) Demirgöz, D.; Pangburn, T. O.; Davis, K. P.; Lee, S.; Bates, F. S.; Kokkoli, E. *Soft Matter* **2009**, *5*, 2011.

(21) Lin, J. J.; Ghoroghchian, P. P.; Zhang, Y.; Hammer, D. a. *Langmuir* **2006**, *22*, 3975-3979.

(22) Zupancich, J. a.; Bates, F. S.; Hillmyer, M. a. *Biomacromolecules* **2009**, *10*, 1554-1563.

(23) Cabane, E.; Malinova, V.; Menon, S.; Palivan, C. G.; Meier, W. *Soft Matter* **2011**, *7*, 9167-9176.

(24) Zhang, Q.; Ko, N. R.; Oh, J. K. *RSC Adv.* **2012**, *2*, 8079-8086.

(25) Ghoroghchian, P. P.; Frail, P. R.; Susumu, K.; Park, T.-H.; Wu, S. P.; Uyeda, H. T.; Hammer, D. a.; Therien, M. J. *J. Am. Chem. Soc.* **2005**, *127*, 15388-15390.

(26) Kamat, N. P.; Robbins, G. P.; Rawson, J.; Therien, M. J.; Dmochowski, I. J.; Hammer, D. A. *Adv. Funct. Mater.* **2010**, *20*, 2588-2596.

(27) Kamat, N. P.; Liao, Z.; Moses, L. E.; Rawson, J.; Therien, M. J.; Dmochowski, I. J.; Hammer, D. A. *Proc. Natl. Acad. Sci. U. S. A.* **2011**.

(28) Bermudez, H.; Brannan, A. K.; Hammer, D. A.; Bates, F. S.; Discher, D. E. *Macromolecules* **2002**, *4*, 8203-8208.

(29) Christian, N. A.; Milone, M. C.; Ranka, S. S.; Li, G.; Frail, P. R.; Davis, K. P.; Bates, F. S.; Therien, M. J.; Ghoroghchian, P. P.; June, C. H.; Hammer, D. A. *Bioconjugate Chem.* **2006**, *18*, 31-40.

(30) Stork, C.; Li, Y. *J. Mol. Signaling* **2010**, *5*, 1-6.

Chapter 5

Conclusions and future directions

I. Conclusions

The development of photoactivatable oligonucleotides has come a long way since initial efforts in our lab where we demonstrated RNase H-dependent RNA digestion with a light-activated DNA hairpin, and a light-responsive negatively charged peptide nucleic acid hairpin for antisense activity in zebrafish embryos.[1-4] Work presented in this thesis expanded these photochemical tools to three new caging methods. A bidirectional photo-regulated miRNA was designed to control a miRNA antagomir and exogenous miRNA with 365 nm light.[5] A ruthenium-caged morpholino for the photoregulation of antisense activity was presented, extending the photoactivation wavelength to the visible spectrum. Finally, a visible light-responsive nano-polymersome system was developed for the encapsulation and release of a variety of cargo, including metal ions, oligonucleotides, and a fluorescent dye.

Chapter 2 expanded upon our previously demonstrated caged hairpin design by exploring the benefit of one vs. two nitrobenzyl moieties. Incorporating a second photocleavable group within the blocking strand achieved a significantly higher T_m prior to irradiation, and an overall larger ΔT_m between the photolyzed and caged construct. This result was corroborated by remarkably low background activity (2%) prior to irradiation due to the number of bases that could be rendered inactive through hybridization with the biologically active miRNA antagomir. Additionally, this second photocleavable group limited the amount of sequence specificity needed in the design, as the near full-length blocking sequence needed little optimization in placement and length

to block function. A circular miRNA presented in Chapter 2 was the first example of a light-activatable miRNA for "turning on" an exogenous miRNA *in vivo.*

Chapter 3 presented the first example of a ruthenium photolinker, RuBEP, which was activated with visible light. RuBEP was designed with two alkyne-containing ligands for circularizing a bis-azido oligonucleotide through a Cu(I)-mediated [3+2] Huisgen cycloaddition reaction. This Ru photolinker was applied to the circularization of two morpholinos targeting early developmental genes in zebrafish, *ntl* and *chd,* and antisense activity was successfully photomodulated with 450-nm light. Circular designs provided benefits over hairpin designs, as the circularization process was nearly sequence independent without the need for a blocking sequence. Additionally, the exclusion of a blocking sequence avoided the risk of off-target effects upon dissociation.

Chapter 4 expanded caging techniques to the design of a light-responsive nano-polymersome. This design employed a meso-to-meso ethyne-bridged (porphinato)zinc(II) dimer, PZn_2, encapsulated in the hydrophobic membrane to harvest visible light for membrane destabilization. Nano-polymersomes encapsulated a variety of cargo, including oligonucleotides, a fluorescent dye, and metal ions. Photoresponsive release was tunable with wavelength, irradiation time, and dextran inclusion in the aqueous core. Nanocarriers provided a versatile method of caging through encapsulation, as a wide variety of cargo can be contained in the aqueous core with no modulation to the self-assembly process.

II. Future directions

New methods for caging oligonucleotides will soon make it possible to incorporate a small library of caging designs and light-activatable moieties. Having various caged oligos that can be photoactivated at different wavelengths will provide a method of multiplexing, or controlling multiple oligos sequentially with high spatiotemporal resolution.

One very promising application for multiplexing can be applied to recently published work from our lab by Lovatt and Ruble et al., demonstrating a method for non-invasively harvesting mRNA from single cells using transcriptome *in vivo* analysis (TIVA).[6] This method used a hairpin design based on the design presented in Chapter 2 as well as published RNA bandage designs by Richards et al.,[7] using a second photocleavable moiety in the blocking strand to achieve a large ΔT_m between the pre- and post-photolysis construct. The original TIVA design uses two nitrobenzyl moieties, which optimally photolyzes with 365 nm light. To realize many potential applications, a second TIVA-tag that photolyzes with visible light would be advantageous. Using RuBEP as a photolinker to develop circular Ru-TIVA is currently being explored to expand the TIVA-tag library, as well as to provide a TIVA construct that can be activated with two-photon light (Yeldell et al., unpublished work). By using the first generation TIVA-tag[6] in tandem with Ru-TIVA, sequential pull-down of mRNA, or multiplexing, may be achieved.

More generally, a library of ruthenium-based photolinkers spanning the visible spectrum will enable multiplexing for a multitude of applications, as RuBEP and future Ru photolinkers have the potential to circularize any bis-azido oligonucleotide. Additional applications potentially include elucidating gene regulatory systems in living model systems, where sequential gene knockdown is necessary to probe function.

III. References:

(1) Tang; Dmochowski, I. J. *Org. Lett.* **2004**, *7*, 279-282.

(2) Tang, X.; Dmochowski, I. J. *Angew. Chem., Int. Ed. Eng.* **2006**, *45*, 3523-3526.

(3) Tang, X.; Maegawa, S.; Weinberg, E. S.; Dmochowski, I. J. *J. Am. Chem. Soc.* **2007**, *129*, 11000-11001.

(4) Tang, X.; Richards, J. L.; Peritz, A. E.; Dmochowski, I. J. *Bioorg. Med. Chem. Lett.* **2005**, *15*, 5303-5306.

(5) Griepenburg, J. C.; Ruble, B. K.; Dmochowski, I. J. *Bioorg. Med. Chem.* **2013**, *21*, 6198-6204.

(6) Lovatt, D.; Ruble, B. K.; Lee, J.; Dueck, H.; Kim, T. K.; Fisher, S.; Francis, C.; Spaethling, J. M.; Wolf, J. A.; Grady, M. S.; Ulyanova, A. V.; Yeldell, S. B.; Griepenburg, J. C.; Buckley, P. T.; Kim, J.; Sul, J.-Y.; Dmochowski, I. J.; Eberwine, J. *Nat. Methods* **2014**, *11*, 190-196.

(7) Richards, J. L.; Tang, X.; Turetsky, A.; Dmochowski, I. J. *Bioorg. Med. Chem. Lett.* **2008**, *18*, 6255-6258.

Appendix A. Crystal structure determination of $Ru(bpy)_2(3\text{-ethynylpyridine})_2(PF_6)_2$

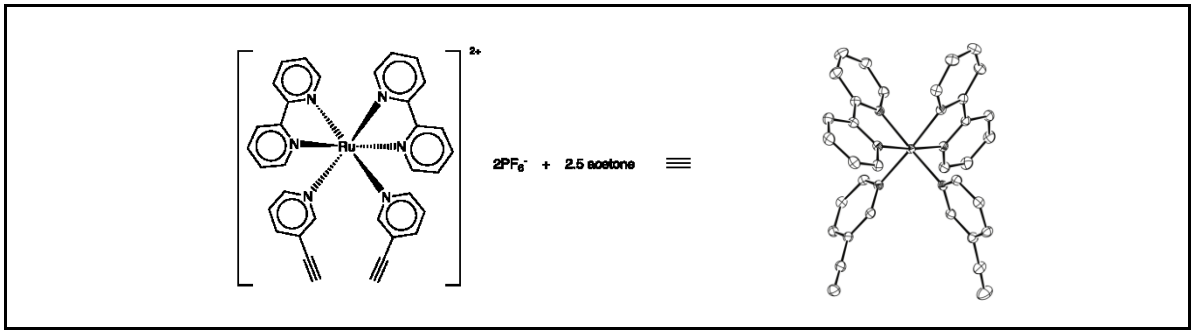

I. Methods

Compound $C_{34}H_{26}N_6P_2F_{12}Ru \bullet 2½$ acetone, crystallized in the Triclinic space group P$\bar{1}$ with a=11.2159(7)Å, b=12.5550(8)Å, c=18.1382(12)Å, α=70.206(3)°, β=85.323(3)°, γ=67.450(2)°, V=2216.1(2)Å^3, Z=2, and d_{calc} = 1.581 g/cm^3. X-ray intensity data were collected on a Bruker APEXII CCD area detector employing graphite-monochromated Mo-Kα radiation (λ=0.71073 Å) at a temperature of 100(1)K. Preliminary indexing was performed from a series of thirty-six 0.5° rotation frames with exposures of 10 seconds. A total of 2348 frames were collected with a crystal to detector distance of 37.6 mm, rotation widths of 0.5° and exposures of 20 seconds:

scan type	2Θ	ω	Φ	χ	frames
Φ	19.50	327.79	15.97	36.30	739
Φ	-20.50	342.55	321.55	-73.06	739
ω	-23.00	333.53	158.99	-70.01	64
ω	-15.50	340.80	341.11	-63.64	99
ω	-25.50	330.51	47.91	-56.95	185
ω	-25.50	239.19	209.98	28.88	204
ω	-18.00	243.20	310.97	36.30	208
ω	27.00	277.79	5.00	57.63	221
Φ	-10.50	318.39	249.35	52.47	254
ω	17.00	322.24	318.36	83.36	114
Φ	27.00	352.41	83.39	85.83	157
Φ	-18.00	124.02	292.98	-95.28	588

Rotation frames were integrated using SAINT,[3] producing a listing of unaveraged F^2 and $\sigma(F^2)$ values which were then passed to the SHELXTL[4] program package for further processing and structure solution. A total of 73021 reflections were measured over the ranges $1.86 \leq \theta \leq 27.54°$, $-14 \leq h \leq 14$, $-16 \leq k \leq 16$, $-23 \leq l \leq 23$ yielding 10200 unique reflections ($R_{int} = 0.0189$). The intensity data were corrected for Lorentz and

[3]Bruker (2009) SAINT. Bruker AXS Inc., Madison, Wisconsin, USA.

[4]Bruker (2009) SHELXTL. Bruker AXS Inc., Madison, Wisconsin, USA.

polarization effects and for absorption using SADABS[5] (minimum and maximum transmission 0.6876, 0.7456).

The structure was solved by direct methods (SHELXS-97[6]). Refinement was by full-matrix least squares based on F^2 using SHELXL-97[1]. All reflections were used during refinement. The weighting scheme used was $w=1/[\sigma^2(F_o^2)+ (0.0907P)^2 + 0.3133P]$ where $P = (F_o^2 + 2F_c^2)/3$. Non-hydrogen atoms were refined anisotropically and hydrogen atoms were refined using a riding model. Refinement converged to R1=0.0266 and wR2=0.0630 for 9570 observed reflections for which $F > 4\sigma(F)$ and R1=0.0292 and wR2=0.0655 and GOF =1.051 for all 10200 unique, non-zero reflections and 643 variables.[7] The maximum λ/σ in the final cycle of least squares was 0.002 and the two most prominent peaks in the final difference Fourier were +1.120 and -0.826 e/Å^3.

Table A1-1 lists cell information, data collection parameters, and refinement data. Final positional and equivalent isotropic thermal parameters are given in Tables A1-2 and A1-3. Anisotropic thermal parameters are in Table A1-4. Tables A1-5 and A1-6 list bond

---

[5]Sheldrick, G.M. (2007) SADABS. University of Gottingen, Germany.

[7]$R1 = \Sigma||F_o| - |F_c|| / \Sigma |F_o|$

$wR2 = [\Sigma w(F_o^2 - F_c^2)^2/\Sigma w(F_o^2)^2]^{½}$

$GOF = [\Sigma w(F_o^2 - F_c^2)^2/(n - p)]^{½}$

where n = the number of reflections and p = the number of parameters refined.

distances and bond angles. Figure A1-1 is an ORTEP[8] representation of the molecule with 50% probability thermal ellipsoids displayed.

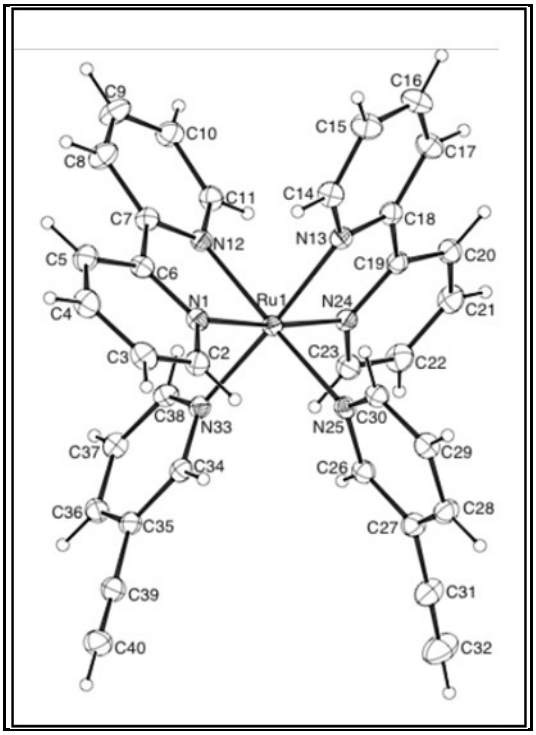

Figure A1-1. ORTEP drawing of RuBEP with 50% probability thermal ellipsoids.

[8]"ORTEP-II: A Fortran Thermal Ellipsoid Plot Program for Crystal Structure Illustrations". C.K. Johnson (1976) ORNL-5138.

Table A1-1. Summary of structure determination of [RuBEP]$(PF_6)_2$

Empirical formula	$C_{83}H_{82}F_{24}N_{12}O_5P_4Ru_2$
Formula weight	2109.63
Temperature	100(1) K
Wavelength	0.71073 Å
Crystal system	Triclinic
Space group	PT
Cell constants:	
a	11.2159(7) Å
b	12.5550(8) Å
c	18.1382(12) Å
α	70.206(3)°
β	85.323(3)°
γ	67.450(2)°
Volume	2216.1(2) $Å^3$
Z	1
Density (calculated)	1.581 Mg/m^3
Absorption coefficient	0.522 mm^{-1}
F(000)	1068
Crystal size	0.42 x 0.26 x 0.10 mm^3
Theta range for data collection	1.86 to 27.54°
Index ranges	$-14 \le h \le 14$, $-16 \le k \le 16$, $-23 \le l \le 23$
Reflections collected	73021
Independent reflections	10200 [R(int) = 0.0189]
Completeness to theta = 27.54°	99.6 %
Absorption correction	Semi-empirical from equivalents
Max. and min. transmission	0.7456 and 0.6876
Refinement method	Full-matrix least-squares on F^2
Data / restraints / parameters	10200 / 122 / 643
Goodness-of-fit on F^2	1.051
Final R indices [I>2sigma(I)]	R1 = 0.0266, wR2 = 0.0630
R indices (all data)	R1 = 0.0292, wR2 = 0.0655
Largest diff. peak and hole	1.120 and -0.826 $e.Å^{-3}$

Table A1-2. Refined positional parameters for [RuBEP]$(PF_6)_2$

Atom	x	y	z	U_{eq}, Å^2
Ru1	0.506258(11)	0.163868(11)	0.264396(7)	0.01291(4)
N1	0.65818(12)	0.13185(12)	0.19098(8)	0.0153(2)
N12	0.45450(12)	0.07306(12)	0.20479(8)	0.0149(2)
N13	0.57466(12)	-0.00632(12)	0.34959(8)	0.0155(2)
N24	0.35555(13)	0.17812(12)	0.33876(8)	0.0154(2)
N25	0.57819(13)	0.24338(12)	0.32652(8)	0.0155(2)
N33	0.41533(12)	0.33223(12)	0.17585(8)	0.0151(2)
C2	0.75831(15)	0.16753(15)	0.18526(10)	0.0188(3)
C3	0.85450(16)	0.14474(16)	0.13324(10)	0.0219(3)
C4	0.84615(17)	0.08520(16)	0.08327(10)	0.0235(3)
C5	0.74281(16)	0.04878(16)	0.08769(10)	0.0218(3)
C6	0.65119(15)	0.07173(14)	0.14269(9)	0.0169(3)
C7	0.54123(15)	0.03182(14)	0.15400(9)	0.0173(3)
C8	0.52811(17)	-0.04635(17)	0.11907(11)	0.0247(4)
C9	0.42495(18)	-0.08374(17)	0.13656(12)	0.0272(4)
C10	0.33660(17)	-0.04140(16)	0.18777(10)	0.0226(3)
C11	0.35404(15)	0.03707(15)	0.22011(9)	0.0180(3)
C14	0.68458(15)	-0.09937(15)	0.34717(10)	0.0195(3)
C15	0.71162(17)	-0.21890(16)	0.39519(11)	0.0247(4)
C16	0.62293(18)	-0.24480(16)	0.44906(11)	0.0261(4)
C17	0.51085(17)	-0.14999(16)	0.45341(10)	0.0222(3)
C18	0.48813(15)	-0.03161(14)	0.40305(9)	0.0165(3)
C19	0.36860(15)	0.07434(14)	0.40007(9)	0.0161(3)

C20	0.27411(16)	0.07009(16)	0.45418(10)	0.0204(3)
C21	0.16281(17)	0.17312(17)	0.44612(10)	0.0235(3)
C22	0.15004(17)	0.27882(16)	0.38419(11)	0.0239(3)
C23	0.24783(16)	0.27815(15)	0.33221(10)	0.0198(3)
C26	0.50882(15)	0.35333(14)	0.33424(9)	0.0173(3)
C27	0.55503(16)	0.40441(15)	0.37742(10)	0.0200(3)
C28	0.67825(17)	0.33911(15)	0.41461(10)	0.0211(3)
C29	0.75013(16)	0.22637(15)	0.40647(10)	0.0198(3)
C30	0.69787(15)	0.18182(14)	0.36276(9)	0.0172(3)
C31	0.47574(18)	0.52329(17)	0.38143(11)	0.0262(4)
C32	0.4114(2)	0.62209(19)	0.38320(13)	0.0366(5)
C34	0.47048(15)	0.41520(14)	0.14776(9)	0.0164(3)
C35	0.41314(15)	0.52533(14)	0.08664(9)	0.0173(3)
C36	0.29400(16)	0.55052(15)	0.05305(9)	0.0191(3)
C37	0.23679(16)	0.46539(15)	0.08154(10)	0.0191(3)
C38	0.29993(15)	0.35806(15)	0.14190(9)	0.0174(3)
C39	0.47884(16)	0.60893(15)	0.05965(10)	0.0201(3)
C40	0.53479(18)	0.67633(17)	0.03667(11)	0.0259(4)
P1	0.91753(4)	0.07849(4)	0.63543(3)	0.01945(9)
F1	0.77189(10)	0.10137(11)	0.61329(8)	0.0342(3)
F2	1.06165(11)	0.05864(13)	0.65717(9)	0.0424(3)
F3	0.92791(14)	-0.04413(12)	0.70349(9)	0.0504(4)
F4	0.97134(12)	0.00549(13)	0.57550(8)	0.0439(3)
F5	0.90455(13)	0.20274(12)	0.56596(8)	0.0429(3)
F6	0.86228(11)	0.15488(12)	0.69372(7)	0.0368(3)

P2	0.86742(4)	0.76441(4)	-0.00468(3)	0.02104(9)
F7	0.83036(18)	0.78269(12)	0.07795(8)	0.0564(4)
F8	0.89749(19)	0.75132(17)	-0.08864(9)	0.0644(5)
F9	0.71659(13)	0.81513(15)	-0.02793(10)	0.0695(6)
F10	0.86397(11)	0.90155(10)	-0.04003(7)	0.0306(2)
F11	1.01548(12)	0.71759(12)	0.01791(11)	0.0554(4)
F12	0.86992(12)	0.62856(11)	0.03176(8)	0.0373(3)
C41	0.8714(2)	0.33261(18)	0.77964(12)	0.0307(4)
C42	1.0085(2)	0.2875(3)	0.75661(19)	0.0539(7)
C43	0.8319(3)	0.2412(2)	0.84166(13)	0.0412(5)
O1	0.79828(19)	0.43755(14)	0.75071(11)	0.0501(4)
C44	0.7925(4)	0.4704(4)	0.2172(3)	0.0285(8)
C45	0.9341(4)	0.4331(4)	0.2064(3)	0.0467(10)
C46	0.7225(6)	0.5914(5)	0.2295(4)	0.0436(12)
O2	0.7350(3)	0.4074(3)	0.21545(17)	0.0437(6)
C47	0.7960(5)	0.5225(4)	0.2705(3)	0.0266(9)
C48	0.6794(7)	0.6370(7)	0.2342(5)	0.0403(16)
C49	0.8510(10)	0.4355(8)	0.2255(5)	0.052(2)
O3	0.8449(3)	0.5035(3)	0.33352(18)	0.0263(7)
C50	0.9372(4)	0.4879(4)	0.4842(3)	0.0275(9)
C51	0.8817(5)	0.4529(4)	0.5634(3)	0.0425(11)
C52	1.0506(5)	0.5301(5)	0.4789(3)	0.0392(11)
O4	0.8932(3)	0.4866(3)	0.42707(17)	0.0347(6)

$U_{eq}={}^{1}/_{3}[U_{11}(aa^*)^2+U_{22}(bb^*)^2+U_{33}(cc^*)^2+2U_{12}aa^*bb^*\cos\gamma+2U_{13}aa^*cc^*\cos\beta+2U_{23}bb^*cc^*\cos\alpha]$

Table A1-3. Positional parameters for hydrogens in [RuBEP]$(PF_6)_2$

Atom	x	y	z	U_{iso}, Å^2
H2	0.7632	0.2095	0.2178	0.025
H3	0.9235	0.1690	0.1319	0.029
H4	0.9089	0.0698	0.0473	0.031
H5	0.7349	0.0095	0.0542	0.029
H8	0.5881	-0.0732	0.0843	0.033
H9	0.4153	-0.1367	0.1141	0.036
H10	0.2665	-0.0653	0.2003	0.030
H11	0.2936	0.0662	0.2540	0.024
H14	0.7450	-0.0826	0.3117	0.026
H15	0.7882	-0.2811	0.3914	0.033
H16	0.6387	-0.3246	0.4816	0.035
H17	0.4508	-0.1651	0.4898	0.030
H20	0.2856	-0.0018	0.4957	0.027
H21	0.0982	0.1713	0.4815	0.031
H22	0.0766	0.3496	0.3775	0.032
H23	0.2386	0.3499	0.2911	0.026
H26	0.4265	0.3972	0.3097	0.023
H28	0.7113	0.3704	0.4441	0.028
H29	0.8329	0.1810	0.4302	0.026
H30	0.7473	0.1059	0.3580	0.023
H32	0.3608	0.6998	0.3846	0.049
H34	0.5502	0.3985	0.1700	0.022
H36	0.2535	0.6231	0.0122	0.025

H37	0.1569	0.4803	0.0603	0.025
H38	0.2613	0.3009	0.1600	0.023
H40	0.5786	0.7291	0.0187	0.034
H42a	1.0273	0.3552	0.7214	0.081
H42b	1.0201	0.2290	0.7310	0.081
H42c	1.0658	0.2495	0.8027	0.081
H43a	0.8614	0.2331	0.8922	0.062
H43b	0.8695	0.1636	0.8335	0.062
H43c	0.7394	0.2679	0.8392	0.062
H45a	0.9675	0.3548	0.1992	0.070
H45b	0.9768	0.4278	0.2521	0.070
H45c	0.9493	0.4926	0.1612	0.070
H46a	0.6326	0.6048	0.2359	0.065
H46b	0.7310	0.6558	0.1848	0.065
H46c	0.7591	0.5910	0.2757	0.065
H48a	0.6533	0.6840	0.2689	0.060
H48b	0.6099	0.6152	0.2253	0.060
H48c	0.7006	0.6847	0.1851	0.060
H49a	0.9247	0.3670	0.2547	0.077
H49b	0.8769	0.4766	0.1757	0.077
H49c	0.7866	0.4072	0.2171	0.077
H51a	0.8093	0.4324	0.5583	0.064
H51b	0.8537	0.5205	0.5827	0.064
H51c	0.9467	0.3836	0.5994	0.064
H52a	1.0786	0.5469	0.4262	0.059

H52b	1.1208	0.4668	0.5143	0.059
H52c	1.0229	0.6029	0.4928	0.059

Table A1-4. Refined thermal parameters (U's) for [RuBEP]$(PF_6)_2$

Atom	U_{11}	U_{22}	U_{33}	U_{23}	U_{13}	U_{12}
Ru1	0.01149(6)	0.01408(6)	0.01414(6)	-0.00525(4)	0.00267(4)	-0.00578(5)
N1	0.0133(6)	0.0157(6)	0.0157(6)	-0.0045(5)	0.0025(5)	-0.0053(5)
N12	0.0145(6)	0.0150(6)	0.0148(6)	-0.0042(5)	0.0016(5)	-0.0061(5)
N13	0.0141(6)	0.0169(6)	0.0169(6)	-0.0066(5)	0.0008(5)	-0.0066(5)
N24	0.0153(6)	0.0181(6)	0.0154(6)	-0.0072(5)	0.0027(5)	-0.0081(5)
N25	0.0160(6)	0.0164(6)	0.0146(6)	-0.0047(5)	0.0033(5)	-0.0075(5)
N33	0.0147(6)	0.0161(6)	0.0154(6)	-0.0066(5)	0.0031(5)	-0.0061(5)
C2	0.0170(7)	0.0220(8)	0.0192(7)	-0.0070(6)	0.0028(6)	-0.0095(6)
C3	0.0163(7)	0.0256(8)	0.0230(8)	-0.0052(7)	0.0047(6)	-0.0104(6)
C4	0.0195(8)	0.0262(8)	0.0232(8)	-0.0088(7)	0.0089(6)	-0.0080(7)
C5	0.0221(8)	0.0231(8)	0.0214(8)	-0.0104(7)	0.0061(6)	-0.0081(7)
C6	0.0153(7)	0.0157(7)	0.0182(7)	-0.0049(6)	0.0018(6)	-0.0052(6)
C7	0.0157(7)	0.0174(7)	0.0182(7)	-0.0063(6)	0.0017(6)	-0.0056(6)
C8	0.0229(8)	0.0274(9)	0.0298(9)	-0.0173(7)	0.0072(7)	-0.0103(7)
C9	0.0282(9)	0.0294(9)	0.0348(10)	-0.0196(8)	0.0052(7)	-0.0154(8)
C10	0.0225(8)	0.0247(8)	0.0258(8)	-0.0093(7)	0.0029(7)	-0.0140(7)
C11	0.0166(7)	0.0201(7)	0.0180(7)	-0.0060(6)	0.0025(6)	-0.0083(6)
C14	0.0156(7)	0.0212(8)	0.0218(8)	-0.0071(6)	0.0015(6)	-0.0071(6)
C15	0.0196(8)	0.0190(8)	0.0309(9)	-0.0071(7)	0.0000(7)	-0.0032(6)
C16	0.0274(9)	0.0174(8)	0.0291(9)	-0.0017(7)	-0.0009(7)	-0.0085(7)
C17	0.0221(8)	0.0221(8)	0.0225(8)	-0.0044(7)	0.0028(6)	-0.0113(7)
C18	0.0160(7)	0.0194(7)	0.0167(7)	-0.0068(6)	0.0013(6)	-0.0086(6)
C19	0.0172(7)	0.0184(7)	0.0159(7)	-0.0074(6)	0.0019(6)	-0.0090(6)

C20	0.0238(8)	0.0232(8)	0.0183(8)	-0.0077(6)	0.0056(6)	-0.0133(7)
C21	0.0216(8)	0.0295(9)	0.0246(8)	-0.0140(7)	0.0104(7)	-0.0126(7)
C22	0.0197(8)	0.0251(8)	0.0266(9)	-0.0131(7)	0.0069(7)	-0.0056(7)
C23	0.0189(8)	0.0198(8)	0.0201(8)	-0.0076(6)	0.0034(6)	-0.0064(6)
C26	0.0164(7)	0.0174(7)	0.0169(7)	-0.0052(6)	0.0029(6)	-0.0061(6)
C27	0.0222(8)	0.0189(8)	0.0203(8)	-0.0082(6)	0.0042(6)	-0.0083(6)
C28	0.0236(8)	0.0224(8)	0.0218(8)	-0.0097(6)	0.0009(6)	-0.0112(7)
C29	0.0173(7)	0.0211(8)	0.0202(8)	-0.0051(6)	-0.0007(6)	-0.0076(6)
C30	0.0162(7)	0.0167(7)	0.0178(7)	-0.0052(6)	0.0025(6)	-0.0062(6)
C31	0.0268(9)	0.0264(9)	0.0281(9)	-0.0135(7)	0.0001(7)	-0.0087(7)
C32	0.0350(11)	0.0292(10)	0.0446(12)	-0.0212(9)	-0.0036(9)	-0.0021(8)
C34	0.0151(7)	0.0194(7)	0.0174(7)	-0.0088(6)	0.0038(6)	-0.0075(6)
C35	0.0196(7)	0.0177(7)	0.0166(7)	-0.0082(6)	0.0067(6)	-0.0080(6)
C36	0.0200(8)	0.0171(7)	0.0172(7)	-0.0053(6)	0.0021(6)	-0.0042(6)
C37	0.0161(7)	0.0211(8)	0.0207(8)	-0.0088(6)	0.0009(6)	-0.0060(6)
C38	0.0153(7)	0.0188(7)	0.0210(8)	-0.0089(6)	0.0033(6)	-0.0082(6)
C39	0.0209(8)	0.0196(8)	0.0193(8)	-0.0077(6)	0.0049(6)	-0.0068(6)
C40	0.0298(9)	0.0251(9)	0.0268(9)	-0.0100(7)	0.0096(7)	-0.0149(7)
P1	0.01575(19)	0.0244(2)	0.0210(2)	-0.01088(17)	0.00422(15)	-0.00833(16)
F1	0.0199(5)	0.0419(7)	0.0526(7)	-0.0303(6)	0.0009(5)	-0.0113(5)
F2	0.0166(5)	0.0530(8)	0.0643(9)	-0.0304(7)	-0.0008(5)	-0.0103(5)
F3	0.0471(8)	0.0362(7)	0.0502(8)	0.0053(6)	0.0052(6)	-0.0149(6)
F4	0.0363(7)	0.0536(8)	0.0534(8)	-0.0411(7)	0.0134(6)	-0.0111(6)
F5	0.0426(7)	0.0355(7)	0.0405(7)	-0.0020(5)	0.0113(6)	-0.0151(6)
F6	0.0305(6)	0.0582(8)	0.0378(6)	-0.0358(6)	0.0084(5)	-0.0177(6)

P2	0.01733(19)	0.0287(2)	0.0218(2)	-0.01123(17)	0.00414(16)	-0.01182(17)
F7	0.1081(13)	0.0372(7)	0.0286(7)	-0.0170(6)	0.0303(7)	-0.0324(8)
F8	0.1137(14)	0.0909(12)	0.0411(8)	-0.0449(8)	0.0397(9)	-0.0807(12)
F9	0.0283(7)	0.0710(10)	0.0773(11)	0.0349(9)	-0.0177(7)	-0.0329(7)
F10	0.0297(6)	0.0302(6)	0.0310(6)	-0.0061(5)	0.0064(5)	-0.0148(5)
F11	0.0200(6)	0.0354(7)	0.0984(12)	-0.0064(7)	-0.0155(7)	-0.0078(5)
F12	0.0438(7)	0.0322(6)	0.0451(7)	-0.0163(5)	0.0065(6)	-0.0221(5)
C41	0.0405(11)	0.0273(9)	0.0309(10)	-0.0136(8)	-0.0054(8)	-0.0148(8)
C42	0.0437(13)	0.0595(16)	0.0807(19)	-0.0376(15)	0.0061(13)	-0.0310(12)
C43	0.0648(15)	0.0345(11)	0.0319(11)	-0.0191(9)	0.0104(10)	-0.0216(11)
O1	0.0649(12)	0.0273(8)	0.0487(10)	-0.0093(7)	-0.0069(8)	-0.0086(8)
C44	0.030(2)	0.035(2)	0.0234(18)	-0.0038(16)	0.0006(17)	-0.0205(18)
C45	0.033(2)	0.056(3)	0.047(2)	-0.0104(19)	-0.0049(18)	-0.0172(19)
C46	0.052(3)	0.039(3)	0.051(3)	-0.018(3)	0.016(3)	-0.029(3)
O2	0.0426(15)	0.0430(15)	0.0558(17)	-0.0174(13)	0.0019(12)	-0.0259(12)
C47	0.030(2)	0.024(2)	0.025(2)	0.0034(18)	0.0004(19)	-0.019(2)
C48	0.038(4)	0.042(4)	0.030(3)	0.003(3)	-0.011(3)	-0.013(3)
C49	0.062(6)	0.052(5)	0.042(4)	-0.021(4)	-0.008(5)	-0.018(4)
O3	0.0254(16)	0.0274(16)	0.0234(15)	-0.0020(13)	-0.0050(12)	-0.0114(13)
C50	0.0300(16)	0.0191(14)	0.0274(16)	-0.0095(14)	0.0036(14)	-0.0020(11)
C51	0.065(3)	0.041(2)	0.028(2)	-0.0137(18)	0.014(2)	-0.028(2)
C52	0.046(3)	0.032(2)	0.040(3)	-0.010(2)	-0.010(3)	-0.013(2)
O4	0.0321(15)	0.0307(14)	0.0386(16)	-0.0121(12)	0.0000(12)	-0.0082(12)

The form of the anisotropic displacement parameter is:

$\exp[-2\pi^2(a^{*2}U_{11}h^2+b^{*2}U_{22}k^2+c^{*2}U_{33}l^2+2b^*c^*U_{23}kl+2a^*c^*U_{13}hl+2a^*b^*U_{12}hk)]$

Table A1-5. Bond distances in [RuBEP]$(PF_6)_2$, Å

Ru1-N13	2.0595(13)	Ru1-N12	2.0617(13)	Ru1-N24	2.0660(13)
Ru1-N1	2.0750(13)	Ru1-N33	2.0981(13)	Ru1-N25	2.1083(13)
N1-C2	1.345(2)	N1-C6	1.359(2)	N12-C11	1.344(2)
N12-C7	1.362(2)	N13-C14	1.345(2)	N13-C18	1.363(2)
N24-C23	1.345(2)	N24-C19	1.362(2)	N25-C26	1.349(2)
N25-C30	1.355(2)	N33-C34	1.346(2)	N33-C38	1.354(2)
C2-C3	1.384(2)	C3-C4	1.384(3)	C4-C5	1.388(2)
C5-C6	1.391(2)	C6-C7	1.476(2)	C7-C8	1.390(2)
C8-C9	1.384(2)	C9-C10	1.381(3)	C10-C11	1.382(2)
C14-C15	1.383(2)	C15-C16	1.387(3)	C16-C17	1.380(2)
C17-C18	1.392(2)	C18-C19	1.471(2)	C19-C20	1.388(2)
C20-C21	1.384(2)	C21-C22	1.384(3)	C22-C23	1.386(2)
C26-C27	1.398(2)	C27-C28	1.395(2)	C27-C31	1.438(2)
C28-C29	1.386(2)	C29-C30	1.383(2)	C31-C32	1.182(3)
C34-C35	1.397(2)	C35-C36	1.391(2)	C35-C39	1.439(2)
C36-C37	1.385(2)	C37-C38	1.383(2)	C39-C40	1.187(3)
P1-F3	1.5831(13)	P1-F4	1.5904(12)	P1-F6	1.5956(11)
P1-F2	1.5998(12)	P1-F5	1.6021(13)	P1-F1	1.6064(11)
P2-F11	1.5717(13)	P2-F8	1.5821(14)	P2-F7	1.5907(13)
P2-F12	1.5967(12)	P2-F9	1.5980(13)	P2-F10	1.6070(12)
C41-O1	1.207(3)	C41-C43	1.488(3)	C41-C42	1.498(3)
C44-O2	1.205(4)	C44-C45	1.490(5)	C44-C46	1.504(6)
C47-O3	1.217(5)	C47-C49	1.499(7)	C47-C48	1.506(6)
C50-O4	1.192(5)	C50-C51	1.509(5)	C50-C52	1.538(6)

Table A1-6. Bond angles in [RuBEP]$(PF_6)_2$, °

N13-Ru1-N12	83.17(5)	N13-Ru1-N24	78.73(5)	N12-Ru1-N24	96.51(5)
N13-Ru1-N1	97.01(5)	N12-Ru1-N1	78.84(5)	N24-Ru1-N1	174.11(5)
N13-Ru1-N33	172.47(5)	N12-Ru1-N33	91.25(5)	N24-Ru1-N33	96.99(5)
N1-Ru1-N33	86.80(5)	N13-Ru1-N25	93.45(5)	N12-Ru1-N25	174.24(5)
N24-Ru1-N25	87.36(5)	N1-Ru1-N25	97.01(5)	N33-Ru1-N25	92.52(5)
C2-N1-C6	118.06(13)	C2-N1-Ru1	126.69(11)	C6-N1-Ru1	115.21(10)
C11-N12-C7	118.18(14)	C11-N12-Ru1	125.44(11)	C7-N12-Ru1	115.65(10)
C14-N13-C18	118.04(14)	C14-N13-Ru1	125.13(11)	C18-N13-Ru1	115.42(10)
C23-N24-C19	117.88(13)	C23-N24-Ru1	126.67(11)	C19-N24-Ru1	115.45(10)
C26-N25-C30	117.15(14)	C26-N25-Ru1	123.00(11)	C30-N25-Ru1	119.83(10)
C34-N33-C38	117.45(14)	C34-N33-Ru1	122.42(11)	C38-N33-Ru1	120.04(10)
N1-C2-C3	123.04(15)	C2-C3-C4	118.81(15)	C3-C4-C5	119.01(15)
C4-C5-C6	119.28(16)	N1-C6-C5	121.77(15)	N1-C6-C7	115.09(14)
C5-C6-C7	123.14(15)	N12-C7-C8	121.53(15)	N12-C7-C6	114.77(14)
C8-C7-C6	123.64(15)	C9-C8-C7	119.35(16)	C10-C9-C8	119.12(16)
C9-C10-C11	118.91(16)	N12-C11-C10	122.89(15)	N13-C14-C15	122.82(15)
C14-C15-C16	119.12(16)	C17-C16-C15	118.79(16)	C16-C17-C18	119.60(16)
N13-C18-C17	121.61(15)	N13-C18-C19	114.62(14)	C17-C18-C19	123.71(14)
N24-C19-C20	121.75(15)	N24-C19-C18	114.87(13)	C20-C19-C18	123.38(15)
C21-C20-C19	119.82(16)	C22-C21-C20	118.42(15)	C21-C22-C23	119.33(16)
N24-C23-C22	122.79(16)	N25-C26-C27	123.01(15)	C28-C27-C26	118.87(15)
C28-C27-C31	121.66(16)	C26-C27-C31	119.46(15)	C29-C28-C27	118.30(15)
C30-C29-C28	119.51(15)	N25-C30-C29	123.16(15)	C32-C31-C27	178.6(2)
N33-C34-C35	122.86(15)	C36-C35-C34	118.75(15)	C36-C35-C39	121.81(15)

C34-C35-C39	119.44(15)	C37-C36-C35	118.71(15)	C38-C37-C36	119.18(15)
N33-C38-C37	123.05(15)	C40-C39-C35	178.65(18)	F3-P1-F4	90.54(8)
F3-P1-F6	90.85(8)	F4-P1-F6	178.55(8)	F3-P1-F2	91.13(8)
F4-P1-F2	90.12(7)	F6-P1-F2	90.26(7)	F3-P1-F5	178.94(8)
F4-P1-F5	89.28(8)	F6-P1-F5	89.32(7)	F2-P1-F5	89.91(8)
F3-P1-F1	89.77(8)	F4-P1-F1	90.64(7)	F6-P1-F1	88.97(6)
F2-P1-F1	178.82(7)	F5-P1-F1	89.19(7)	F11-P2-F8	91.44(10)
F11-P2-F7	91.11(10)	F8-P2-F7	177.15(11)	F11-P2-F12	91.15(7)
F8-P2-F12	91.85(8)	F7-P2-F12	89.35(7)	F11-P2-F9	178.68(9)
F8-P2-F9	88.88(11)	F7-P2-F9	88.54(10)	F12-P2-F9	90.12(8)
F11-P2-F10	88.99(7)	F8-P2-F10	89.09(7)	F7-P2-F10	89.69(7)
F12-P2-F10	179.04(7)	F9-P2-F10	89.74(7)	O1-C41-C43	122.0(2)
O1-C41-C42	121.9(2)	C43-C41-C42	116.0(2)	O2-C44-C45	121.9(4)
O2-C44-C46	120.7(4)	C45-C44-C46	117.4(4)	O3-C47-C49	121.7(5)
O3-C47-C48	120.6(5)	C49-C47-C48	117.7(5)	O4-C50-C51	121.7(4)
O4-C50-C52	120.6(5)	C51-C50-C52	117.7(5)		

Appendix B. Table of Abbreviations

Abbreviation	Definition
$[Ru(bpy)_2XY]^{n+}$	Ru(II) center with two bipyridines and two monodentate ligands
1-P	1-photon
2′-F RNA	2′-Fluoro RNA
2′-OMe RNA	2′-O-methyl RNA
2-P	2-photon
3-EP	3-ethynylpyridine ligand
4-AP	4-aminopyridine
6-FAM	carboxyfluorescein
BHQ1	black hole quencher
bpy	2, 2′-bipyridine
CHANT1	caged hairpin antagomir with 1 photocleavable moiety, targeting *let-7*
CHANT2	caged hairpin antagomir with 2 photocleavable moieties, targeting *let-7*
chd	zebrafish *chordin* gene
chd-MO	control morpholino targeting *chordin*
CIRC*let7*	circular *let-7* miRNA
CLSM	confocal laser scanning microscopy
DLS	dynamic light scattering
DMNPE	(dimethoxy-2-nitrophenyl)ethyl moiety

DMT	dimethoxytrityl
FITC	fluorescein isothiocyanate
fl-MO	fluorescein labeled morpholino
GM	Göppert-Mayer
hpf	hours post fertilization
ISC	intersystem crossing
let-7	zebrafish miRNA, *lethal-7*
LF	ligand field
LNA	locked nucleic acid
MB	molecular beacon
miRNA	micro RNA
MLCT	metal to ligand charge transfer
MO	morpholino
N_3-DNA	DNA with single azide modification
N_3-DNA-N_3	DNA with two azide modifications
ntl	zebrafish *notail* gene
ntl-MO	control morpholino targeting *notail*
OB29	polyethyleneoxide$_{30}$ - polybutadiene$_{46}$
ONB	*o*-nitrobenzyl photocleavable moiety
PAGE	polyacrylamide gel electrophoresis

PL	nitrobenzyl photocleavable linker moiety
PZn_2	meso to meso ethyne bridged [bis(porphinato)zinc]
RISC	RNA-induced silencing complex
RNAi	RNA interference
RuBEP	$Ru(bpy)_2(3\text{-ethynylpyridine})_2Cl_2$
Ru-cDNA	DNA circularized with RuBEP
Ru-DNA	DNA singly clicked to RuBEP
Ru-cMO	Morpholino circularized with RuBEP
siRNA	short interfering RNA
Sulfo-EMCS	N-Ɛ-Maleimidocaproyl-oxysulfosuccinimide ester
TBTA	([(1-benzyl-1*H*-1,2,3-triazol-4-yl)methyl]amine)
TEAA	triethylammonium acetate
TLF wildtype	Tuebingen long fin wildtype zebrafish
Tu wildtype	Tuebingen wildtype zebrafish
WT	wildtype